Titre: Title:	Syngas/Photo-Initiated Chemical Vapor Deposition to Modify Single-Walled Carbon Nanotubes
Auteur: Author:	Seyedehsan Hosseininasab
Date:	2018
Type:	Mémoire ou thèse / Dissertation or Thesis
Référence: Citation:	Hosseininasab, S. (2018). Syngas/Photo-Initiated Chemical Vapor Deposition to Modify Single-Walled Carbon Nanotubes [Thèse de doctorat, École Polytechnique de Montréal]. PolyPublie. https://publications.polymtl.ca/3938/

URL de PolyPublie: PolyPublie URL:	https://publications.polymtl.ca/3938/
Directeurs de recherche: Advisors:	Nathalie Faucheux, Gervais Soucy, & Jason Robert Tavares
Programme: Program:	Génie chimique

POLYTECHNIQUE MONTRÉAL

affiliée à l'Université de Montréal

Syngas/photo-initiated chemical vapor deposition to modify single-walled carbon nanotubes

SEYEDEHSAN HOSSEININASAB

Département de génie chimique

Thèse présentée en vue de l'obtention du diplôme de *Philosophiæ Doctor*

Génie chimique

Octobre 2018

POLYTECHNIQUE MONTRÉAL

affiliée à l'Université de Montréal

Cette thèse intitulée:

Syngas/photo-initiated chemical vapor deposition to modify single-walled carbon nanotubes

présentée par : **Seyedehsan HOSSEININASAB**

en vue de l'obtention du diplôme de *Philosophiæ Doctor*

a été dûment acceptée par le jury d'examen constitué de :

Paul STUART, président
Jason Robert TAVARES, membre et directeur de recherche
Nathalie FAUCHEUX, membre et codirectrice de recherche
Gervais SOUCY, membre et codirecteur de recherche
Louis FRADETTE, membre
Pierre-Luc GIRARD-LAURIAULT, membre

DEDICATION

To my beloved parents and family

To my lovely wife for her love, endless support, and encouragement.

ACKNOWLEDGEMENTS

RÉSUMÉ

Dans la présente étude, nous détaillons le développement d'une méthode performante pour la fonctionnalisation de nanotubes de carbone mono-paroi (SWCNTs) à l'aide de dépôt chimique en phase vapeur photo-initié (PICVD) à base de syngaz (CO+H_2) qui se montre efficace pour l'introduction d'une grande variété de groupes fonctionnels en surface. Les résultats mettent en évidence qu'en modifiant les paramètres expérimentaux de pression, de ratio molaire H_2/CO, de temps de traitement et de la position du substrat dans le réacteur, la mouillabilité du matériaux peut être finement ajustée en passant d'hydrodophile à super-hydrophobe (que ce soit par modification de la densité des groupes fonctionnels ou encore par modification directe de la topologie de surface). De plus, une étude cinétique du procédé mis en oeuvre a été effectuée en phase gazeuse et en surface afin de comprendre l'effet et le comportement du traitement des SWCNTs, incluant le rôle de la température. Il a été déterminé que le pentacarbonyle de fer (l'impurité la plus abondante dans les cylindres de monoxyde de carbone) joue un rôle crucial dans le procédé puisqu'il est consommé à plus de 94% durant le traitement, contre 0% du CO et du H_2 injectés dans le réacteur. Le bilan de matière du syngas/PICVD a été calculé en se basant sur la caractérisation de la phase gazeuse et de la surface des SWCNT. La composition chimique du matériel déposé a été identifiée comme étant du $C_{38}H_5O_{43}Fe_{14}$, avec une principale présence de groupes carboxyliques, hydroxyles, de $Fe(CO)_n$ et de $Fe(OH)_n$. Sur la base des analyses et du bilan de masse ontenus, nous suggérons deux mécanismes distincts pour la chimie se déroulant en phase gazeuse (incluant 12 réactions) et en phase de surface (incluant 30 réactions).

Pour conclure, la procédé de syngas/PICVD présenté ici se montre une technique prometteuse pour réaliser la fonctionnalisation de nanomatériaux tel que les SWCNTs, et ce, avec une grande plage de valeurs de mouillabilité. Cette dernière composante peut être modulée librement en modifiant les paramètres expérimentaux comme la pression, le ratio molaire H_2/CO, la position du substrat dans le réacteur et le débit d'injection des précurseurs.

ABSTRACT

In the present study, a promising method has been developed to functionalize single-wall carbon nanotubes (SWCNTs) using photo-initiated chemical vapor deposition (PICVD) with syngas ($CO+H_2$) and then applying it to form a full range of functional groups on the surface of the SWCNTs. It was observed that by changing the operating conditions, including pressure, the molar ratio of H_2/CO, treatment time, and the position of the substrate inside the reactor, a wide range of wettability (caused either by functionality density or physical roughness of the coating) ranging from super-hydrophilic to super-hydrophobic can be obtained. A kinetic study of the syngas/PICVD process was then performed in both the gas and surface phases to understand the syngas/PICVD behavior in the treatment of SWCNTs. The influence of temperature on this process was also determined to gain more insight about the syngas/PICVD behavior on SWCNT treatment. We found that iron pentacarbonyl, the most common impurity in the carbon monoxide cylinder, played a very important role in this process considering that 94% is consumed during treatment, while at the same time carbon monoxide and hydrogen fed to the reactor was not consumed. The mass balance of syngas/PICVD was calculated based on the gas phase characterizations and surface phase analyses of SWCNTs. The chemical structure of the deposited coating was identified as $C_{38}H_5O_{43}Fe_{14}$ in the majority with mainly carboxylic, hydroxyl, $Fe(CO)_n$, and $Fe(OH)_n$ chemical moieties. Based on the analyses and the obtained mass balance, two mechanisms were suggested for the gas phase (including 12 reactions) and surface phase (including 30 reactions) reactions, separately.

As a general conclusion, it was demonstrated that syngas/PICVD was a promising method for functionalizing nanoparticles, especially SWCNTs in a full range of wettability. It was also possible to control wettability by changing the operational parameters, including pressure, the molar ratio of H_2/CO, the position of the substrate inside the reactor, and the flow rate of precursors.

TABLE OF CONTENTS

LIST OF TABLES

LIST OF FIGURES

LIST OF SYMBOLS AND ABBREVIATIONS

AFM	Atomic Force Microscopy
αMEM	Alpha Minimum Essential Medium
ALP	Alkaline Phosphatase
Al	Aluminum
PBS	Phosphate Buffered Saline
BMP	Bone Morphogenetic Protein
BSP	Bone Sialoprotein
BGs	Bioactive Glasses
CNT	Carbon Nanotube
CA	Contact Angle
CHI	Chitosan
CVD	Chemical Vapour Deposition
CO	Carbon Monoxide
DWCNT	Double-Wall Carbon Nanotube
DOE	Design of Experiment
DTGA	Differential Thermogravimetric Analysis
ECM	Extracellular Matrix
EDS	Energy Dispersive Spectroscopy
FTIR	Fourier Transform Infrared Spectroscopy
Fe	Iron
GF	Growth Factor
GC	Gas Chromatography

HR	High-Resolution
HR-XPS	High-Resolution X-ray Photoelectron Spectroscopy
HAP	Hydroxyapatite
hMSCs	Human Mesenchymal Stem Cells
HUVECs	Human Umbilical Vein Endothelial Cells
HREELS	High-Resolution Electron Energy Loss Spectroscopy
HWCVD	Hot-Wire Chemical Vapor Deposition
HSCs	Hematopoietic Stem Cells
H_2O_2	Hydrogen Peroxide
H_2	Hydrogen
HEK293	Human Embryo Kidney 293
ICP-MS	Inductively Coupled Plasma Mass Spectroscopy
IR	Infrared
IC50	Half Maximal Inhibitory Concentration
Kr	Krypton
LDH	Lactate Dehydrogenase
LOD	Limit of Detection
MSCs	Mesenchymal Stem Cells
MMP	Mitochondrial Membrane Potential
MTT	(3-(4,5-dimethylthiazolyl-2)-2,5-diphenyltetrazolium bromide)
MWCNT	Multi-Wall Carbon Nanotube
MS	Mass Spectroscopy
MAM	Murine Alveolar Macrophages
Mg	Magnesium

NCP   Nanocrystalline Diamond

NIR   Near-Infrared Spectroscopy

NR   Neutral Red

NH_3 Ammonia

Ni   Nickel

Ozone/UV   Treatment by Ozone under UV light

O-T-SWCNT Ozone Treated Single-Wall Carbon Nanotubes

P-SWCNT   Pure Single-Wall Carbon Nanotubes

PVP   Polyvinyl Pyrrolidone

PEI   Polyethyleneimine

PG   Poly Glycerol

PCA   Polycitric Acid

PLA   Polylactic Acid

PGA   Polyglycolide

PP   Polypropylene

PE   Polyethylene

PI   Photo-Initiator

PICVD   Photo-Initiated Chemical Vapour Deposition

PECVD   Plasma Enhanced Chemical Vapor Deposition

PES   Photoelectron Spectroscopy

PEG   Polyethylene Glycol

PhotoSEL   Photochemical Surface Engineering Laboratory

PPM   Part per Million

PVP   Polyvinylpyrrolidone

PCL	Poly(Epsilon-)Caprolactone
ROS	Reactive Oxygen Species
RF	Radio Frequency
R-SWCNT	Raw- Single Wall Carbon Nanotube
RT	Room temperature
rhBMP-2	Recombinant human bone morphogenetic protein-2
SWCNT	Single Wall Carbon Nanotube
SEM	Scanning Electron Microscopy
Saos-2	Osteosarcoma Cells
SS	Stainless Steel
SDS	Sodium Dodecyl Sulfate
Syngas/PICVD	Syngas Photo-Initiated Chemical Vapour Deposition
S-T-SWCNT	Syngas Treated Single-Wall Carbon Nanotube
SCCM	Standard Cubic Centimeters per Minute
T-SWCNT	Treated Single-Wall Carbon Nanotube
TEG	Triethylene Glycol
TEM	Transmission Electron Microscopy
TACVD	Thermal Activated Chemical Vapor Deposition
TFBA	4-Trifluoromethyl Benzaldehyde
TFAA	Trifluoroacetic Anhydride
TGA	Thermogravimetry Analysis
TdT	Deoxynucleotidyl Transferase
Ti	Titanium
UV	Ultra-Violet

VACNT	Vertically Aligned Carbon Nanotube
XPS	X-Ray Photoelectron Spectroscopy
Xe	Xenon
3-D	3-Dimensional
P	Density
γ_{sl}	Solid-Liquid Interfacial Energy
γ_l^p	Polar Component of Liquid Surface Tension
γ_l^d	Dispersive Component of Liquid Surface Tension
γ_s	Total Free Surface Tension of Solid
γ_s^d	Dispersive Components of Solid Surface Tension
γ_s^p	Polar Components of Solid Surface Tension
θ	Liquid Contact Angle

LIST OF APPENDICES

CHAPTER 1   INTRODUCTION

Carbon nanotubes (CNTs) are allotropes of carbon explored by Ijiima (1991), which form cylinders with a nanometer-scale diameter and micrometer-scale length [1]. CNTs can be produced either as single wall carbon nanotubes (SWCNTs) or multi-walled carbon nanotubes (MWCNTs), which have one or more than one shell, respectively [1]. SWCNTs are synthesized by various methods, such as chemical vapor deposition (CVD), arc discharge, laser ablation, microwave inductive heating, chemical methods, and cold plasma [2]. The final purity of CNT production is different from one method to another. The laser ablation synthesis method produces the highest quality CNTs (>75%) but is quite expensive for the industry. CVD yields SWCNTs with a lower purity (about 30-50% by weight) final product [1, 3] and a high defect density, its main disadvantages. The lower purity of SWCNTs when comparing laser ablation and arc discharge is due to a lower synthesis temperature. The remaining weight percentage (up to 100%) is impurities, including metallic nanoparticles (used as a catalyst) and carbonaceous impurities, such as amorphous carbon, graphitic carbon, and carbon nanoparticles (carbon molecules that can not be turned into CNTs and are formed during the synthesis processes). Although these metallic nanoparticles, such as Ni, Co, Fe, and Y, seem to be necessary for the SWCNT synthesis, their post removal from the synthesized SWCNTs in order to purify them is a major challenge. CVD can be scaled-up to commercial scale as it is reported that this method can produce 100 g/h of SWCNTs (the main advantage of this method) [2]. Recently, radio frequency (RF) induction thermal plasma has been introduced as a promising method to synthesize SWCNTs with higher purity than CVD and presents several advantages, such as high yield, high production rate, and no vacuum filtering [2]. CNTs have attracted the attention of many researchers because of their unique and individual properties, such as high electrical conductivity (CNTs are able to be both metallic and a semiconductor simply by structural changes rather than compositional changes), high Young's modulus (between 1 and 5 TPa), high mechanical strength, and light weight [1]. All these individual properties make them a promising candidate for different applications, such as electronics, high-strength materials, and biomedical applications or tissue engineering [1].

These materials have become one of the most important areas of research and technology in Canada considering their above-mentioned unique properties and the potential for commercial applications in the last five years [4]. The potential applications of these materials in Canada

include electronics, sensors, bioactive materials, structural materials, fillers, and storage materials (supercapacitors) and, most recently, the construction industry is interested in using these materials [4]. The most common example of commercial applications of CNTs in Canada is for use as filler material in car paints and polymer composites [4]. This application made a new market for CNTs with a multibillion-dollar value in Canada. Polymers can be easily manufactured and incorporated with CNTs without damaging them to make CNT/polymer nanocomposites; these systems have reduced manufacturing costs compared to CNT/metal or CNT/ceramic composites [5]. The CNT/polymer composites can be categorized into structural and functional composites [4, 5]. The performance of these composites depends on many factors, such as CNT type, morphology, size, choice of polymer, the interfacial interaction between the polymer and CNTs and, most importantly, the appropriate dispersion of CNTs within the matrix. Uniform dispersion of CNTs in polymers is, therefore, a fundamental challenge for composites [5]. The attraction between untreated CNTs by van der Waals forces entangles them and consequently prevents them from being well dispersed within the polymer, causing the inappropriate mechanical performance of composites [5].

Another common potential application for CNTs is bioactive materials. CNTs benefit from their similarities to triple helix collagen fibrils in terms of size and shape (SWCNTs has responded more efficiently here, with a diameter in the range of 0.7-1.5 nm) [6]. Since their weight (1.6 g/cm^3) is lower than other candidates like stainless steel (SS, 7.7 g/cm^3), titanium (Ti, 4.506 g/cm^3), cobalt-chrome alloys (8.5 g/cm^3), and ceramic-based and metal-based materials, and their tensile strength, flexibility, and elasticity are greater than stainless steel, SWCNTs hold promise for use in the field of bone applications compared to the abovementioned traditional materials [7]. Nevertheless, the risk of CNT cytotoxicity is a major concern, which must be fully addressed before their use in the human body [8, 9]. Several parameters have been mentioned to explain the cytotoxic behavior of CNTs, such as their dimension, impurities (both metallic and carbonaceous impurities), functionality, functional groups density, and hydrophobicity leading to agglomeration [10].

It has been reported that most of the effective parameters in the cytotoxicity/biocompatibility of CNTs, such as hydrophobicity, functional groups, the extent of functionalities, ratios of length to diameter (aspect ratio), surface energy, and surface charge, can be controlled by a flexible and appropriate functionalization method. This ability has made functionalization or surface treatment

of CNTs the most promising method in reducing their cytotoxicity. The surface engineering of SWCNTs causes improved dispersion in culture media and prevents them from forming bundles or aggregates in the biological media. However, there is still the same contradiction about biocompatibility or at least less cytotoxicity of functionalized CNTs compared with untreated CNTs [11, 12].

Another example of their application can be supercapacitors. Supercapacitors are devices with the ability to store electrochemical energy. These devices mainly consist of an electrode, an electrolyte, and a separator. Carbon nanotubes can be used as a promising electrode in supercapacitors where they can store and properly deliver an electrical charge due to their high surface-to-volume ratio and high electrical conductivity, respectively [13].

Functionalization methods can be classified into two groups: wet chemistry and gas-phase (Surface engineering) methods. Wet chemistry approaches, such as acid treatments, suffer from multi-step and complex preparation methodologies. It was also proven that these methods damage the structure of CNTs [14]. These methods are also unfavorable for the industry because of their difficulties with scale-up, safety hazards, and tremendous waste containing CNTs [14].

Gas-phase methods are an alternative for surface modification, which can eliminate most of the abovementioned problems and are classified into several methods according to the applied energy resource for reaction initiation. Among them, photo initiated chemical vapor deposition (PICVD) is more affordable due to its simple procedure and lack of vacuum requirement. PICVD is an environment-friendly technique in which the reactions can be initiated by cheap lamps with low energy consumption, like UVC light. High efficiency, low energy consumption, and low deposition temperature are some other advantages of this method [3]. PICVD, which operates under (or near) atmospheric pressure utilizing UV-sensitive precursors, has been introduced as a potential approach to functionalize nano-materials [3]. However, to our knowledge, there has been no report on the treatment of CNTs over a full range of wettability (surface energy). By controlling the functionalization degree, it would be possible to obtain optimized wetting or dispersion of CNTs in the desired polymers depending on their polarity.

In this project, it was hypothesized that syngas/PICVD could potentially apply various densities of functionalities and consequently wettability on SWCNTs by controlling the operational parameters. In the first part of this dissertation, the capability of syngas/PICVD to treat SWCNT

surfaces is studied. The impact of operating parameters, such as flow rate, the molar ratio of H_2/CO precursors, pressure, the concentration of H_2O_2 as a photoinitiator, and substrate position inside the reactor are also investigated. In the second part of the dissertation, the focus is on the kinetics and reaction mechanism of syngas/PICVD along with an investigation of the temperature effects on the process. The gas- and surface-phase analysis provides insight into the structure of the film deposited on the surface. The dissertation is presented in 7 chapters:

- Chapter 1 provides a summary and introduction of the work.

- Chapter 2 provides a literature review regarding 5 main focal points of the dissertation: (1) carbon nanotubes, their properties, and applications, (2) synthesis methods of CNTs and their impurities as well as the purification methods of CNTs, (3) Potentials and risks of SWCNTs in bone application, (4) functionalization and surface treatment methods of CNTs, (5) PICVD and the effective parameters on it, and (6) common surface analysis methods.

- Chapter 3 highlights the objectives and sub-objectives along with the organization of the articles.

- Chapters 4 and 5 present two articles containing the main results of this study.

- Chapter 6 reports a general discussion with respect to the main results.

- Chapter 7 concludes the work, specifying the original contributions and recommendations for future work.

CHAPTER 2   LITERATURE REVIEW

2.1   Carbon Allotropes and CNTs

Carbon is one of the most abundant elements in the world. Carbon atoms are able to bond with other atoms and various levels of hybridization, such as sp^1, sp^2, and sp^3, which is why carbon can appear in different allotropes, such as diamond, graphite, C_{60}, C_{540}, amorphous carbon, graphene and CNTs [15] (Figure 1A). CNTs are allotropes of carbon in which graphitic sheets are rolled in a cylindrical shape [16].

CNTs are named according to their shell number as single-walled (SW), double-walled (DW), or multi-walled carbon nanotubes (MWCNTs) (2-50 walls) [17]. CNTs were first explored by Iijima in 1991. Their properties vary as a function of their angle of rotation (chirality) (Figure 1B). Accordingly, they can be classified into 3 groups: zig-zag, armchair, and chiral (Figure 1C) [18, 19].
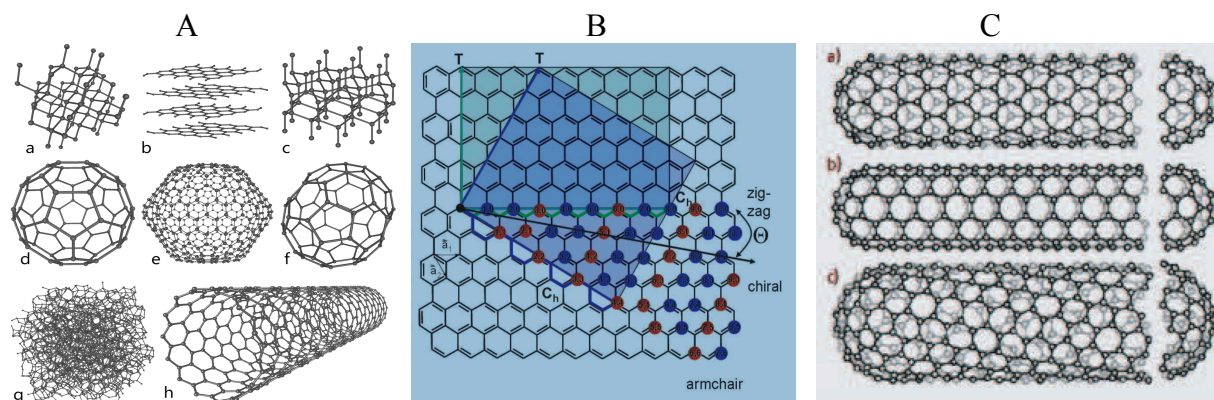
Figure 1. A) Different allotropes of carbon: a) diamond, b) graphite, c) lonsdaleite, d) C_{60}, e) C_{540}, f) C_{70}, g) amorphous carbon, h) SWCNT , B) Chirality of SWCNTs, C) Three different SWCNT structures a) zig-zag, b) armchair, c) chiral [19].

2.2   Properties of CNTs

CNTs have some specific characteristics, such as extraordinary mechanical properties (their tensile strength is predicted to be up to 200 GPa, 10-100 fold greater than stainless steel), electrical conductivity (92 S cm^{-1}) and remarkable thermal stability (up to 2800 °C under vacuum

and nitrogen) [6, 7]. Moreover, they have interesting optical features such as near-infrared optical absorption, high microwave absorption, stiffness, aspect ratio, and surface area [19-22]. Additionally, they have the highest Young's modulus or axial elastic modulus among all different types of composites and nano-materials. It is predicted to be 1-5 TPa [23, 24]. CNTs are very light with a density of about one quarter that of steel. It has been reported that CNTs are very flexible and can be twisted, elongated and bent before fracturing [25].

2.3   Synthesis Methods of CNTs

There are different methods for synthesizing CNTs. Chemical vapor deposition (CVD), arc discharge, and laser ablation are the most common [26-28]. Arc discharge method consists of breaking down a gas using electrical power to generate plasma [24]. The arc discharge chamber consists of an evaporated gas as the source of carbon molecules, a cathode electrode (normally graphite), an anode electrode (normally carbon powder) [24], and a metallic catalyst, such as Fe, Co, and Cu, is inserted into the anode electrode in the case of SWCNT synthesis (Figure 2A) [2, 3]. Carbon vapors aggregate and move toward the cathode to form a cigar-like structure at a temperature range of 3700-5700 ºC [29]. This method is cost-efficient but has little control over the alignment (chirality) of CNTs and leaves high levels of impurities [24]. Laser ablation utilizes an intense laser beam, which provides high temperature locally upwards of 9700 ºC (Figure 2B). At this temperature, the carbon source (graphite) and metallic catalyst particles (in the case of SWCNT synthesis) are transformed into a carbon/catalyst vapor, forming a plasma plume [29]. During the expansion of the plasma, it cools along a steep temperature gradient and the condensation of carbon-metallic catalyst atoms occurs to form larger structures. High-purity SWCNTs (>75%) can be synthesized by laser ablation, which is the main advantage of this approach [30]. However, the method's low efficiency limits it to the lab-scale [2, 3, 24]. Chemical vapour deposition (CVD) involves the decomposition of hydrocarbons, like methane, ethylene, acetylene, propylene, carbon monoxide, and benzene, in the presence of a catalyst (Figure 2C) [31]. CNT growth by this method takes place over the catalyst (typically transition metals, such as Ni, Fe, Co) within a temperature range of 300-1200 °C. CVD leads to CNTs in various forms, such as aligned, straight, thin films, powder, and even the complicated architecture of nanotubes by controlling the operating parameters, such as growth temperature, catalyst type, catalyst size, and carbon source [31]. Good control on the CNT diameter, number of shells, and

growth rate can be achieved with this method as there is a direct correlation between the diameter of SWCNTs and the size of the catalyst particles [31]. SWCNTs produced by CVD represent about 30-50% by weight of the final product, while for MWCNT this rate is closer to 30-99% by weight [1, 3]. CVD can be scaled-up to commercial scale as it is reported that this method can produce 100 g/h of SWCNTs [2]. The main disadvantage of CVD is the high defect density in the synthesized CNTs because of the comparatively low-temperature synthesis (vs. arc discharge and laser ablation). Accordingly, the tensile strength of the CNTs synthesized by CVD is only one-tenth of those made by arc discharge [1, 3]. It is a worth mentioning that the production of SWCNTs is more expensive and difficult than MWCNTs for several reasons. The synthesis of SWCNTs requires metallic catalysts, such as Ni, Fe, and Co, while MWCNTs can be produced without any catalysts. The synthesis can be even more complicated if a specific type of SWCNT (chiral, armchair, and zig-zag) is required. In this case, the effective operating parameters, such as the type of catalyst, solubility of carbon in the catalysts, growth temperature, and carbon-feeding rate, should be carefully selected and controlled. Sometimes, the desired chiral angles can be obtained using specific conditions [32]. For example, Lolli et al. (2006) synthesized SWCNTs with a specific chiral angle in a chemical vapor deposition (CVD) reactor using a CoMo catalyst on SiO_2 substrates. By changing the support for MgO, they could obtain SWCNTs with the same size but different chiral angles. They justified this behavior based on the interaction between depositing carbon and metal nanoparticles [33]. The significant dependency of SWCNT synthesis (in terms of the chiral angle) on the operating parameters (mostly the type of catalysts in the reactor) to grow a single tube on the catalyst particles makes their products more expensive, less pure with more defective sites on their hexagonal structure, and less efficient compared with the production of MWCNTs [24].
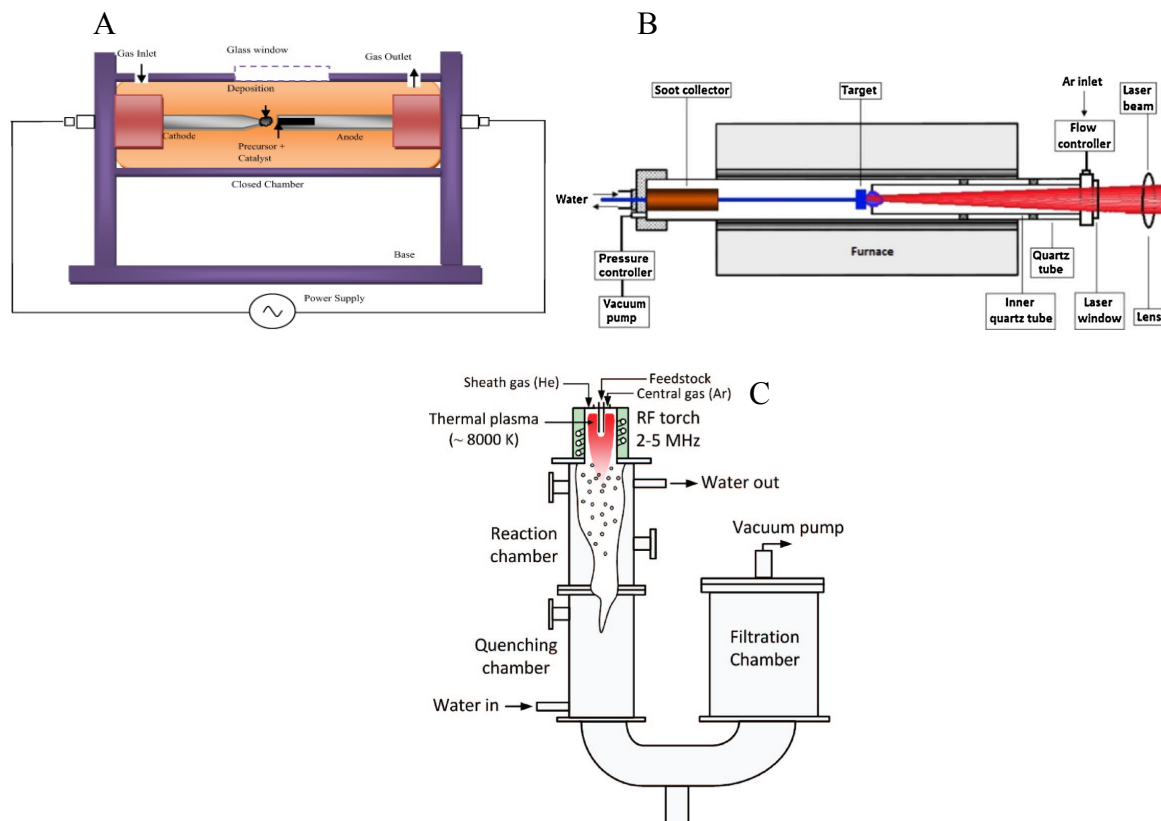
Figure 2. Schematic of A) arc discharge setup [29], B) laser ablation setup, C) CVD [30].

2.4 Impurities of CNTs and Purification Methods

Raw CNTs prepared by different synthesis methods inevitably contain some impurities, such as carbonaceous species and metal catalyst particles. Carbonaceous impurities are commonly in the form of amorphous carbon, fullerenes, and carbon nanoparticles (Figure 3) [6]. These impurities severely influence certain individual properties of CNTs, such as their electrical properties [34], and biocompatibility and, consequently, limits their applications [35-37]. Therefore, it is very important to know the type of impurities and the related purification methods. Purification methods are usually applied to remove these impurities. Purification methods of CNTs can be basically classified into two categories, namely chemical and physical methods. The chemical methods work based on the selective oxidation of impurities where the oxidation rate of carbonaceous impurities is faster than the oxidation rate of CNTs and/or oxidation of metallic impurities in acids, such as nitric acid (HNO_3) [2], sulfuric acid (H_2SO_4) [38], oxygen [3], hydrochloric acid (HCl) [2], and even a combination of acids (i.e., HNO_3 and H_2SO_4 [39]). Wet

chemistry, high-temperature annealing, and microwave heating are classified in the chemical purification methods. The physical methods work based on the differences in size, aspect ratio, magnetic properties of CNTs with impurities (such as metallic and carbonaceous impurities), and gravity. This method is able to remove graphitic sheets, carbon nano-spheres (CNSs), aggregates, and separate CNTs with different aspect ratios. Chromatography, filtration, centrifugation, and electrophoresis are classified in the category of physical purification methods. These methods are detailed in Appendix D.
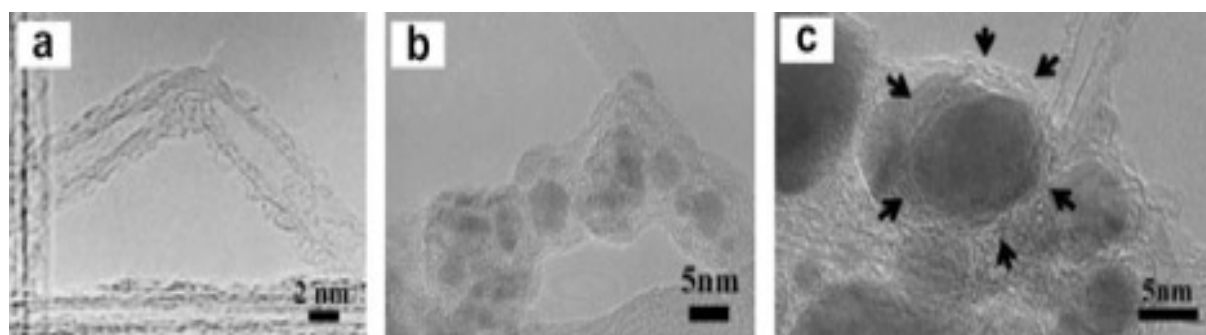
Figure 3. Transmission electron microscopy (TEM) images of (a) amorphous carbon and fullerene molecules on the surface of CNTs, (b) metal nanoparticles covered by amorphous carbon, (c) metal nanoparticles covered by graphitic carbon multi-layers [6].

2.5 Applications of CNTs

CNTs have various applications in different industries, such as electronics, aerospace, biotechnology, and medicine. Due to their individual properties, they have a strong potential to be used in biomedical applications. It was proven that they could also be used in drug delivery systems to release proteins, drugs, and DNA [40-42]. They have been used in imaging, treatment, and diagnosis applications, and particularly in cancer applications [41]. In the field of tissue engineering, they have been extensively used in bone researches [40-42]. Here, we focus our discussion specifically on the bone applications, as these explicitly highlight the impact of surface functionalization.

Bone is an active tissue composed of two material groups: the extracellular matrix (ECM) and bone cells. ECM is divided into the organic phase/osteoid, water, and inorganic/mineral phase. The organic phase is mostly composed of collagen type I (90% w/w) and ten percent non-collagenous protein [43, 44]. Current materials in bone applications can be classified into three

generations. The first generation of biomaterials was designed with the aim of matching materials with the desired tissue taking into consideration the mechanical and physical properties of materials. These materials have been mostly used since 1940 and been classified into metal-based, ceramic-based, and polymer-based materials. Stainless steel (SS), titanium (Ti) and cobalt-chrome alloys are the most popular ones of metal-based materials. The first generation of polymer-based materials was developed with the aim of anchoring the prostheses to the bones. PE, acrylic resins, and polypropylene (PP) are some examples of these materials [45].

The second generation of materials has been used since 1980. These materials have been developed to be bio-actively able to promote tissue/surface bonding and interact with the biological environments. Also, they were designed to be degraded along with the healing process. Calcium phosphate and bioactive glasses (BGs) are the most common ceramic-based materials. The reason for a material's bioactivity is their similarities with the mineral phase of bones with regard to structure and surface properties. In order to make the metals bioactive, two methods were proposed: coating by hydroxyapatite (HAP) or BGs and chemical modification of implants [45].

The third generation of materials is designed with the aim of higher bioactivity and to be bioabsorbable depending on the implantation site. The regeneration and repair of bones and the acceleration of the healing period are considered as the most important concerns of this generation. Another objective of this generation of biomaterials is to take advantage of removing drawbacks of the first and second generations of these materials, such as tissue infection, poor implant-tissue interface, fatigue, corrosion, poor flexibility, and heavyweight. Some examples of biodegradable polymers of the third generation are PGA, PLA, poly (ε-caprolactone) (PCL), polyhydroxybutyrate, and chitosan (CHI). Considering the above-mentioned properties, CNTs are one of the best options that can be replaced by the current bone materials [24, 45, 46].

SWCNTs have been identified as a strong candidate for bone applications, specifically because of their similarity with triple helix collagen fibrils in terms of size and morphology. SWCNTs are 0.7-1.5 nm in diameter and 200-1000 nm in length, while triple helix collagen is 1.5 nm in diameter and 300 nm in length [46, 47]. These nanostructures provide the roughness required for the bone cell function of osteoblasts (which contribute to bone synthesis) [46]. Another advantage is that the Young's modulus of SWCNTs is reported as being between 1 and 5 TPa. This modulus is even bigger than the one of MWCNTs (0.2-0.95 TPa) [48]. Young's modulus,

the ratio of stress to strain along the axis, is an important parameter in designing biomaterials. These benefits make SWCNTs a promising candidate for bone applications, especially for use as a scaffold to provide an appropriate surface roughness for a better *in vivo* function of bone cells (especially osteoblasts) [46]. It was demonstrated that CNTs are able to improve the mechanical properties of bone composites [22]. Additionally, applying SWCNTs can accelerate bone repair by using the electrical stimulation of SWCNTs in the desired area [49]. However, the mechanism for the related osteogenesis under electrical stimulation has not yet been fully understood [49]. As depicted in Figures 4A and 4B, due to their similarities with collagen (their rod-like shape and aspect ratio), they may be able to play the role of fibrillar proteins (collagen present as fibrillar proteins) in the ECM [22].
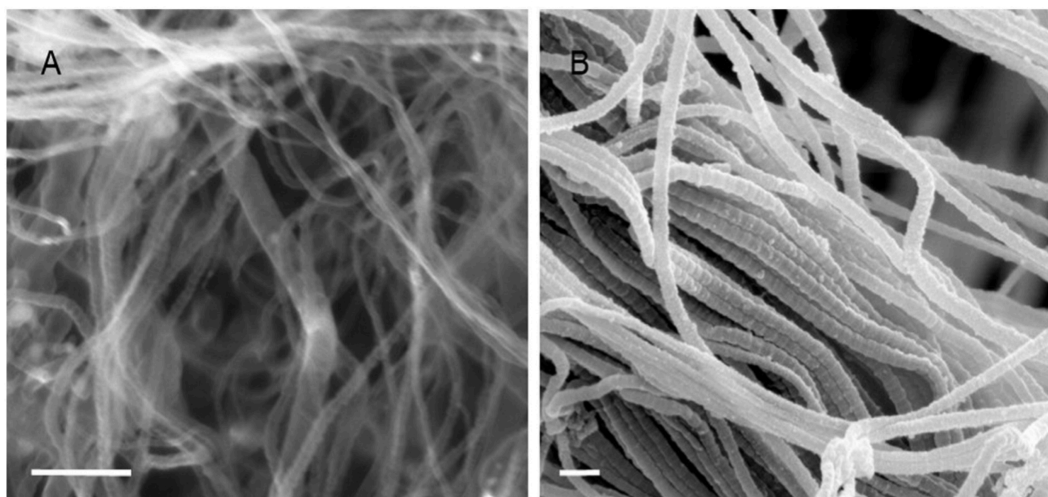
Figure 4. Scanning electron microscopy (SEM) image demonstrating the similarity between MWCNTs (A) and collagen (B) [22].

2.6 Cytotoxicity of CNTs

Cytotoxicity is the degree to which a substance can damage a cell. Cells exposed to a cytotoxic inducer undergo different reactions such as necrosis, in which their membrane is damaged, and apoptosis, in which cells activate specific intracellular pathways that control cell death [50, 51]. Despite all progress in biomaterials and all distinctive properties of CNTs, interaction mechanisms between CNTs and cells have not been understood yet and there is a contradiction about the cytotoxicity effect of CNTs. For example, Lobo et al. (2010) investigated the cytotoxicity of vertically aligned carbon nanotube (VACNT) scaffolds with SaOS-2 cell lines

derived from osteosarcoma, a type of bone cancer. These cancerous cells are commonly used as a model in bone cancer research. [52, 53]. The results revealed high cell adhesion for incubation periods of 6 h, 24 h, 48 h, and 7 days using SEM images and a high proliferation of cells attached to the VACNT scaffolds without any cytotoxic responses. The cell viability and cell proliferation were evaluated using the activity of lactate dehydrogenase (LDH). This enzyme is located in the cytoplasm of living cells and released when the cell membrane is damaged. LDH assay is commonly used to evaluate the cell cytotoxicity [53]. The same research group, Lobo et al. (2008), investigated the cytotoxicity of VACNTs for L-929 mouse fibroblasts in similar experimental conditions and found the same results, high adhesion and proliferation of cells in contact with the VACNTs [54]. In contrary, several authors reported the cytotoxicity of SWCNTs [55-57]. For example, Tian et al. (2006) reported the cytotoxicity of SWCNTs on human fibroblast cells (using MTT assay) in a dose-depended manner ranged from $0.06\,\mu g/ml$ to $0.6\,mg/ml$ (in vitro) [56].

Reading the literature revealed that the cytotoxicity of CNTs is caused by numerous parameters, such as their wettability, size, type, shape, degree of purity, functional groups, surface charge, and surface energy, etc. The cytotoxicity is considered in a dose-/time-depended manner in several studies [22, 55-57]. This is the main reason for the reported contradiction about the cytotoxicity of CNTs in which authors applied CNTs with different properties.

A closer look at the literature revealed that the same contradiction was reported on functionalized CNTs while the functionalization of CNTs is considered the most promising method for making them biocompatible [11, 12]. For example, functionalized SWCNTs using carboxylic acid groups were reported to be more cytotoxic and reduced cell viability and cell proliferation compared with non-functionalized ones [58-60], whereas Montes-Fonseca et al. (2012) reported less cytotoxicity for functionalized CNTs [61]. It is reported that CNT functional groups, the electrical charge of functional groups, and the extend of functionalities play a significant role in the cytotoxic response of CNTs [62]. For example, CNTs with positive charges in a dose-depended manner can negatively interact with cell membranes presenting negative charges and, consequently, cause cell lysis [62]. Table 1 summarizes a few studies in which functional groups and the related contradiction about their cytotoxicity have been investigated.

Based on the literature review, CNTs have not been treated yet over wide ranges of wettability,

which is the main reason for the contradiction regarding the cytotoxicity of functionalized CNTs. On the other hand, there typically has been no attention paid to the extent of functionalization in the literature and authors have mostly reported the cytotoxicity of CNTs based on one functionalization degree (a single treatment) [11, 12]. Surface wettability (which is reversely proportional to the surface energy) of SWCNTs derives their interaction with cells. It is indicated that the viability of a cells in contact with the hydrophobic CNTs is less than hydrophilic ones because of weak adhesive interactions between cell and CNTs leading to unsuccessful endocytosis. Since wettability is reversely proportional to the surface energy, we can make the same conclusion for it - Nanotubes with high surface energy can present a detrimental interaction with cells leading to an apoptosis or blood protein denaturation such as albumins and globulins [11, 12].

In addition to the above-mentioned explanations, most of the effective parameters on the cytotoxicity of CNTs, such as hydrophobicity, functional groups, the extent of functionalities, ratios of length to diameter (aspect ratio), surface energy, and surface charge, can be controlled by a flexible and appropriate functionalization method (it is a bonus if the wide range of wettability occurs based on a similar precursor). This is why functionalization has been named as the most promising method in reducing the cytotoxicity of CNTs.

Table 1. Effect of functional groups on biocompatibility or cytotoxicity of CNTs.

Functional Group	Type of CNT	Length μm	Diameter nm	Cell	Dose μg/mL	Purified	Results	Ref
COOH	SW & MW	5-15	SWCNT<2 MWCNT<5	MSCs	3-30	Yes	COOH-SWCNTs inhibit proliferation and differentiation of MSCs.	[63]
COOH	MW	10-30	10-20	Human normal liver cell line (L02)	12.5-200	>95%	Cytotoxicity of MWCNTs can be reduced by carboxylic groups compared to Pristine CNTs.	[58]
OH, NH$_2$, PEG, COOH	SW	-	-	Human breast cancer cell line (MCF7)	0-80	Yes	All functionalized SWCNTs showed significant impact on the ROS formation and mitochondrial activity. However, all samples could induce cell membrane damage and increase cell apoptosis.	[64]
NH$_2$, COOH	MW	-	20-30	Mouse fibroblast cell line (L929)	1-100	Yes	Functionalized MWCNTs did not show any cytotoxic effect up to 50 μg/mL.	[65]
COOH	MW	-	60	Human umbilical vein endothelial cells (HUVECs)	>100μg	Yes	COOH-MWCNTs decrease the viability of HUVECs.	[66]

2.7 Functionalization Methods of SWCNTs

Adding functional groups to materials is called functionalization. When the target for these functional groups is the surface of materials, this is identified as surface engineering. There are several methods to functionalize and surface engineer CNTs. These methods can be categorized

into covalent (in which functional groups are attached to the surface through a chemical bond) and noncovalent (in which functional groups are physically adsorbed on the surface) methods based on the type of attachment of functional groups to the target materials. They are also categorized into liquid- and gas-phase functionalizations based on the reaction environment (liquid phase methods are normally responsible for bulk functionalization and gas phase methods are responsible for surface treatment). In the case of CNTs, the functionalization can also be classified into i) endohedral in which functional groups are added inside the tubes or ii) hexahedral in which functional groups are added on the surface (Figure 5) [67]. Deposited atomic layers can be called a thin film when the film thickness is 1 μM (or less) or a coating when the thickness is greater than 1μM. The properties of thin layers/coatings can be strongly affected by the thickness of the coating and substrate. Accordingly, the deposited films can be pure/impure, dense/scattered, amorph/crystallized, or thin/thick [68].
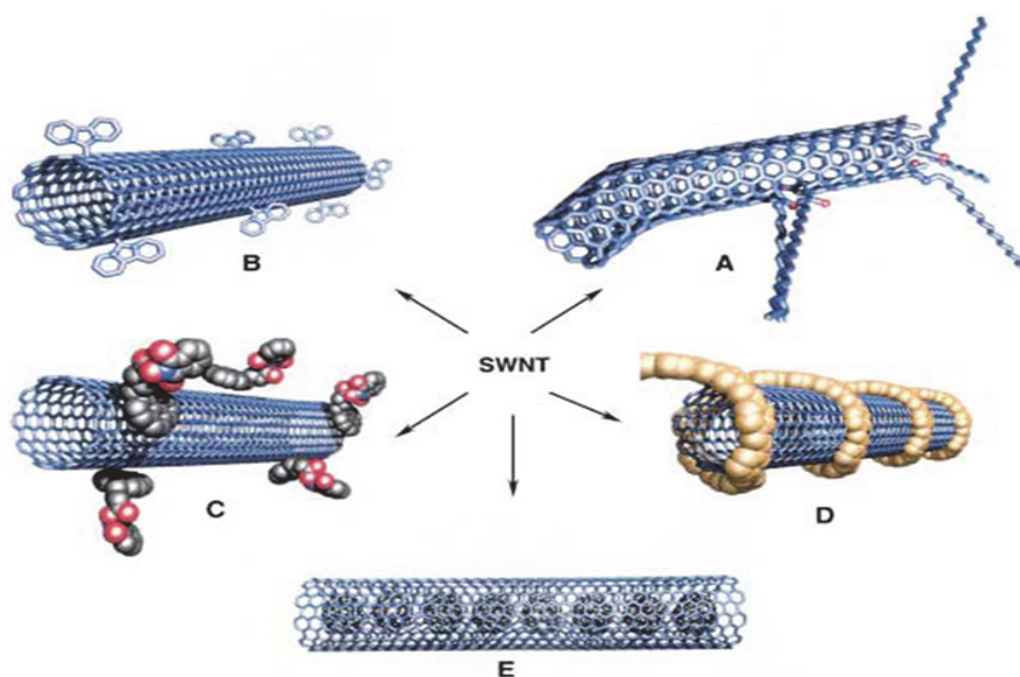
Figure 5. Different types of liquid functionalization, A) defect group functionalization, B) covalent functionalization of sidewall, C) non-covalent functionalization with surfactant, D) exohedral functionalization (non-covalent) with polymer, E) endohedral functionalization [67].

2.7.1 Liquid-Phase Methods

Liquid methods utilize oxidizing chemical reagents under thermal conditions to add organic

functionalities to nanoparticles or CNTs. They can be applied on a relatively large-scale. A multi-stage process, including acid refluxing, sonication, centrifugation, and filtration, in addition to huge industrial liquid waste and by-products make these methods unfavorable for the industry. Additionally, these methods alter the structure of CNTs and induce a lot of defect sites on the hexagonal structure of CNTs. For example, Ramanathan et al. (2005) functionalized SWCNTs with amine groups using a multi-step liquid phase procedure [69]. Accordingly, they first treated SWCNTs with a sulfuric/nitric acid mixture (3:1 v/v%). Then, the oxidized samples were sonicated for 3h at 40 ºC. The mixture was then filtered through a polycarbonate filter membrane (10 μm pore size) and dried in a vacuum (4h). The carboxylated SWCNTs further dispersed in ethylenediamine/N-[(dimethylamino)-1H-1,2,3-triazolo[4,5,6]pyridin-1-ylmethylene]-N-methylmethanaminium hexafluorophosphate N-oxide (HATU) mixture and sonicated for 4h. The amine functionalized SWCNTs became ready after passing through a 10 μm pore-size membrane and drying under vacuum [69].

2.7.2 Gas-Phase Methods

Surface engineering or gas-phase treatments are methods in which functional groups are deposited from gas precursors onto the target surface, according to a combination of gas and surface phase reactions. The deposited functional groups can be attached to the surface physically (like deposited periodic polyethylene (PE) oligomers on individual CNTs [70]) or chemically (like deposited amino groups on the CNT surfaces [71]). According, they can be categorized into physical vapor deposition (PVD) or chemical vapor deposition (CVD) processes.

2.7.2.1 PVD Processes

PVD (also called the overlay process) is a method in which the atomic layers can be deposited on the substrate atom-by-atom. In this process, the depositing materials are vaporized from a liquid/solid state and then brought to the surface using a high vacuum and finally condensed on the surface. The resulting deposited film can range from a thin film (≤ 1 μM) to a coating (>1 μM) on the substrates with various sizes (very small to very big) and shapes (flat or complex geometry). PVD is mostly used for deposition films from elements (like carbon (C), Titanium (Ti), and Magnesium (Mg)) and alloys (like copper:gold (Cu:Au) and aluminum:magnesium (Al:Mg)) [68]. This process can be classified to sputter, vacuum, arc vapor, and ion plating

deposition regarding the type of processing. Vacuum deposition is a type of PVD process in which the materials are thermally vaporized and then reach the substrate surface under $10^{-5} – 10^{-9}$ Torr vacuum without any significant collisions between gas molecules and precursor vapors. This method is commonly used for decorative mirror coatings, flexible packaging, and conductive coatings [68, 70]. In the sputter deposition, the deposition of particles happened from a solid substrate through physical sputtering. The required vacuum for the sputtering particles is <5 mTorr. Arc vapor deposition utilizes a low voltage arc to vaporize an anodic or cathodic electrode and deposit the vapor on the surface. This method is commonly used for hard coatings. In the ion plating process, depositing films are exposed to a continuous or periodic bombardment of energetic particles (usually made of either a reactive or natural gas) in order to be modified. The ion plating process is normally used for hard coatings from compound materials. The high temperature, high vacuum, and cooling system requirements make the PVD process costly for the industry. The PVD process has been rarely used to treat nanoparticles and CNTs. As an example, Li et al. (2006) deposited periodic polyethylene (PE) oligomers on individual CNTs [70]. Periodic patterning on CNTs is a great interest for many researchers because it is a necessary step toward building nanodevices based on CNTs [70].

2.7.2.2 Chemical Vapor Deposition

Chemical vapor desposition (CVD) is a method in which film deposition can be done using the reduction or decomposition of gas phase precursors containing the target materials for the deposition (Figure 6). Decomposition of gas-phase precursors can be obtained at a high temperature while a partial decomposition can also be reached under plasma (energetic ions) and energetic light photons. In CVD, gas and surface reactions lead to film formation on the substrate surface. From an economic point of view, this method is more affordable and favorable than wet chemistry methods because of the lack of liquid waste, less hazard, inexpensive precursors, and rapid procedures [3, 23]. The quality and quantity of the depositions (thin films or coatings) can be adjusted by varying the operating conditions, such as temperature, pressure, and ratio of precursors. Based on the initiation source for the reactions, CVD can be classified into three main categories: plasma enhanced chemical vapor deposition (PECVD), thermally activated chemical vapor deposition (TACVD), and photo-initiated chemical vapor deposition (PICVD) [3].
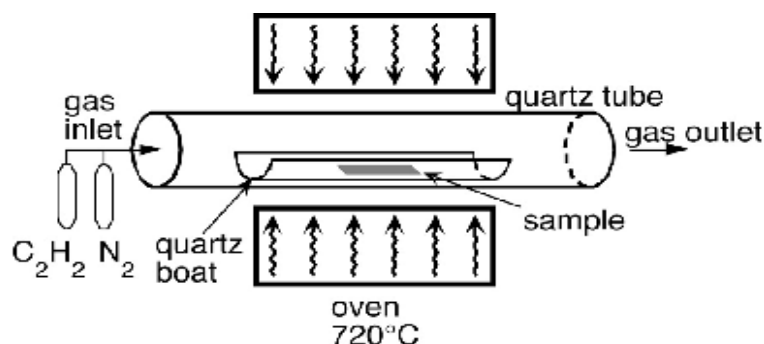
Figure 6. Schematic of a CVD process [3].

2.7.2.3 TACVD Method

TACVD or Hot-Wire CVD (HW-CVD) is a CVD process in which a heating source is used to initiate chemical reactions. Normally, heat is employed as a resource of energy, which can be provided from infrared radiation, inductive heating, or electrical resistivity. In this method, the monomers or the substrate surface (or both) are heated to produce reactive species or intermediates (free-radicals, cations, and anions). Solid film deposition occurs on the surface. This technique works at high temperature (>600 ℃), which can be the main disadvantage of this method. Applying a high temperature makes a limited range of monomers for this technique. On the other hand, the substrate should tolerate the high temperature that cannot be applied to a vast range of substrates (Figure 7A) [3]. This technique (TACVD) has been mostly developed in the semiconductor industry in which a high deposition rate is required [3].
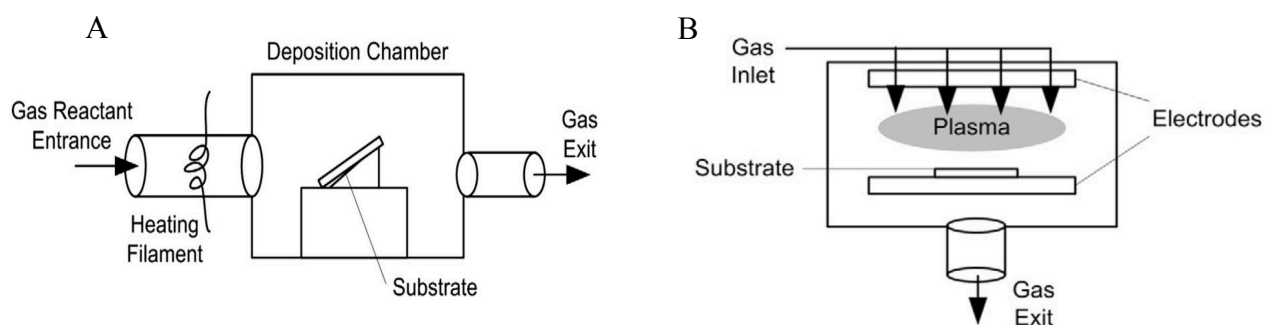
Figure 7. Schematic of A) HWCVD process, B) PECVD process [3].

2.7.2.4 PECVD

Plasmas can be used in CVD reactors for the partial decomposition or activation of gas-phase precursors. This process is called PECVD or plasma-enhanced chemical vapor deposition. This method is normally used in the semiconducting industries with the reported deposition rate of 5-10 nm in minutes [68]. However, this process can also be used for polymerization reactions in the reactor when the precursor is a monomer and can be crosslinked in plasma and on the surface. The resulting plasma films present appropriate surface coverage and low porosity [68]. In PECVD, electrons or ions derived from the plasma state will be used to initiate polymerization reactions and to form the coating films. This process utilizes a combination of electrical power and light emission to produce a glow discharge plasma (composed of excited species and ions). In this method, free radicals and reactive ions will be produced by a direct collision in the low-pressure plasma (high energy electrons). Working at lower temperatures than TACVD for reactions, accurate control over the coating structure, and short reaction times can be mentioned as the best advantages of this technique (Figure 7B) [3, 72]. However, PECVD suffers from some disadvantages, such as the vacuum requirement, low purity of depositions due to trapped precursors (they are not desorbed completely so they remain unreacted), low cross-linked film structures due to short reaction times, and low efficiency (due to wasting energy for species with insufficient energy) [3, 72]. PECVD processes usually need complicated reactor designs considering the applied discharge plasma. The requirements for a vacuum and sophisticated reactor design make this technique expensive [73]. This process is extensively used to treat CNTs [71, 74-78]. As an example, Yook et al. (2010) treated CNT films using PECVD. They successfully added amine groups on the CNT surfaces while NH_3 was used as the precursor [71].

2.7.2.5 PICVD

Photochemical methods, similar to the cold plasma approach, utilize light to initiate reactions [79]. Unfortunately, there is not a lot of information about the PICVD and this technique is mostly developed on semiconductor industries. Ozone ultraviolet (Ozone/UV) treatment or ozonolysis can be the first example of photochemical treatments of nanoparticles, which is able to add organic functional groups on the nanoparticle surfaces. This technique has not been referred to as photopolymerization but has been extensively used to treat nanoparticles, especially CNTs (both MWCNTs and SWCNTs) [80-83]. It is indicated that UV light is able to excite

molecular oxygen from its ground spin-triplet state into a higher energy level, which is a spin-singlet state [80, 81]. This excitation leads to a lower activation energy for the chemisorption of molecular oxygen on the CNTs [80]. For example, Raja (2015) investigated the surface treatment of SWCNTs using ozone/UV treatment. They reported the successful surface functionalization of SWCNTs by carboxylic acid functional groups [83]. Cai et al. (2002) reported a variety of functional groups, such as carboxylic acids, esters, and quinone moieties, on the SWCNT surfaces after 180 min of ozone/UV treatment [84]. This technique is destructive for the hexagonal structure of CNTs and there is limited control on the extent of hydrophilicity [85-87].

Vacuum-ultraviolet (VUV) is another example of photochemical treatments of nanoparticles, which refers to the photopolymerization reactions. During the past decade, there have been a few research groups, such as Wertheimer et al. [88, 89], Girard-Lauriault et al. [90, 91], and Scherzer [92, 93], who worked on the VUV treatment of nanomaterials. Truica-Marasescu et al. (2007) from the Wertheimer group used the VUV technique to add nitrogen groups to the polyethylene surface. For this matter, they used Kr and Xe lights to initiate the photopolymerization reactions while a combination of C_2H_4, CH_4, and NH_3 was used as the precursor [89]. Ruiz et al. (2010) from the same group later reported nitrogen and oxygen enrichment of the polyethylene film surface while C_2H_4/N_2O and C_2H_4/NH_3 were used as the precursors [88]. Girard-Lauriault et al. (2012) investigated the functionalization of graphite sheets (99% (w/w)) and Raw-MWCNTs (R-SWCNTs) under VUV (Kr: 123.6 nm, delivered intensity of 95 mW/cm^2) irradiation using NH_3 or O_2 as UV-sensitive precursors [94]. They quantified amine and hydroxyl functional groups using two reagents, including 4-fluoroethylene benzaldehyde (TFBA) and trifluoroacetic anhydride (TFAA) utilizing X-Ray Photoelectron Spectroscopy (XPS) and derivatization reactions. The results revealed the successful deposition of nitrogen- or oxygen-containing groups on both graphite and MWCNT [94]. The greatest disadvantage of the VUV technique is the absorption in the air. This limits the options (such as MgF_2 and LiF_2 which are transparent to the wavelength of below 200 nm) to choose reactor windows [3].

We refer PICVD to the photochemical reactions in which energetic free radicals drive the reaction pathway and initiate chain reactions leading to polymerization. Radicals in PICVD processes can be created by initiators or monomers when they are exposed to energetic light photons (Figure 9). Therefore, a series of heterogeneous chain reactions occur on the surface of the substrate and in the gas phase regime [79]. This process can be classified into two categories,

free radical and ionic polymerizations regarding the type of deriving radicals. Ionic polymerization itself can be categorized as anionic and cationic polymerization. In the case of free-radical polymerizations, free radicals determine the reaction pathway while in ionic polymerizations this role is played by cations and anions, respectively. The mechanism of radical polymerizations comprises three stages: initiation, propagation, and termination.

For the first time, Tavares et al. (2014) introduced the syngas/PICVD technique in order to add oxygen-containing functionalities on the metallic flat substrates, such as Cu [72]. This technique utilized syngas as the precursor and H_2O_2 as the UVC sensitive photoinitiator. They used a simple setup consisting of two UVC lamps with the major peak emission of 254 nm, a plug flow reactor, an injection system for the liquid photoinitiators, and syngas cylinders (Figure 8). The authors reported successful incorporation of oxygen-containing groups on the metallic flat surfaces mostly based on the physical characterizations, such as tensiometery (contact angle measurements). They also suggested a primary reaction pathway for the syngas/PICVD [72]. Farhanian et al (2017) from the same group investigated the syngas/PICVD treatments of flat silicon substrates in order to understand the chemistry behind this technique. The authors revealed the compositional structure of coatings resulting from the syngas/PICVD treatment. They suggested a deposition rate of Y=0.7t (t is time (min) and Y is deposition thickness (nm)) and a reaction pathway for the syngas/PICVD technique based on the surface analyses [95].

Nasri et al. (2017) from the Tavares research group reported the presence of iron pentacarbonyl ($Fe(CO)_5$) in CO cylinders as an impurity and Farhanian et al. (2017) selected $Fe(CO)_5$ in their suggested reaction pathway [95, 96].

Syngas/PICVD has several advantages, including affordable cost, due to its simple procedure and lack of vacuum requirement. PICVD is an environment-friendly technique with high efficiency. The efficiency is coming from its controlled deposition rates, low energy consumption, and low deposition temperature. Like PECVD, the quality and quantity of deposition films can be easily adjusted by operational parameters in comparison to other CVD techniques [3]. This technique has not been used for the surface treatment of CNTs and still suffers from a lack of information about the mass balance or a gas phase analysis. Table 2 summarizes the differences between the presented methods (advantages and disadvantages).
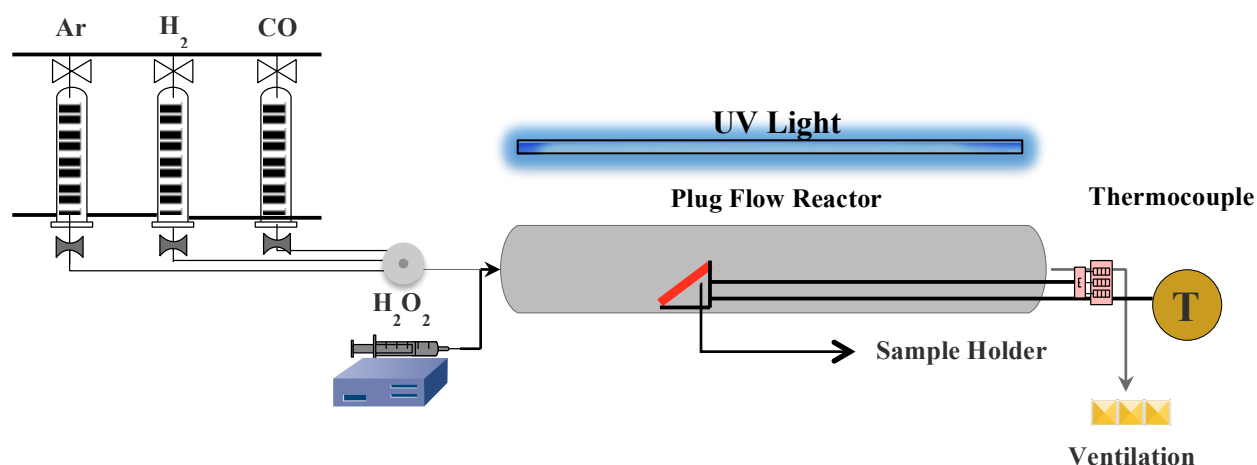
Figure 8. Schematic of a PICVD process.

2.8 Effective and Operational Parameters of PICVD

Several parameters affect the formation of deposited films in PICVD, such as reactor pressure, reaction time, type and flow of photoinitiator (PI), and ratio of PI to monomer (PI/M), type, shape, structure and viscosity of monomers, ratio of precursors (in the case of binary systems, such as those using CO/H_2), flow of monomers, extent of oxygen in the reactor, reactor temperature and substrate temperature, position of substrate inside the reactor, confirmation of reactor and substrate, and wavelength, intensity and photon flux of the light [89, 97, 98]. Some of the main parameters are explained in the following.

Table 2. Comparison of different functionalization methods.

Methods	Advantages	Disadvantages	Ref.
Wet Chemistry	1. Easy scale-up 2. Relatively low-cost method 3. Covalent bonding between functional groups and substrates	1. Time-consuming process 2. Multi-step Process 3. A lot of hazardous waste will remain 4. Destructive for the structure of CNTs	[3, 99, 100]
PVD	1. Easy scale-up 2. High deposition rate	1. Non-covalent bonding between functional groups and substrates 2. High-temperature requirement 3. High vacuum requirement 4. Cooling system requirement 5. Expensive method	[70]
TACVD	1. Simplicity 2. Covalent bonding between functional groups and substrates 3. Easy scale-up 4. High deposition rates and conversions	1. High-temperature requirement 2. Low energy 3. Monomer limitation 4. Expensive process	[3, 101]
PECVD	1. High deposition rate 2. Wide available range of monomers 3. Covalent bonding between functional groups and substrates 4. Control on deposition temperature 5. Easy scale-up	1. Vacuum requirement 2. Low cross-linked depositions 3. Expensive method 4. Low efficiency 5. Unreacted precursors and by-products, often embedded in functional coating	[71, 77, 101-103]
PICVD	1. Working at near atmospheric pressure 2. Working at room temperature 3. Easy scale-up 4. Inexpensive process 5. High cross-linked depositions 6. High-quality films due to low excitation energy 7. Low energy consumption and high selectivity (because of mono-energetic photons)	1. Low reaction rate and low conversion	[3, 95, 99]

2.8.1 Light Source

Light is the most important part of the PICVD system, as it acts as a source of excitation for precursors (and if necessary, initiators). Common UV lamps emit a photon energy of 4.88- 15 eV, which is capable of dissociating many chemical bonds. There are several parameters, which should be considered, such as light intensity, light wavelength, and photon flux. By increasing light intensity, higher reaction rates can be observed [104]. For example, Behnajady el al. (2006) studied the photodegradation of C.I.AcidYellow23 (AY23) in the presence of ZnO as a catalyst.

The results showed that the reaction kinetic rate constants increase with increasing light intensity [104]. UV wavelengths range from 74 nm up to 400 nm. The light source and its specific emission profile will depend on the desired precursors and their binding energy. UV lights can be classified based on wavelength into the following three classifications, UVC (100-280 nm), UVB (280-320 nm) and UVA (320-400 nm) [105, 106].

2.8.2 Precursor Selection

Precursor selection is the most important parameter in the PICVD while the properties of resulting coating are affected by it. Precursor selection depends on applying light intensity, light wavelength (UV, visible light, etc.), and the type of reactor lead directly to the desired functionality, and surface wettability [73, 98, 107].

The preliminary conditions for selecting a precursor are a high absorption cross-section in the desired wavelength range and the appropriate double bond density that will be attacked by the radicals for an efficient propagation step and the desired functional groups (this is necessary in the case of polymerization in which a hydrocarbon is in high demanded.). For example, to work under UVC light (as the energy source of reaction initiation) with a major peak emission wavelength of 254 nm, the selected monomer has to have an appropriate light absorption at this wavelength. In the precursors with a significant absorption cross-section, the cleavage of the precursors' C=C double bonds (or other desired bonds) happens when the energy of an incident photon is higher than the bond dissociation energy of the double bond or any other target bonds. Table 3 presents some of the gas-phase precursors that worked under the appropriate spectral range (VUV or UVC).

Sulfur containing monomers, like hydrogen sulfide (H_2S), can lead to thiol groups. Gaseous H_2S has a significant absorption in the wavelength range of 120-250 nm (Figure 9A). This molecule has a good overlap with the VUV spectral range leading to the dissociation of the H-SH bond with the binding energy of 3.6 eV (Incident of this molecule with energetic photons with hv>4 eV leads to a S-H bond cleavage) [91]. As Table 3 presents, oxygen-containing groups including hydroxyl and carboxylic acid can be produced by gaseous oxygen (O_2) and ozone (O_3) precursors, respectively. As mentioned before, ozone/UV is a popular method for functionalizing CNTs [81]. Gaseous O_2 is also used for the treatment of MWCNTs under VUV light in order to

enrich their surfaces with hydroxyl groups [94]. Gaseous hydrocarbons, such as Methane (CH_4), ethylene (C_2H_4), and acetylene (C_2H_2), have been used for the polymer formation. These molecules present an appropriate absorption in the VUV spectral range (Figure 9A-C). Some properties of these common hydrocarbons (CH_4, C_2H_2, C_2H_4), such as binding energy and required wavelength for their bond dissociation, are presented in Table 3 [88, 89, 91]. In the hydrocarbon precursor selection, the double bond present in the molecule creates a bonus for the photochemical reactions. If a precursor has the appropriate double bond density and absorption cross-section simultaneously, we can expect self-initiating photo-polymerization systems in which there is no need to use photo-initiators. Otherwise, a photo-initiator (PI) is needed in the polymerization system, to be able to make energetic and reactive species, including free radicals, cations, and anions (initiation step). The reactive species can make the reactions progress further (propagation step) until they react together (termination step). [73, 98]. Nitrogen-containing monomers, like ammonia (NH_3) and nitrous oxide (N_2O), can lead to amine functional groups. For example, NH_3 has a strong absorption in the wavelength range of 112-220 nm (Figure 9C). Energetic VUV photons with the photon energy of $h\nu > 6.2$ eV are able to dissociate D0 ($H-NH_2$) with the bonding energy of 4.4 eV. Amine groups can be stated as the most probable products of NH_3 photolysis. This molecule is applied to add nitrogen-containing groups on the MWCNT surfaces under VUV light [94].

In the case of surface wettability, hydrocarbon or fluorine-containing groups lead to hydrophobic coatings while oxygen or amine-containing groups lead to hydrophilic surfaces [98]. There are some other effective parameters on the precursor selection, such as viscosity, molecular structure, solubility, molar absorption coefficient, and functionality, that should be taken into account to select precursors [98].

Table 3. Common gas-phase precursors with their related bond energy and dissociation

Precursor	Dissociation Energy (eV)	Absorption Range (nm)	Required Wavelength for Bond Dissociation (nm)	Major Target Functionalities	Target Substrate	Ref.
H_2S (D_0 H-SH)	3.6	120-250	VUV (10-200 nm) ($h\nu$ >4 eV)	Thiol Groups	Silicon	[91]
O_2 (D_0 O-O)	1.5	110-180	VUV (10-200 nm)	Hydroxyl Groups	MWCNTs	[94]
O_3 (D_0 O-O)	1.05	100-350	VUV (10-200 nm)	Carboxylic Acid Group	MW- and SW-CNTs	[81] [72, 73].
CH_4 (D_0 H-CH_3)	4.5	110-144	VUV (10-200 nm)	Hydrocarbons	Polyethylene	[89]
C_2H_4 (D_0 $H_2C=CH_2$)	6.9	110-185	VUV (10-200 nm)	Hydrocarbons such as acetylene	Polyethylene	[89]
C_2H_2 (D_0 HC≡CH)	8.7	123-184	VUV (10-200 nm) $h\nu$ >5.8 eV	Hydrocarbons	Silicon/ Polyethylene	[91]
NH_3 (D_0 N-HN_2)	4.4	112-220	VUV (10-200 nm) ($h\nu$ >6.2 eV)	Amine Groups	MWCNTs	[94]
N_2O (D_0 N≡NO)	9.8	120-153	VUV (10-200 nm)	Nitrogen-Containing Groups	Polyethylene	[88]
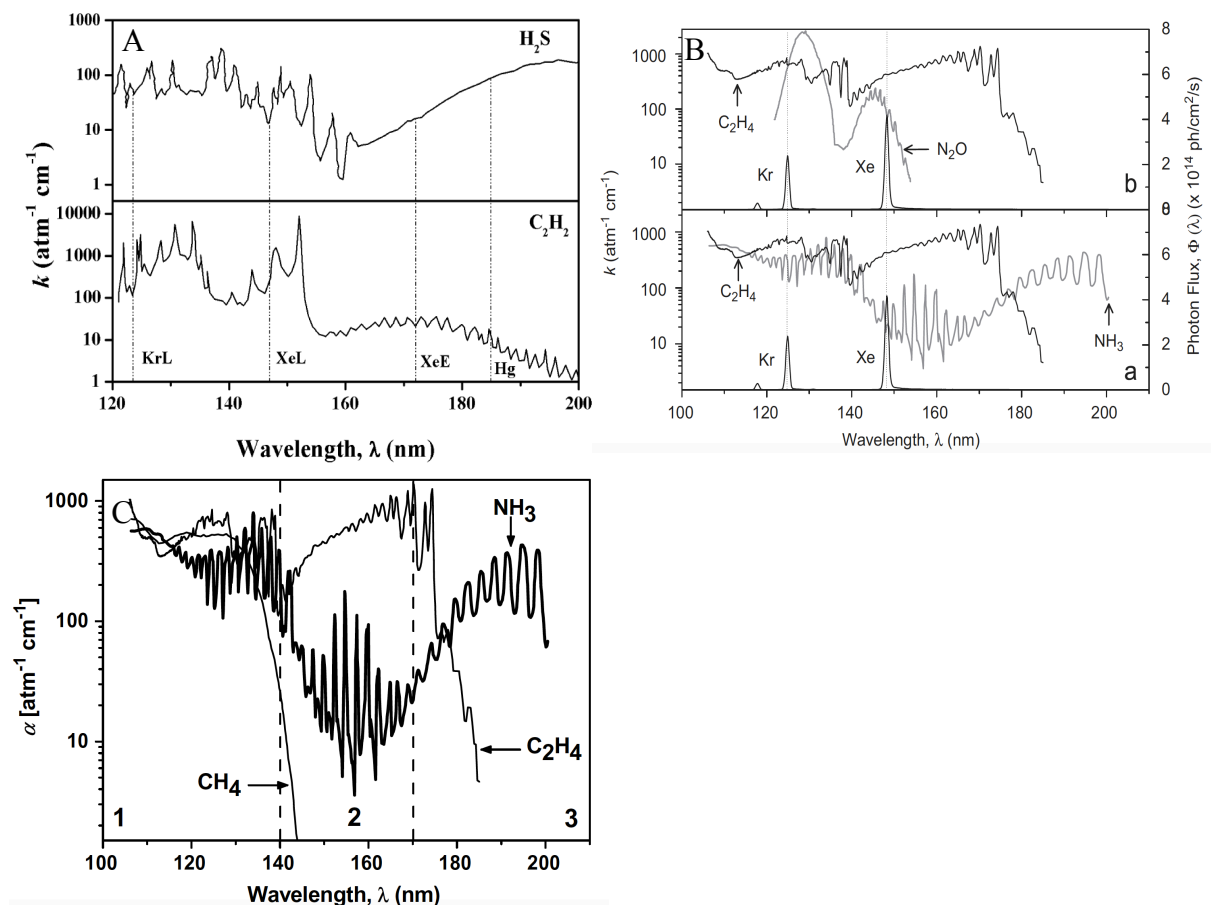
Figure 9. Absorption cross-section of A) H_2S/C_2H_2 system in order to add thiol groups on the silicon flat surfaces [91] , B) C_2H_4/N_2O and C_2H_4/NH_3 in order to add oxygen- and nitrogen containing polymers on polyethylene [88], C) $CH_4/C_2H_4/NH_3$ system in order to add amine containing polymers on polyethylene [89].

2.8.3 Initiation Systems

The initiation of polymerization reactions usually occurs by Photo-initiators (PIs). However, some liquid monomers, like acrylates, contain a lot of carbon-carbon double bonds, which can easily undergo bond cleavage. In addition, they have an appropriate absorption cross-section in a wide range of spectra. They are well known as self-initiating monomers that can be used as PI. Initiators can be divided into two classifications: Type 1 or radical PIs and Type 2 or ionic PIs (cationic or anionic). Radical PIs (Type 1) are UV-sensitive substances, which have the ability to produce free radicals leading to radical polymerization reactions in which monomers with low molecular weight convert to high cross-linked films [98]. Ionic PIs (Type 2) also initiate

polymerization reactions by creating positive or negative ions. This kind of polymerization was identified to be more stable [98]. PIs in the polymerization reactions can lead to faster curing rates based on their rate of initiation, more photosensitivities due to their molar absorption, and polymer properties depending on their type of radicals [97, 98].

Radical initiators can usually initiate the reactions in two pathways, one of which is photo-fragmentation (Class 1) where two radicals are formed by an α-cleavage mechanism (Figure 10). Aromatic carbonyl compounds, such as hydroxyalkylphenones, benzil ketals, and acylphosphine oxides, are great examples of these types of initiating systems [97, 108].
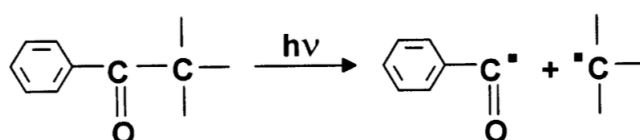
Figure 10. Class 1 initiating system undergoes a homolytic C-C bond dissociation upon UV exposure **[97]**.

The H-atom abstraction (Class 2) is the second initiating pathway in which the R• radical is formed by abstracting a hydrogen atom coming from a hydrogen donor molecule, such as amines, alcohols, and ethers (Figure 11). Thioxanthones, phenylglyoxalates, aromatic diketones, camphorquinone, and benzopehnone are some examples of this type of initiating system among which benzophenone is the most common one [97].
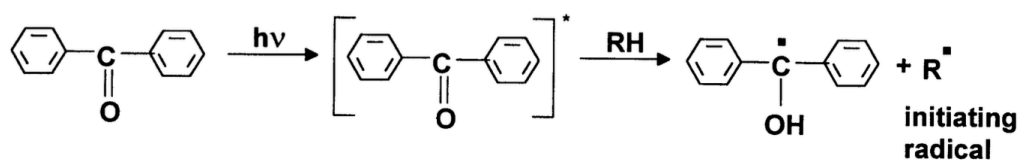
Figure 11. Class 2 initiating system undergoes an H-atom abstraction upon UV exposure **[97]**.

Hydrogen peroxide is a liquid example of the radical PIs, which are capable of breaking down radicals into two hydroxyls (OH•) under UV light. H_2O_2 is a non-polar molecule with a binding energy of 2.15 ± 0.02 eV and 3.84 ± 0.1 eV for HO-OH and HO_2-H, respectively. Based on the absorption coefficient of the molecule shown in Figure 12A, it seems that the most important absorption occurs in the wavelength range of 150 nm up to 410 nm. The primary photo-dissociation reaction of this molecule can be defined as $H_2O_2\rightarrow2OH\bullet$. Two free radicals can be

produced by its dissociation, which can play a significant role in leading radical polymerization [72, 73].

Ozone is a gas-phase precursor which can be serve as a gaseous PI. Ozone is a bent molecule with a binding energy of $(D_0= (O-O_2))$ 1.05±0.02 eV and an angle of 116.8°. This molecule has a significant photo-absorption with an efficient quantum yield at the wavelength of 254.7 nm (Figure 12B). High reactivity, toxicity, and UV sensitivity are some of its properties [72, 73].

Iron pentacarbonyl $(Fe(CO)_5)$ is a liquid metal compound which is sensitive to heat and light. This compound can be formed inside the carbon monoxide (CO) cylinders at high pressure (>20 MPa) through the reaction between iron and CO. $Fe(CO)_5$ decomposes at a low temperature (230 °C) into some reactive radicals such as $Fe(CO)_4$, $Fe(CO)_3$, or Fe. Photocatalytic behavior of $Fe(CO)_5$ in the polymrization reactions (in tshe yngas/PICVD method) is reported by Nasri et al (2017) from Tavares group. They reported that $Fe(CO)_5$ is able to accelerate and govern the radical chain reactions in syngas/PICVD [96]. Table 4 presents a list of common PIs working in the UV wavelength range.
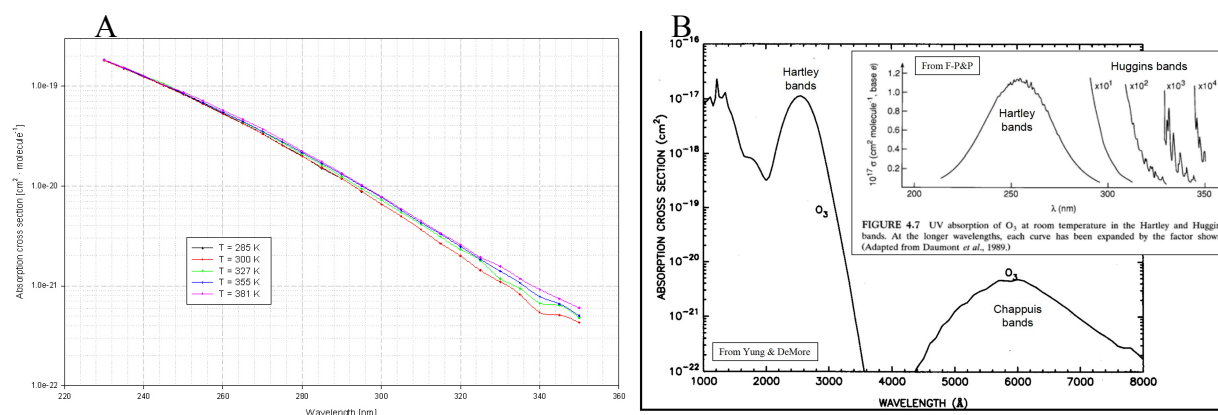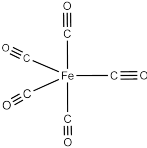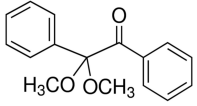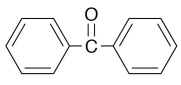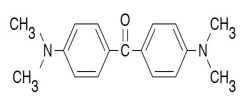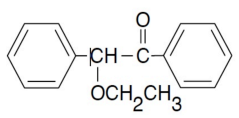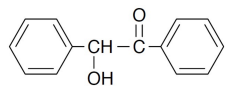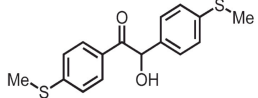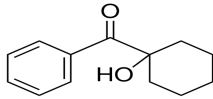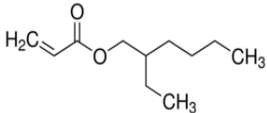
Figure 12. A) Absorption cross-section of H_2O_2, B) Absorption cross-section of ozone.

Table 4. Photo-initiator and photo-sensitizers used for radical photo-polymerization.

Name	System	Wavelength	PS/PI	State	Structure	Ref.
Hydrogen Peroxide (H$_2$O$_2$)	Type I	(UV) 254 nm	PI	Liquid		[72]
Iron Pentacarbonyl Fe(CO)$_5$	Type I	(UVC) 254 nm	PI	Liquid		[96]
2,2-dimethoxy-2-phenyl-acetophenone	Type I	(UVC) 254 nm	PI	Liquid		[109], [110]
Acetophenone	Type I	(UV) 220-340 nm	PI	Liquid		[111]
Benzophenone	Type I	(UV) 220-380 nm	PI	Liquid		[112], [113], [114], [113]
4,4'-Bis(diethylamino)benzophenone	Type II	(UV) 220-400 nm	PI	Liquid		[115]
Benzoin ethyl ether	Type I	(UV) 220-370 nm	PI	Liquid		[116]
Benzoin	Type I	(UV) 220-360 nm	PI	sublimed		[117]

Benzoin with two methyl thioether substituents (MTB)	Type I	(UV) 313 nm	PI	Liquid		[117]
hydroxycyclohexyl phenyl ketone (HCPK)	Type II	(UVC) 254	PI	Liquid		[118]
Hexyl Acrylate (HA)	Type I	(UVC) 254	PI	Liquid		[119]

2.8.4 Effect of Heteroatom (Functional Groups)

Since most of the photoinitiators are liquid and even liquid monomers can be used in the PICVD in either evaporated or atomized form, we have briefly discussed the effect of heteroatoms on photochemical reactions. It is believed that hydrogen abstraction happens more easily in the case of carbons attached to a heteroatom (mainly nitrogen, oxygen, and sulfur) compared to the ones not attached to the heteroatoms. This definitely influences the course of polymerization [97]. The effects of the main heteroatom groups on polymerization are briefly discussed below.

Amines are one of the most common groups used as co-initiators in polymerization [120]. They are compatible with bioapplications and increase the hydrophilicity of coatings [73]. They can also have a contradictive effect on polymerization regarding the reaction atmosphere. Under air atmosphere, they can easily undergo H-atom abstraction to make a peroxy radical, which is very reactive (Equation 1) [120]. In turn, this radical can then abstract an H atom from the oxidizable monomer to make an amine hydroperoxy (propagation step, Equation 2). Consequently, amines can accelerate polymerization under air [120].

$RRNC^{\bullet}H + O_2 \rightarrow RRNCHOO^{\bullet}$ Equation 1

$RRNCHOO^{\bullet} + RRNCH_2 \rightarrow RRNCH^{\bullet} + RRNCHOOH$ Equation 2

The corrosion of substrates and yellowish color of final coatings are the biggest disadvantages of this functional group. Under inert atmosphere, they have a negative effect on polymerization leading to a retarding on polymerization due to the re-initiation reactions indicated in Equations 3 and 4 [121].

$$RRNCH_2 + M^{\bullet}H \rightarrow RRNC^{\bullet}H + MH_2 \qquad\qquad\qquad \text{Equation 3}$$

$$RRNC^{\bullet}H + MH_2 \rightarrow M^{\bullet}H + RRNCH_2 \qquad\qquad\qquad \text{Equation 4}$$
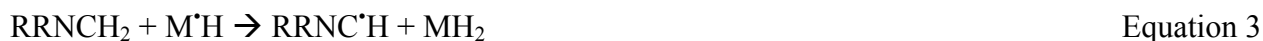
Sulfide groups have several positive impacts on the photopolymerization rates and resulting coatings. They are well known as thermal stabilizers and can therefore increase the thermal resistance of the resulting coatings [122]. These groups change the surface properties of coatings to be hydrophobic and improve the refraction index [123]. Aliphatic sulfides can be used as H-atom donors and serve as co-initiators of benzophenone [124].

Ether-containing monomers are another example that can prove the impact of heteroatoms on polymerization. These functional groups can increase the polymerization rate in air significantly. Some of these monomers, such as poly(ethyleneoxides) and poly(propyleneoxides), reduce the polymerization sensitivity of oxygen inhibition [97]. Ether-containing monomers can be also used as a co-initiator, although their initiation ability is less significant compared to amine-containing monomers [97].

2.8.5 Effect of Oxygen on photochemical reactions

Oxygen is a great radical scavenger because of its electronegative structure. Additionally, oxygen molecules absorb UV radiation. In the former, generated radicals are consumed and in the later radical formation is suppressed. Together, they inhibit and delay the PICVD process. Several studies have investigated how to understand the effect of oxygen on photo polymerization reactions. The results show several deleterious effects on free radical polymerization, which can be classified into 5 groups: 1- slow polymerization rate, 2- long term induction periods, 3- lower conversion, 4- a short polymeric chain and 5- pale surface properties [125, 126]. The presence of molecular oxygen in the reactor causes a negative impact on the efficiency of polymerization or chain reactions through the quenching of radicals. Molecular oxygen can rapidly react with the radicals ($R^{\bullet}$) to make a peroxyl radical. Peroxyl radicals are able to easily abstract a hydrogen atom from monomers to make a hydroxyperoxide (ROOH), which is less efficient in the

oxidation of double bonds or any other desired ones [97]. Figure 13 depicts the mechanism in detail. This phenomenon has negatively impacted the quantum yield of the initiation step and is called oxygen inhibition. Oxygen inhibition is more common in the photo-curing of coatings with a high ratio of surface to volume providing optimal conditions for the diffusion of oxygen [97].

$$R^{\cdot} + O_2 \rightarrow ROO^{\cdot} \hspace{8cm} \text{Equation 5}$$

$$ROO^{\cdot} + RH \rightarrow ROOH + R^{\cdot} \hspace{6cm} \text{Equation 6}$$

Where RH, $R^{\cdot}$ are a hydrogen donor (or a monomer) and a free radical made of an initiator, respectively.

A polymerization reaction can take place when the oxygen is depleted from the polymerization media by injecting an inert gas, such as nitrogen, or the consumption rate of oxygen in the media is greater than its diffusion rate into the media. [125-127]. Oxygen inhibition can be prevented by using a physical method as well.
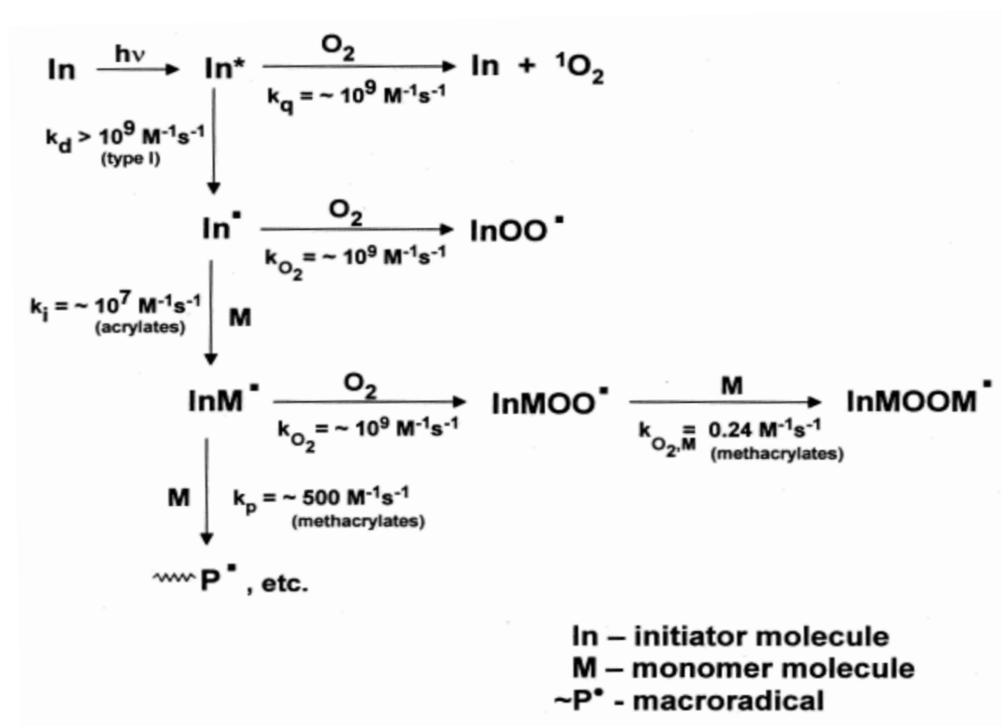
Figure 13.Mechanism of oxygen effect on polymerization [97].

2.8.6 Effect of Temperature

The effect of temperature on photochemical polymerization is well understood and has been

mentioned by several authors [97, 128, 129]. Temperature has a two-stage behavior on the photopolymerization rate and total conversion. The first stage happens when the temperature range is 70-90 ºC, which leads to an increase in the polymerization rate due to the Arrhenius behavior. The second stage (>90 ºC) can lead to either a decrease or a plateau in the polymerization rate. As mentioned before, polymerization is a radical chain reaction comprised of initiation, propagation, and termination (in the presence of oxygen, we can also have the inhibition step). At low temperature (70-90 ºC), propagation is conducted while termination rates become dominate at higher temperatures (>90 ºC). This is mentioned as the best reason for the two-step behavior of temperature. In the case of liquid photopolymerizations, temperature has a significant impact on the viscosity of monomers and the viscosity has an impact on the maximum propagation rate. Therefore, as the reaction temperature increases, the monomer viscosity rapidly drops and the maximum propagation rate consequently increases [97].

2.8.7 Crosslinking Systems

Figure 14 depicts reactions, which lead to the formation of a crosslinking network. Accordingly, the addition of monomer molecules into the polymer chains containing pendant bonds is the first stage of network formation. Continuing on, three pathways can be considered to form the network namely, pathway A in which the addition of more monomer molecules is desired, pathway B (interamolecular crosslinking) in which cyclization reactions are considered to determine network formation and pathway C (intermolecular crosslinking) in which a radical site is added onto the free double bond. Pathway C leads to network formation [125]. The apparent reactivity of pendant double bonds on the same chain is enhanced, which leads to higher cyclization and consequently the formation of compact structures (microgel). In this case, the reactivity of pendant double bonds decreases due to trapping and further reactions occur through chemical joining. The formation of compact structures or microgels is the reason for network inhomogeneity, which causes lower mechanical strength in the polymeric network. Based on the network formation strategy, polymer radicals can be classified into three populations: free radicals, attached radicals to loosely crosslinked portions, which are relatively mobile, and trapped radicals, which are an important feature of the network formation [125].

~•   **radical end**

⌒ ⌒   **divinyl monomer**
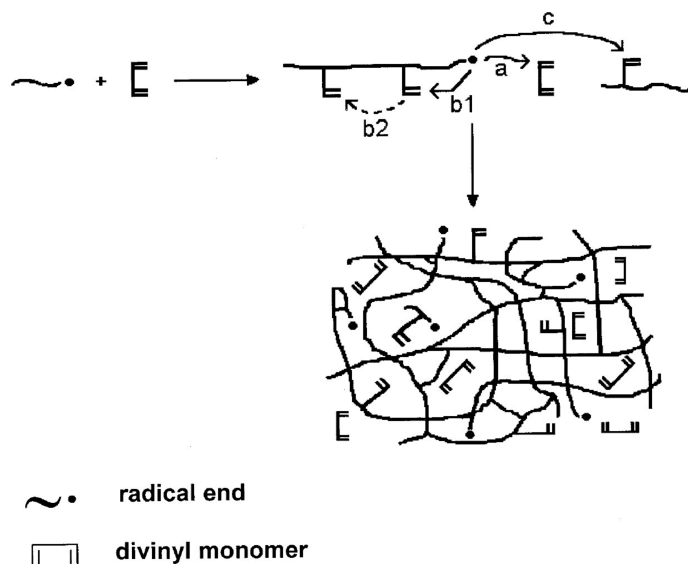
Figure 14. Croosslinking Network formation [125].

2.8.8 Polymerization Time

The thickness of coatings can be controlled by the treatment time. Scherzer (2012) investigated the effect of exposure time on the photopolymerization of silicone acrylates. Three different exposure times were chosen namely 20, 50, and 100 ms under VUV exposure. The results showed that by increasing exposure time, the conversion of double bonds increased [98]. Generally, it can be mentioned that longer polymerization times lead to thicker caotings [95, 130]. As an example, Farhanian et al. (2018) indicated that the coating thickness resulted from syngas/PICVD system (in the presence of H_2O_2) on the silicon wafers increases linearly over time (Y=0.7t) [95].

2.8.9 Surface Analysis Techniques of Coatings

Characterization of engineered surfaces and coatings can be analyzed by many physical and chemical methods. Some of the most common and favorable chemical analysis methods are X-ray photoelectron microscopy (XPS), Fourier – Transform Infrared Spectroscopy (FT-IR), ThermoGravimetric Analysis (TGA), and Time-of-Flight Secondary Ion Mass Spectrometry (ToF-SIMS). Tensiometry or Contact –Angle Measurements (CA) and Transmission Electron

Microscopy (TEM) are common physical techniques to characterize the surface properties of coated samples.

2.8.9.1 XPS and Chemical Derivatization

XPS is a surface sensitive spectroscopic technique that became a very common and favorable approach in the chemical characterization of samples and coatings. This method works based on irradiating surfaces by X-ray beam and simultaneously monitoring kinetic energy and electron intensity in a surface penetration range of 0-10 nm. XPS is a qualitative method to study the chemistry of surfaces (in the survey XPS spectra) and to gain more information about chemical bonding states or coating structure in the high-resolution spectral mode. XPS can be used in a quantified way for favorable functional groups if well-established chemical derivatization reactions (Chemical Derivatization X-ray Photoelectron Spectroscopy or CD-XPS) are combined with this technique. In the case of quantification of hydroxyl groups, reagent of trifluoroacetic anhydride (TFAA) is commonly applied and in the case of quantification of amine groups, reagent of 4-trifluoromethyl benzaldehyde (TFBA) is commonly applied. Derivatization reactions take place in a small chamber (typically ca. 25 mL) under vacuum. The mentioned reagents are very selective to the specific functional groups. After evacuation (deaeration) of the chamber using nitrogen, the chamber is connected to the reservoir containing the desired reagent (the reagents is in the form of liquid and should be used individually). Over time, the chamber becomes saturated by the vapor pressure of the reagent to label the desired functional groups. The appropriate time to complete the derivatization reactions for the reagents of TFAA and TFBA was previously suggested to be 60 and 240 min, respectively. Then, the reservoir containing the reagent becomes separated from the chamber and the chamber is evacuated for a short period of time. Surveying XPS analysis on both the derivatized and non-derivatized samples can reveal the quantitative measurements of functional group concentrations using the equations 7 -10 (in the case of TFAA and TFBA) [94].

XPS can be used to characterize both CNTs and CNT buckypapers before being applied in the biological experiments. CD-XPS can also be used to count the number of functional groups, which is an effective parameter in biological assays [21].

$$[NH_2]_N = \frac{I_{F1s,D}/3.RSF_{F1s}}{I_{N1s,D}/RSF_{N1s}} \qquad \text{Equation 7}$$

$$[OH]_O = \frac{I_{F1s,D}/RSF_{F1s}}{3.I_{O1s,D}/RSF_{O1s} - I_{F1s,D}/RSF_{F1s}}$$

Equation 8

$$[NH_2]_T = \frac{I_{F1s,D}/3.RSF_{F1s}}{I_{C1s,ND}/RSF_{C1s} + I_{N1s,ND}/RSF_{N1s} + I_{O1s,ND}/RSF_{O1s}} * \frac{I_{N1s,ND}}{I_{N1s,D}}$$

Equation 9

$$[OH]_T = \frac{I_{F1s,D}/3.RSF_{F1s}}{I_{C1s,ND}/RSF_{C1s} + I_{N1s,ND}/RSF_{N1s} + I_{O1s,ND}/RSF_{O1s}} * \frac{I_{O1s,ND}/RSF_{O1s}}{I_{O1s,D}/RSF_{O1s} - I_{F1s,D}/3.RSF_{F1s}}$$

Equation 10

2.8.9.2 FT-IR

FT-IR is an accessible technique that can be used for surface analyses. This technique works based on the light absorption of elements in a wide range of wavelengths at the same time, which decreases the measuring time and increases light throughput or performance. An FT-IR spectrometer comprises five pieces, namely a beam splitter, fixed mirror, a movable mirror, spectrum detector, and Michelson interferometer with a light source. This method is called Fourier transform because the Fourier mathematical method is applied to convert the spectrum data into Fourier spectrum. Based on Equation 11, the continuous data, such as frequency (v) and scan length (X), is converted into discrete data. The continuous data FT-IRs should have a strong detector and provide a high signal-to-noise ratio spectrum for an appropriate measurement.

$$S(n.\Delta v) = \sum_{n=0}^{N-1} I(n.\Delta X) e^{i2\Pi n.k/N}$$

Equation 11

2.8.9.3 TGA

TGA is a useful technique mostly for the bulk characterization of samples. However, this technique can be easily used to characterize and quantify coatings. TGA works based on the weight loss of substances as a function of temperature or time at a controlled temperature and atmosphere. TGA can be easily merged with other techniques to give more valuable information about the samples, such as TGA/MS, TGA/DSC, TGA/IR, etc. Derivative TGA is another feature of this technique in which a derivative of weight loss is plotted. DTGA curve shows weight loss assigned to a substance. The weighing accuracy and isothermal temperature accuracy of this method are reported to be 0.1% and 1ºC, respectively. Table 5 presents the degradation

temperature of CNTs and their common impurities. Accordingly, SWCNTs are degraded at a temperature range of 600-650 ºC depending on the structural integrity of SWCNTs [131, 132]. When SWCNTs are oxidized, their degradation temperature happens more easily and at a lower temperature. According to the extent of oxidation, the oxidized SWCNTs can be degraded at a temperature range of 400-600 ºC [131]. Since SWCNTs have a lot of carbon impurities, such as amorphous carbon, the impurities can be quantified based on their lower degradation temperature as SWCNTs or oxidized SWCNTs (200-400 ºC) using TGA. The metallic particle impurities are normally stable at a temperature of less than 800 ºC. Therefore, the mass residue after reaching the temperature of 800 ºC is assigned to metallic impurities and their oxidized complexes [131]. The humidity gained by the SWCNT samples can also be quantified based on the weight loss at a temperature of less than 100 ºC [133]. This analysis method can also be used to measure functional groups and more promising to measure impurities of CNTs before being applied in the biological assays. This method is commonly used to identify types of impurities of CNTs [10].

Table 5. Degradation temperature of SWCNTs and their common impurities.

Components	Degradation Temperature (ºC)	Ref.
SWCNTs	600-650	[131, 132]
Oxidized SWCNTs	400-600	[131]
Amorphous Carbon	200-400	[131, 132]
Metallic Residues	>800	[131]
Humidity	<100	[133]

2.8.9.4 ToF-SIMS

ToF-SIMS is a surface sensitive spectroscopic method in which the sample surface is bombarded by a pulsed ion beam (mostly Cs or Ga) to remove molecules from the surface. The depth penetration of the ion beam in this technique is less than 1 nm. Secondary ions made by the collision of the primary ion beam and surface were then accelerated in a long flight tube and their mass was determined based on the time it took the secondary ions to reach the detector. The high surface sensitivity of this technique should be mentioned as the main drawback of the method as

it can be easily affected by topographic effects and probable surface contaminations. This method can be used in three different ways, namely surface spectroscopy, depth profiling, and surface imaging [134].

2.8.9.5 CA Measurements

Tensiometry or contact angle measurement is a physical surface analysis technique with a penetration depth of 0.5 nm. This method can be used to analyze surface wettability and surface energy. This method works based on the measurement of the angle between a drop of liquid (usually water) and a solid surface (Figure 15A). Wettability of surfaces is categorized into 4 groups, namely superhydrophilic (<5°, the drop easily spreads on the surface), hydrophobic (>90°, Figure 15B), hydrophilic (<90°, Figure 15C), and superhydrophobic (>150°, the drop tends to minimize the angle, Figure 15D). The surface energy of treated/untreated samples can take place based on the Young-Laplace Equation (Equation 12) [135].

$$\gamma_{SV} - \gamma_{SL} = \gamma_{LV} \cos \Theta \qquad \text{Equation 12}$$

where γ_{LV}, γ_{SV}, and γ_{SL} are the surface tension of liquid/vapor, solid/vapor, and solid/liquid, respectively. Θ is the contact angle between the drop and solid [135].
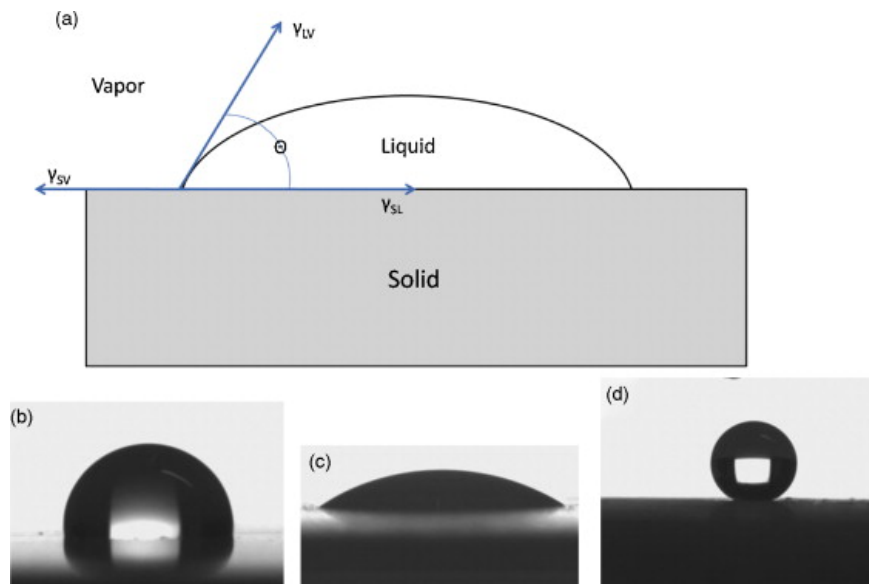
Figure 15. (a) The contact angle between a drop and surface in exposed to air, (b) hydrophobic surface, (c) hydrophilic surface, superhydrophobic surface [135].

There is another interesting value, adhesion work (W_a), extracted from the Dupré equation (equation 13). This value is needed to separate the equilibrium phase of two phases from the interface.

$$W_a = \gamma_L + \gamma_s - \gamma_{SL}$$
Equation 13

Dynamic CA is an alternative method to measure the angle between the droplet and the surface under moving boundaries including air, liquid droplet, and solid film (Figure 16). Dynamic tensiometry can be conducted in three different ways, including advancing CA (θ_A), receding CA (θ_R), and CA hysteresis. Advancing CA is about the wetting ability of liquid and receding CA is about its detaching ability from the surface. Hysteresis CA describes the difference between advancing and receding CAs. Dynamic CA is able to reveal the inhomogeneity and roughness of the surface rather than the wettability of surfaces [136-138]. This technique (Tensiometry) has been extensively used to evaluate surface wettability and surface energy of CNTs [139-141]. For example, the dynamic contact angle is used to evaluate the stability and wettability of treated aligned CNT [139]. As another example, Li et al. (2016) used this technique to measure the surface energy of treated CNTs [140]. This technique seems to be easy and reliable enough to evaluate nanoparticle wettability. However, the measurements are conducted on the buckypaper form rather than on individual particles, which can be pointed out as the major disadvantage for this method [141].
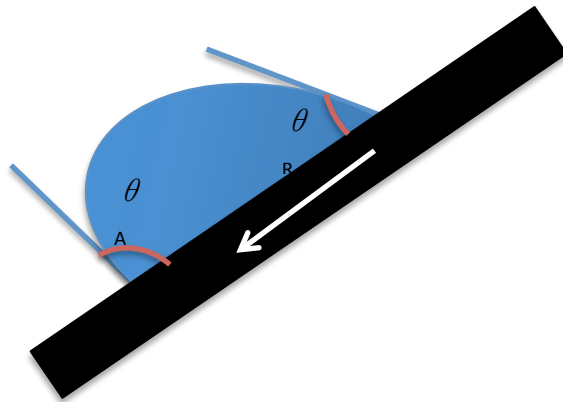
Figure 16. Dynamuc contact angle A) advancing CA, B) receding CA.

Since wettability and surface energy of CNT are reported as effective parameters on cytotoxicity of CNTs, this technique has been commonly used to measure their wettability and surface energy before being utilized in cytotoxicity of SWCNTs [43].

2.8.9.6 Scanning Electron Microscopy (SEM) and TEM

 SEM is an electron microscope in which the images are made by the interaction of beam electrons and sample atoms. This method can provide valuable information about surface morphology and the chemical composition of samples. SEM has been extensively used in the field of surface engineering during the past decades. This method is able to measure the length of CNTs and the diameter of CNT bundles. This method is not precise enough to measure the diameter of individual CNTs [142]. To measure the diameter of an individual CNT, TEM can be an impressive option. In addition, the morphology and structure of coatings and substances can be easily investigated by TEM. TEM is a powerful tool that provides atomic resolution images of the samples. This method can be easily used for in situ characterizations of structural changes of nanocrystals caused by any electrical field/anealing or mechanical stress (characterization of SWCNTs when they are affected by an electrical field or mechanical stress in situ). A modern TEM is also equipped with a chemical analysis system called energy-dispersive X-ray spectroscopy (EDS) or electron energy loss spectroscopy (EELS). These features make it possible for TEM analysis to reveal the chemical properties of materials (for example a single crystal) and even full structural properties of a single particle with a focused electron probe [143]. EDS works based on the emitted X-ray from the illuminated specimen region as a function of photon energy while EELS works based on the intensity of transmitted electrons as a function of energy loss. These techniques provide TEM ways to reveal information about the electronic structure of samples [143]. TEM and SEM can be used to provide some valuable information about CNTs before being used in the biological assays.

2.8.9.7 Other Methods

The excited state processes of photoinitiators can be directly investigated through transient absorption laser spectroscopy [144]. This method is able to provide valuable information about the lifetimes of excited states, rate constants of interaction and transient absorption spectra. The picosecond time scale of this spectroscopy enables ultrafast processes, especially the excited state

of photoinitiators. Chemically-induced dynamic nuclear polarization-Nuclear magnetic resonance (CIDNP-NMR) and (CIDEP-ESR) are other methods that have been used in this area to investigate the excited state of photoinitiators and monomers. Allonas et al. (2000) used time resolved thermal lens spectroscopy for the investigation of the excited state of photoinitiators in which the analysis was done based on heat monitoring originating from transient states [145]. Time resolved photoconductivity is another technique in line with this goal in which radical ion generation can be directly monitored and provide worthwhile information [144].

2.9 Summary of the Literature Review

During the literature review, we presented CNTs, their types, and their individual properties. We got familiar with their synthesis methods and their common impurities as well as the purification methods to get rid of them. We highlighted the (potential) applications of CNTs in various industries and focused deeply on the biological applications. It is indicated that the hydrophobicity of CNTs limits their applications despite their individual properties. In the literature review, we seriously focused on the biological application of SWCNTs, such as scaffolds in bone fractures, and found a lot of contradictions about their cytotoxicity, which is referred to as a variety of effective parameters, such as their aspect ratio, impurities, the extent of oxidation, the density of functional groups, surface energy, and hydrophobicity. We could not find a single article in which the cytotoxicity of SWCNTs was studied in terms of a full range of surface wettability of CNTs with similar precursors. Therefore, we noticed that SWCNTs have not been treated in a full range of wettability ranging from superhydrophilic to superhydrophobic, which is in high demand in nanocomposite and biological applications. Therefore, we reviewed the functionalization methods of CNTs, including wet and dry methods. There was some evidence about the ability of syngas/PICVD in making both superhydrophilic and superhydrophobic surfaces with the same precursors based on the flat metallic substrates. However, this method has not been applied to treat CNTs. Then, we reviewed the effective parameters on the PICVD method and deeply focused on the syngas/PICVD. The literature showed that there is not a lot of information about the syngas/PICVD. The kinetics and mechanism of syngas/PICVD have not been investigated through the gas phase analyses, which would be a big gap in this area of knowledge. We finally introduced some characterization methods applying the surface analyses of nanoparticles.

CHAPTER 3   OBJECTIVES AND ORGANIZATION OF THE ARTICLES

Despite all the distinctive properties of CNTs, their hydrophobicity creates a big challenge for them to be dispersed in polar liquids, which restricts their commercial use in many applications. SWCNTs have demonstrated their potential in therapeutic and biomaterial applications, but their cytotoxicity prevents them from being used in human body. However, some researchers relate CNT cytotoxicity to their hydrophobicity resulting in their agglomeration. Based on the literature review presented in chapter 2, we identified PICVD as the best option for CNT functionalization in the hopes of addressing this issue. Specifically, this method can use inexpensive and available precursors (for example, CO and H_2). This project aims to answer the research hypothesis: syngas/PICVD could potentially apply various densities of functionalities and consequently wettability on SWCNTs by controlling the operational parameters.

3.1 Objectives

3.1.1 General Objective

The main objective of this research was defined as "UNDERSTANDING AND APPLYING PHOTO-INITIATED CHEMICAL VAPOR DEPOSITION TO MODIFY THE SURFACE PROPERTIES OF SINGLE-WALLED CARBON NANOTUBES".

3.1.2 Specific Objectives

To attain the main objective we defined two specific objectives:

(1) Study the effect of PICVD operational parameters on the treatment of SWCNTs, focusing on two key precursor types (syngas and ozone)

(2) Advance our knowledge of the kinetics and transport phenomena in syngas/PICVD applied to the treatment of SWCNTs

3.2 Organization of the Articles

The specific objectives resulted in the following two chapters containing the related articles:

The first article presented in Chapter 4 is entitled "*Inducing a full range of wettability through the surface modification of single-wall carbon nanotubes by photo-initiated chemical vapor deposition using syngas*". We investigated the versatility of syngas/PICVD to make various ranges of surface wettability through effective parameters in PICVD. The effective parameters included the flow rate of precursors, the molar ratio of CO/H_2, pressure, the position of the sample inside the reactor, and treatment time. This article was published in the *Chemical Engineering Journal* (Volume 325, (2017), pages 101-113).

The second article presented in Chapter 5 is entitled "*Reaction kinetics and temperature effects in syngas photo-initiated chemical vapor deposition on single-walled carbon nanotubes*". In this work, we present a kinetic study of syngas/PICVD. We compared syngas/TACVD and syngas/PICVD and investigated the role of temperature as the most important thermodynamic parameter in both cases. The significant role of $Fe(CO)_5$ as a photoactive contaminant in CO cylinders is investigated following both gas- and surface-phase analysis, and a mass balance was experimentally calculated and suggested for syngas/PICVD. By coupling gas- and surface-phase analysis in addition to previous work, we presented two separated reaction schemes for the gas- and surface-phase reactions. We could also present a general molar-based formula of $C_{38}H_5O_{43}Fe_{14}$ for the bulk of the coating deposited on the surface, which was different from the surface structure with the chemical formula $C_{21}O_{60}Fe_{19}$ (based on the atomic percentage). This study suggests that little to no CO and H_2 is consumed in the reactor, and that processing can be optimized to decrease syngas throughput. This study was published in the *Journal of Nanoparticle Research* (Volume 21, 2019).

CHAPTER 4   ARTICLE 1: FULL RANGE OF WETTABILITY THROUGH SURFACE MODIFICATION OF SINGLE-WALL CARBON NANOTUBES BY PHOTO-INITIATED CHEMICAL VAPOR DEPOSITION

Seyedehsan Hosseininasab [a], Nathalie Faucheux [b], Gervais Soucy [b] and Jason R. Tavares1,[*]

[a] Department of Chemical Engineering, Polytechnique Montreal, Montreal, Québec H3T 1J4, Canada

[b] Department of Chemical and Biotechnological Engineering, Université de Sherbrooke, Sherbrooke, Québec J1K 2R1 Canada

Published in:

ABSTRACT

Single-wall carbon nanotubes (SWCNTs) have various remarkable properties, which make them a promising candidate for many applications. However, their inherent hydrophobicity have limited their commercial use in optical, biological, and electrical applications. Photo-initiated chemical vapor deposition (PICVD) using syngas is proposed as a novel, affordable, and versatile method to tailor SWCNT wettability through the addition of oxygen-containing functional groups. Following PICVD surface treatment, X-ray photoelectron spectroscopy, water contact angle measurements (CA), thermogravimetric analysis, Raman spectroscopy and transmission electron microscopy confirm controlled oxygenation of the SWCNT surface. Indeed, this novel approach allows to reproducibly make SWCNT having surfaces properties ranging from superhydrophilic (CA<5°) to superhydrophobic (CA>150°), including any intermediate values, by simply varying operational parameters such as molar ratio of the syngas precursor, photo-polymerization time and reactor pressure (about normal conditions).

4.1 Introduction

Single wall carbon nanotubes (SWCNTs) have various properties of interest, such as high mechanical and electrical conductivity, remarkable thermal stability (up to 2800 °C under vacuum) [19, 146], proportionally lower weight than steel and titanium (typical materials in bone applications) [147, 148] and the highest Young's modulus among all different types of composites and nano-materials (> 1-5 TPa) [19, 148]. These individual properties make them promising candidates for a wide range of applications such as aerospace, nanocomposites, biomedical and tissue engineering, to name only a few [149-151]. These materials have also shown potential to be used in bone applications due to their similarities with triple helix collagen fibrils, in terms of size and shape (diameter of SWCNTs ranges between 0.7-1.5 nm) [152-154]. Not only can these materials enhance the mechanical properties of biomaterials [155], they can also stimulate bone regeneration [156]. Therefore, they may be effective for use in different bone substitutes, such as scaffolds and fillers.

Despite all the above-mentioned properties and potential of SWCNTs for different applications such as reinforcements in polymer nanocomposites and biomaterials synthesis, their inherent hydrophobicity and insolubility are the most challenging features that need to be addressed [146].

For example, in the case of nanocomposites, one of the most important factors that should be considered is the homogeneous dispersion of SWCNT nanofillers [151]. Untreated SWCNTs tend to aggregate due to their high surface area to volume ratio and strong van der Waals interactions while the resulting aggregation negatively overshadows mechanical, electrical and thermal properties gained by SWCNT addition [151, 157-159].

Various approaches exist to modify the CNT's surface properties and address such surface-based problems, including surfactants, oxidation, sonication and functionalization [19]. Of these, surface functionalization has been identified as a promising approach [19]. Functionalization implies the covalent grafting of a specific chemical functional group to the surface. Intuitively, the addition of oxygen-based functional groups would seem like a viable route to decrease hydrophobicity and, possibly, make them more compatible to be used in nanocomposites [151] and bio-applications [152].

Covalent functionalization, in which functional groups (such as amino and carboxylic acid groups) are grafted onto SWCNT walls, help overcome attractive forces can prevent this agglomeration and lead to better dispersion [151, 157]. Moreover, the higher reactivity of treated SWCNTs, as well as their increased interfacial bonding and load transfer with the surrounding polymer resulting from reactive functional groups (oxygen- or nitrogen-containing groups) after treatment leads to an increase in mechanical and electrical properties of nanocomposites [151]. Given the wide range of polymer materials (hydrophobic and hydrophilic) and subsequent filler-matrix interactions, a technique capable of tailoring SWCNT wettability is required.

In the case of biomedical applications, there are significant contradictions in the literature concerning the effect of such SWCNT functionalization on their cytotoxicity [160]. For example, some indicate that functionalization of SWCNTs using carboxylic acid groups reduces cell viability and proliferation [58-60], whereas Montes-Fonseca et al. (2012) reported less cytotoxicity for functionalized CNTs [61]. A deep examination of the literature reveals that the contradiction comes from different CNT properties (i.e. wettability, functional group charging, variation of SWCNT size, degree of purity and effect of surface energy, etc.) [22]. Furthermore, the contradictions regarding cell response to functionalized SWCNTs in the literature can likely be attributed to the fact that individual reports do not study surface treatments over wide ranges (i.e. no attention typically paid to the extent of functionalization) – essentially, a single treatment

is applied and the cytotoxicity is analyzed [11, 12]. Beyond the issue of cytotoxicity, applications such as the selective binding of specific blood proteins (that can have polar and non-polar components) to CNTs can necessitate hydrophobic or hydrophilic surfaces [161, 162]. Therefore, before any practical biomaterial applications of CNTs can be considered, it is necessary to address the issue of surface wettability. Specifically, there is a need to study a surface modification technique capable of controlling the extent of the functionalization. Such a method should allow a "full range" of properties (from superhydrophilic to superhydrophobic, for example) using a similar reaction scheme and functional groups.

Functionalization techniques can be classified into two groups: solvent-based (wet chemistry) and solvent-free (gas-phase) methods. Solvent-based approaches suffer from multi-step and complex preparation methodologies and can damage the CNT structure. Furthermore, separation of the treated nanomaterials from the solvent, as well as the management of solvent waste, can be a time-consuming and significant processing issue, which is generally dodged in the literature [3, 99, 100, 163, 164]. Gas-phase surface modification techniques can be classified according to the energy source applied for reaction initiation, including thermally activated chemical vapor deposition (TACVD) [101], plasma-enhanced CVD (PECVD) [165] and photo-initiated CVD (PICVD) [99]. Table 6 presents a detailed comparison between the current functionalization methods for CNTs.

Unlike TACVD (which uses heat, problematic for temperature-sensitive substrates) and PECVD (which requires specialized and costly plasma conditions), PICVD uses light to initiate organic deposition reactions. In this process, radicals can be generated by exposure to ultraviolet (UV) light, launching a series of heterogeneous reactions on the surface of a substrate in parallel with gas phase reactions. PICVD has been gaining interest for the surface treatment of nanomaterials because of its simple procedure, low cost, possibility of operation at or near atmospheric pressure (depending on the wavelength selected) [99, 165], higher intermolecular cross-linking [86], low energy consumption [99, 165] and, most importantly, ability to adjust the desired degree of functionalization [86].

A key parameter for PICVD is the selection of an appropriate monomer to impart the desired functional groups and surface properties (hydrophilic or hydrophobic). The selected monomer should therefore contain the desired chemical moieties, as well as contain groups capable of

forming radicals following exposure to light at the selected wavelength. Ozone is a UV sensitive molecule that can be used as a precursor for oxidative attacks on SWCNTs [166]. It absorbs light significantly at 253.7 nm (peak emission in Hg discharge lamps), with an efficient quantum yield [166]. Accordingly, it can be a good precursor to treat SWCNTs under PICVD, given that Hg discharge lamps are commercially available at low cost (in the form of germicidal lamps) and light at 253.7 nm (UVC) is readily transmitted through common materials such as quartz.

Beyond oxidative attacks with ozone (which are limited to imparting hydrophilic functionalities on CNTs), it is possible to form organic coatings with UVC light, namely by using syngas as a precursor [99]. Our research team has previously demonstrated that syngas (CO and H_2) could be used in PICVD to form hydrophilic and hydrophobic surfaces on copper substrates by manipulating treatment pressure (near atmospheric) and CO/H_2 ratio [99]. In this process, radicals produced from the dissociation of a photo-initiator (PI) and the precursor mixture lead to a combination of gas phase and surface reactions to impart surface functionality [101, 165].

Surface wettability can be investigated through contact angle (CA) measurements, namely through two approaches: static and dynamic methods. Static (or "sessile drop") CA is a measure of the angle between a liquid droplet (of known polarity) and the surface of interest. This method has been applied extensively by CNT researchers - Woo et al. (2010) found that the static CA with water of CNT films oxidized at 400 °C for 30 min under air flow was 96.9° [167]. Koumoulos and Charitidis (2017) measured the static CA to assess the wettability of CNT arrays synthesized by CVD, finding values of. 136° and 150° for water and glycerol droplets, respectively [168]. Liu et al. (2017) surface treated CNT films by atmospheric pressure plasma using a mixture of helium and oxygen, leading to a static contact angle decrease from 105° to 80°, 64°, and 47° only after 0.1, 0.2, and 0.3 s treatments, respectively [169]. Indeed, oxygen plasma functionalization is a common method to make CNTs hydrophilic [170, 171] Similiarly, Wang et al (2009) measured the wettability of graphene and graphene oxide thin films, reporting surface energies of 46.7 and 62.1 mJ/m^2, respectively [172]. Alternatively, the dynamic CA assesses the angle between the liquid and the surface under moving boundaries (three phases: air, liquid and solid film). The dynamic CA is defined through three major parameters: advancing CA (θ_A), receding CA (θ_R), and CA hysteresis. θ_A indicates the wetting ability of a liquid on a solid film upon initial contact, whereas θ_R describes the difficulty of removing the liquid from the

surface. CA hysteresis is defined as the difference between the two (θ_A - θ_R). Dynamic CA serves as an indicator of surface quality in terms of inhomogeneity of chemical treatment, roughness, and stability [136-138]. For example, Lau et al (2003) employed dynamic CA to investigate the stability and wettability behavior of aligned CNT forests coated by poly(tetrafluoroethylene)(to make superhydrobic surfaces through a combination of chemical and roughness changes) [139]. Aside from CA approaches, an inverse gas chromatography-surface energy analyzer (IGC-SEA) may be used to assess expected wettability [173, 174]. For example, Li et al.(2016) measured surface energy of carbon fibres coated with carbon nanotubes. They could successfully fabricate CNT coated Carbon fibres by electrospray method resulted in a multi-scale hierarchal structure without any tensile strength changes of fibres [140]. Both CA and IGC-SEA approaches applied to CNT rely on measurements of the nanomaterials in a bucky paper configuration (or deposited/grown on a surface) – in other words, in aggregate form. To measure the wettability of individual CNTs, indirect measurements must be applied, typically with the CNT in a dispersed state – these can range from stability of CNT in suspension [103] to measurements of the zeta potential (with corrections applied for high-aspect ratio particles) [175].

To the best of our knowledge, the use of syngas and PICVD (syngas/PICVD) on SWCNTs has never been investigated, and shows potential as a viable method to systematically modify CNTs over a wide range of surface energy. Given the importance of process control and materials customization in the fields of chemical and materials engineering, we consider this exploration to be significant. Hence, the main goal of this study is the surface treatment of SWCNTs by syngas/PICVD to allow the addition of oxygen-containing functional groups and thus obtain different degrees of functionalization and, consequently, various surface energies. In this regard, syngas/PICVD is compared with an ozone/UV-based (ozone/UV) treatment.

Table 6. Comparison between some common functionalization methods of nanoparticles and carbon nanotubes.

Methods	Type	Advantages	Drawbacks	Ref.
Wet Chemistry	Covalent (liquid phase)	1- Easy scale-up 2- Facile control of the extent of hydrophilicity 3- Potentially low-cost method (depending on reagents)	1- Multi-step process 2- Unable to make and control extend of hydrophobicity 3- Time consuming 4- Solvent waste management 5- Destructive method for hexagonal structure of CNTs 6- Specific complex reagents for the functionalization	[3, 99, 100]
Surfactants	Non-covalent	1- Able to make both hydrophilic and hydrophobic surfaces (with different or amphiphilic molecules) 2- Non-destructive method for the hexagonal structure of CNTs 3- Preserves the mechanical and electrical properties of SWCNTs	1- Low stability due to weak binding forces 2- Extended sonication period required 3- Poor scale reliability	[176-178]
TACVD	Covalent (gas-phase)	1- Large scale treatment 2- Able to make and control extend of functionality 3- High deposition rates and conversions	1- Vacuum requirement 2- High temperature requirement 3- Lack of appropriate range of monomers 4- Expensive (processing and capital costs) 5- Poor energy efficiency 6- Destructive method for the hexagonal structure of CNTs 7- Difficult to make hydrophobic surfaces	[3, 101]
PECVD	Covalent (gas-phase)	1- Large scale treatment (atmospheric discharges) 2- Able to make and control extend of functionality 3- High deposition rates and conversion 4- Control on deposition temperature	1- Expensive (processing and capital costs, specialized operation) 2- Unreacted precursors and by-products, often embedded in functional coating 3- Low efficiency because of the energy wasted on low energy electrons 4- Unstructured coatings with low cross-linking 5- Limited to small scales for low-pressure discharges	[71, 77, 101-103]
PICVD (Ozone/UV)	Covalent (gas-phase)	1- Large scale treatment 2- Low cost 3- Highly cross-linked coating 4- No vacuum/high pressure requirements 5- Room temperature process 6- High quality films due to low excitation energy	1- Unable to create hydrophobic coatings 2- Limited control on extent of hydrophilicity 3- Low conversion and deposition rate 4- Destructive method for SWCNT structures	[85-87]
PICVD (Syngas/UV)	Covalent (gas-phase)	1- Potential for large scale treatment 2- Low cost processing (inexpensive monomers and PI) 3- Able to make both hydrophilic and hydrophobic surfaces (various extents) 4- Highly cross-linked coating 5- Low energy consumption 6- Selectivity; high control of the overall process (film properties) due to mono-energetic photons that limit reaction pathways 7- No vacuum/high pressure requirements 8- Room temperature process 9- High quality films due to low excitation energy 10- Increased stability compared to their low-pressure plasma counterparts	1- Low conversion and deposition rate	[3, 95, 99]

4.2   Materials and Methods

4.2.1   Materials

Pure SWCNTs (P-SWCNTs) grown by radio frequency induction thermal plasma were purchased from Raymor-NanoIntegris (96.5% w/w, Quebec, Canada). The main impurities remaining in the purchased P-SWCNTs are Fe, Ni, Y and amorphous carbon (as identified by XPS and TEM measurements). Hydrogen peroxide (H_2O_2, 50% (w/w)) and n-hexadecane ($\geq$99%, EMD-Millipore) were purchased from Fisher Scientific (Montreal, Quebec). Ozone was generated by an Ozone Solutions TS-40 ozone generator (20 g/h), with ambient air as the gas source. Syngas (CO and H_2, Air Liquide, chemically pure) and argon (Air Liquide, 99.9%), were used as the functionalization precursors and purging gas, respectively. Two 96 cm-long UVC germicidal lamps (Model T-97505-80, Cole-Parmer Inc) were used for all experimental treatments (main emission peak at 253.7 nm, irradiance of 0.01 W/cm^2 at 3.5 cm, measured with an ILT1700 Radiometer equipped with a SED240 detector from International Light Technologies).
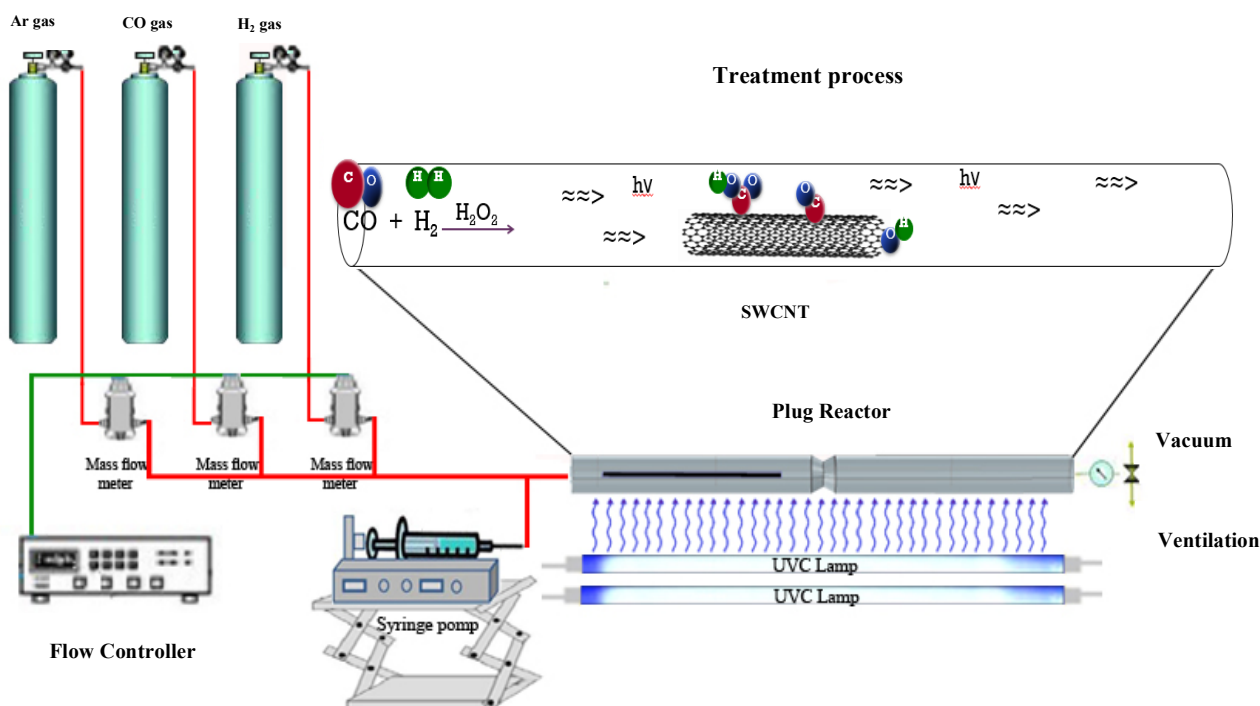
Figure 17. Schematic of the PICVD setup.

4.2.2 PICVD Setup

The PICVD reactor used consists of two UVC lamps and a 25-mm internal diameter quartz tube reactor (Figure 17). A syringe pump was used for H_2O_2 injection and Brooks mass flow controllers (series 5850E) were used to inject precursors (CO and H_2). A centralized vacuum system was applied when working at sub-atmospheric pressure (down to -20 kPa).

4.2.3 Surface Modification

To modify SWCNT surfaces, the method developed by Dorval Dion et al. (2014) was used [99]. Accordingly, P-SWCNTs (in the form of bucky paper) were placed inside the quartz reactor, which was then closed and sealed. Within the same reactor, SWCNTs were treated with one of two different precursors: ozone or syngas. In the case of ozone treatments, the reactor was purged for two minutes with argon at a rate of 3 L/min then connected to the ozone generator. Ozonated air (5-7% w/w ozone, 500 ml/min) was fed to the reactor under different conditions presented in Table 7. In Table 7, experimental treatments 2 to 6 are related to the SWCNTs treated by ozone/UV while experiments 7 to 27 are dedicated to investigating the effects of treatment time, pressure, position of samples inside the reactor and hydrogen peroxide injection. In the case of syngas/PICVD treatments, the reactor was also purged with argon, then CO and H_2 precursors (total flow rate of 350 ml/min) were introduced at various ratios and conditions, as per Table 7. H_2O_2 was injected simultaneously via the syringe pump as a radical photo-initiator (PI) at a rate of 1 μL/s, directly into the syngas stream. Each experimental treatment was repeated at least 3 times. Six independent variables, including precursor molar ratio (H_2/CO), pressure, treatment time, flow rate of precursors and use of PI and position of samples inside the reactor were studied. According to the desired surface functionality, the process can be operated under slight pressure (up to +15 kPa) or slight vacuum (down to -20 kPa). Hydrophilic surfaces are typically obtained under slight vacuum, using hydrogen peroxide, and near the reactor inlet (16 cm), while hydrophobic surfaces are achieved under pressure closer to the outlet (82 cm), based on previous work performed with copper [99]. During treatment, the surface temperature was monitored using an IR Infrared thermometer. Treatment started at room temperature (~25 °C). Upon activating the UVC lamps, the temperature increased to ~52 °C over the first 15 min, and remained constant until the end of treatment (temperature increase attributable to heat emission from the UVC lamps).

Table 7. Experimental treatment conditions with corresponding wettability (contact angle/surface energy).

Samples		Experimental Conditions						Characterization	
No.	Description	Ratio (H$_2$/CO)	H$_2$O$_2$	Time (min)	Pressure (kPa)	Location (cm)	Flow Rate (ml/min)	Average Contact Angle	Surface Energy (mN/m)
1	n/a	purified	-	-	-	-	500	79±2 °	31
2	ozone/UV	ozone	Yes	60	-20	14	500	< 5°	73
3	ozone/UV	ozone	No	30	-10	14	500	< 5°	73
4	ozone/UV	ozone	Yes	75	-10	82	500	< 5°	73
5	ozone/UV	ozone	Yes	60	+15	14	500	< 5°	73
6	ozone/UV	ozone	No	60	+15	82	500	< 5°	73
7	syngas/PICVD	0.12	Yes	180	-15	14	350	0±3 °	73
8	syngas/PICVD	0.12	No	120	+15	82	350	156±7 °	36
9	syngas/PICVD	0.12	Yes	60	-15	14	350	31±2 °	64
10	syngas/PICVD	0.12	Yes	90	-15	14	350	25±5 °	67
11	syngas/PICVD	0.12	Yes	120	-15	14	350	5±3 °	72
12	syngas/PICVD	0.12	Yes	180	-15	14	350	0±3 °	73
13	syngas/PICVD	0.6	Yes	60	-15	14	350	29±1 °	65
14	syngas/PICVD	1	Yes	60	-15	14	350	47±5 °	54
15	syngas/PICVD	2	Yes	60	-15	14	350	36±3 °	60
16	syngas/PICVD	3	Yes	60	-15	14	350	59±4 °	45
17	syngas/PICVD	0.16	Yes	60	-15	14	350	22±3 °	68
18	syngas/PICVD	0.16	Yes	60	-15	14	300	27±3°	65
19	syngas/PICVD	0.16	Yes	120	-15	14	350	4±7 °	73
20	syngas/PICVD	0.16	Yes	60	-15	14	400	49±2 °	52
21	syngas/PICVD	2	Yes	120	-15	14	350	15+3 °	70
22	syngas/PICVD	0.12	Yes	120	+15	82	350	127± 5°	29
23	syngas/PICVD	0.12	No	120	-15	82	350	93± 6°	26
24	syngas/PICVD	0.12	No	120	+15	14	350	58± 4°	44
25	syngas/PICVD	0.12	No	60	+15	82	350	141± 6°	33
26	syngas/PICVD	2	Yes	120	+15	82	350	135± 3°	31
27	syngas/PICVD	3	No	120	-15	82	350	115± 2°	27

4.2.4 Surface Characterization

X-ray photoelectron spectroscopy (XPS) was performed with a VG ESCALAB 3 MKII system using Mg Kα x-rays, with a pass energy of 100 eV and energy step size of 1 eV for survey scans. High-resolution (HR) spectra of treated SWCNT (T-SWCNT) buckypapers were obtained at a pass energy of 20 eV, in increments of 0.05 eV. Some of the XPS characterizations were also performed by Kratos Ultra DLD system with a pass energy of 160 eV and step size of 1 eV for

survey scans and a pass energy of 20 eV and step size of 0.05 eV for HR spectra, using Al Kα x-rays. Peak fitting was performed as described by Yang and Sacher [179], using the Wagner table for sensitivity factors. Background correction was based on the Shirley method, used within the Thermo Avantage (V4.12) software package. Chamber pressure was kept 5 x 10^{-9} torr.

Surface wetting was assessed through sessile drop contact angle (CA) measurements using a FDS OCA DataPhysics TBU 90E tensiometer. 2 μL droplets of water (as a polar liquid) or n-hexadecane (as a nonpolar liquid) were deposited on 3 different areas of the samples, 3 successive times, in order to obtain the average CA. The exposure time between the droplet and the surface was considered 3 s for all experimental treatments. The surface energy was obtained by applying the Owens-Wendt method (Equation 14) to CA measurements (θ_w) with the two different liquids (water/polar and n-hexadecane/nonpolar) [180]. The total free surface energy (γ_s) was obtained by gathering the polar (γ_s^p) and dispersive (γ_s^d) components based on Equation 15. Table A1 in supplementary results presents the related information of the liquids.

$$\gamma_{sl}(1 + cos\theta_w)/2 = \left(\gamma_s^d\gamma_l^d\right)^{0.5} + \left(\gamma_s^p\gamma_l^p\right)^{0.5}$$

Equation 14

$$\gamma_s = \gamma_s^p + \gamma_s^d$$

Equation 15

Where γ_{sl}, γ_l^d and γ_l^p are the solid-liquid interfacial energy, the total dispersive component and the polar component of liquid surface tension, respectively.

Transmission electron microscopy (TEM, JEOL model JEM2100F) was used to investigate the effect of treatment on SWCNT morphology. The TEM grids used were coated with a lacey carbon film (D20045 grids with formwar substrates, Ni mesh 400, SOQUELEC International). To collect samples, T-SWCNTs were dispersed in methanol at a concentration of 1 mg/mL; TEM grids were then briefly dipped in this suspension (~ 1 s) and analyzed after drying.

The integrity of SWCNT samples was assessed by Raman spectroscopy using a Renishaw Invia Reflex Raman microscope equipped with an argon laser (514 nm), scanning in the range of 300-3500 cm^{-1}. Peak deconvolution was completed through the Renishaw Wire 3.4 software. Gaussian and Lorentzian line shapes were employed for all G′ and D′ bands, respectively, as this combination provides appropriate fits for Raman bands, especially to identify disorder in SWCNTs [181].

Thermal stability was assessed through thermogravimetric analysis (TGA, Model Q500, TA instruments) under air atmosphere. The temperature range was 30-800 °C, with a heating rate of 10 ° C/min for all samples. All experimental treatments were carried out with a platinum TGA pan (4 to 5 mg).

4.3 Results and Discussion

4.3.1 Physical Characterizations

To analyse the efficiency of ozone/UV and syngas/PICVD treatments on SWCNTs, we have first determined the physical properties of the treated samples. Table 7 presents the experimental conditions, related water contact angle and surface energy results for ozone/UV and syngas/PICVD treatments. The average water CA of P-SWCNT samples was 79±2° (Figure 18A). For all SWCNTs treated by ozone/UV (Experimental treatments 2-6), the water CA was <5° (below the detection limit of the instrument), irrespective of treatment time, pressure or position (Figure 18B). This behavior is expected: ozone peak absorption overlaps with that of the UVC lamps used [182]. These results are consistent with those of Wang et al. (2010), where they showed that ozone/UV treatments of vertically aligned multi-walled carbon nanotubes for 5 min could lead to superhydrophilic surface behavior (reactor operating with 0.2 L/min flow of oxygen gas supply at 50 °C) [182]. Since the peak absorption cross section of ozone is found at 253.7 nm, treatments under UVC light (λ = 200 to 300 nm) cause it to break down into oxygen gas (O_2) and reactive O radicals. These can react with defects sites (or dangling bonds) on the P-SWCNT surface, leading to the formation of -COOH, OH, and CO groups [182]. While ozone/UV allow for the possibility of sidewall functionalization on SWCNTs, longer ozone/UV treatments can actually destroy the SWCNTs' hexagonal carbon structure [183, 184]. While these experiments and previous works show ozone/UV's ability to produce superhydrophilic SWCNT surfaces [182, 185], it highlights its inability to vary surface energy over a wide range even by changing effective parameters such as treatment time, pressure and position inside the reactor (Experimental treatment 2 to 6).

Syngas/PICVD, on the other hand, can generate superhydrophilic surfaces (Table 7, treatment 7, CA<5°, Figure 18C), all the way to superhydrophobic (Table 7, treatment 8, CA>150°, Figure 18D), mainly by varying sample position from 14 to 82 cm, treatment pressure from -15 to +15

kPa and absence of hydrogen peroxide as PI. The key parameters influencing hydrophobicity are pressure and location. These are illustrated by comparing treatment 8 and 23: save for pressure, both experiments have the same conditions – a lower pressure (- 15 kPa) leads to more hydrophilic behavior. Similarly, experiment 24, compared to experiment 8, changes only location, showing that positioning the sample closer to the inlet results in hydrophilic behavior. The effect of position can be attributed to the accessibility of syngas-derived radicals, activated monomers and PI-derived species (like OH*) in the reactor [99, 186], while treatment pressure affects the organic chain growth rate and collisions between species and substrate surfaces [99, 187-189]. These effects can also be adjusted to allow intermediate properties to be achieved (Table 7). Moreover, our findings based on tensiometry characterization show that H_2O_2 addition tends to make surfaces more hydrophilic, given that it photo-dissociates under UVC light (peak between 180 and 200 nm) to generate two hydroxyl radicals (OH•) that can actively participate in the radical-driven syngas and form additional oxygen-containing (hydrophilic) groups [99, 166].

Experimental treatments 9 to 12 (Table 7) show that SWCNTs become more hydrophilic as a function of treatment time (from 31° at 60 min to 0° at 180 min), likely as a result of additional functional group deposition. Experimental treatments 9, 13 to 17, show that the H_2/CO molar ratio plays a significant role in the syngas/PICVD treatment ($p < 0.05$). Indeed, molar ratio is known to play a significant role in binary precursor systems [85, 103, 154, 190]. Several authors used binary mixtures consisting of an oxygen-containing monomers (e.g. O_2 or N_2O) and a hydrocarbon (e.g. CH_4 or C_2H_4) to treat SWCNTs [85, 103, 154, 190] and showed that the concentration of certain functionalities (mostly hydroxyl, carbonyl and carboxylic acid groups) can increase along with an increase in the ratio of oxygen- or nitrogen-containing precursors to hydrocarbons. Figure 19 shows that the CA of SWCNTs treated by syngas/PICVD (experimental treatments of 13 to 17 in addition to experimental treatments 9) generally increase as a function of the molar ratio (H_2/CO), likely because fewer oxygen-containing groups are present to increase wetting as the ratio increases. This is confirmed with the overlaid surface tension results. The experimental treatments in Figure 19 are performed at a constant pressure and reactor position – varying these parameters in combination with molar ratio allows for a full range of surface energies to be attained ranging from 0 ° to 156 ° (Table 7).
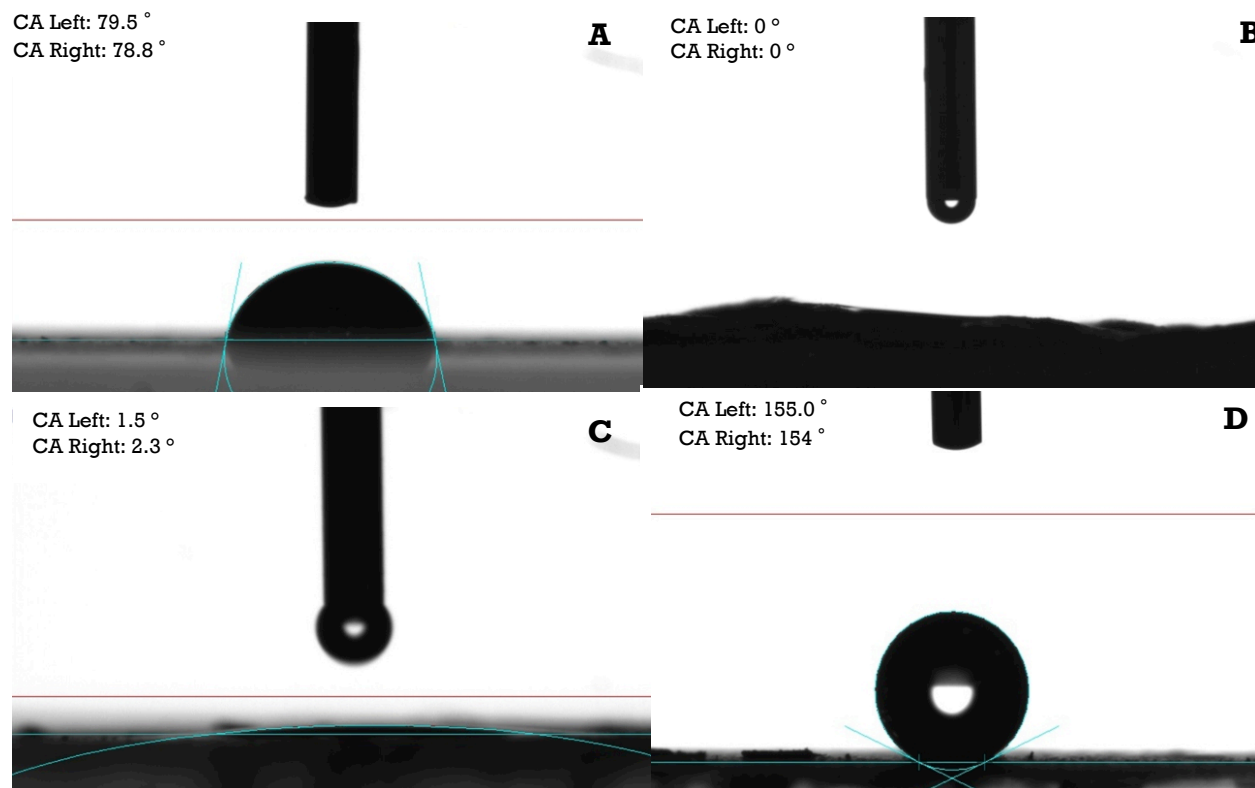
Figure 18. CA measurement obtained by tensiometry A) P-SWCNT (Experimental treatment 1), B) SWCNTs treated by ozone/UV for 1h (Experimental treatment 2), C) SWCNTs treated by syngas/PICVD under vacuum for 3h (Experimental treatment 7), D) SWCNTs treated by syngas/PICVD under pressure for 2h (Experimental treatment 8).

Beyond monomer ratio, our results show that total flow rate in the PICVD reactor can play a role in the final surface properties, given that it will impact residence time in the reactor and, therefore, the probability of collisions between the radicals and the substrate. Except for experimental treatments 18 and 20, all treatments were performed with a total flow rate of 350 ml/min. These two experimental treatments (at 300 and 400 mL/min, respectively), when compared to experiment 17, served to investigate the effect of flow rate. Both experimental treatments 18 and 20 yielded CA higher than at the nominal 350 ml/min flow rate (p-value < 0.05), indicating that hybrid effects may be at play – the reaction domain may switch from deficient to efficient regions (similar to the effect of position). The specific effect of residence time is studied by Farhanian et al (2017) [95]. They reported an increase in film thickness as a function of residence time for a syngas/PICVD system treating flat surfaces [95].
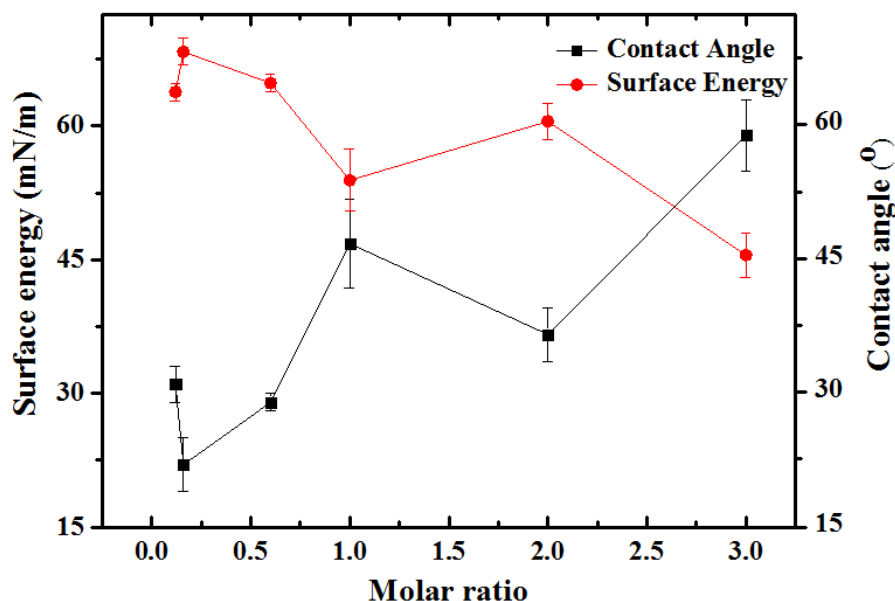
Figure 19. Black squares: Contact angle measurements of T-SWCNTs obtained by tensiometry in terms of molar ratio of H_2/CO; Red circles: Surface energy measurements that have been plotted in terms of molar ratio. Error bars show standard deviation of three measurements.

It is pertinent to note that the surface energy values presented in Table 7, computed using the Owens-Wendt model (Equations 14 and 15), do not consider surface roughness. For this reason, some aberrant values are possible; for example, the surface energy calculated by the tensiometer's software package for experimental treatment 8 (showing superhydrophobic behavior with a contact angle of 156°) is 36 mN/m, nearly unchanged from the far more hydrophilic P-SWCNT (treatment 1, with a contact angle of 79°, 31 mN/m). Given that PICVD treatments on flat surfaces have shown the formation of nanostructured, island-like deposits [95, 191, 192], it is very likely that the increase in roughness plays a large role in the observed wetting behavior.

TEM characterization was done to provide more insight regarding the morphology and structure deposited coatings of T-SWCNTs by syngas/PICVD. Figure 20 show the morphology of SWCNTs before (A,C) and after (B,D) treatment by syngas/PICVD under slight vacuum (-15 kPa, experimental treatment 11). The principal change observed is the appearance of an apparently polymeric layer on the treated sample. The SWCNT diameter grew from 1.4 nm before treatment to 5.3 nm after treatment.

4.3.2 Chemical Characterization

We have determined the chemical properties of SWCNTs treated by ozone/UV or syngas/PICVD treatments using XPS. During ozone/UV treatment, the relative oxygen atomic percentage obtained by XPS survey spectra increased to 20.8% after 30 min (Experimental treatment 3) from untreated P-SWCNTs' 6.9% oxygen content, due to the successful deposition of oxygen-containing groups on the SWCNT surfaces by PICVD (Supplementary Figure A1) (p-value<0.05). HR-XPS fitting of the C1s peak (Supplementary Figure A2) shows 6 major functionalities compared to P-SWCNTs: A) 284.6 eV, corresponding to C=C (sp^2); B) 285.7 eV, corresponding to C=C (sp^2) with defects and C–C (sp^3); C) 286.5 eV, assigned to C–O; D) 288 eV, assigned to C=O and $\pi\rightarrow\pi*$ transition of C=C with defects; E) 289 eV, corresponding to O–C=O; and F) 291.3 eV, assigned to highly delocalized $\pi\rightarrow\pi*$ transition of C=C [193]. Successful incorporation of oxygen-containing groups (mostly –COOH, C=O and -OH) on the SWCNT surfaces after ozone/UV treatment is confirmed, in agreement with previous studies [87].

Raja et al. (2014) had reported successful incorporation of oxygen-containing groups such as carboxylic acid, hydroxyl and carbonyl groups to SWCNTs while they treated SWCNT under ozone/UV or UV and benzophenone [87]. Experimental treatments 2 to 4 were also used to investigate the effect of treatment time in the case of SWCNTs treated by ozone/UV-treated SWCNT (O-T-SWCNT) by applying 60, 30, and 75 min, respectively. As seen in Supplementary Figure A3 (inset), oxygen content reaches a plateau ca. 20-26% after 30 min. However, Supplementary Figure A3 (over plot of C1s HR-XPS spectra of SWCNTs treated by ozone/UV with 60, 30, and 75 min) did not show a significant difference as a function of treatment time. Vautard et al. (2012) reported gas-phase surface treatment of carbon nanofibers in a reactive ozone environment with residence times on the order of 2 min. Their results are in agreement with ours, showing successful incorporation of oxygen-containing groups onto carbon nanofibers [193].
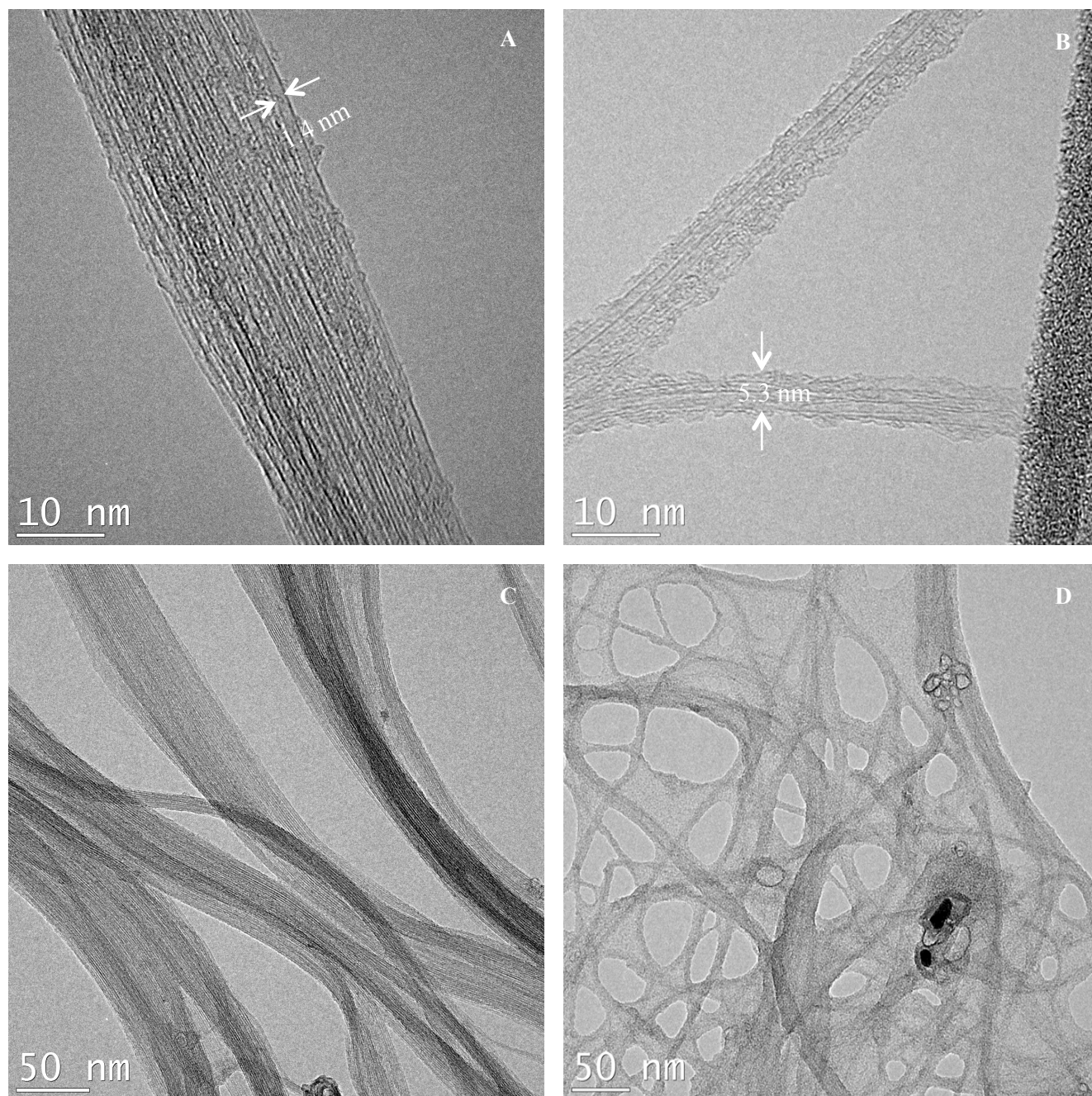
Figure 20. TEM micrographs of A: P-SWCNTs (Experimental treatment 1), B: Syngas Treated SWCNTs (Experimental treatment 11), C: P-SWCNTs with lower magnification (Experimental treatment 1), D: Syngas treated in lower magnification (Experimental treatment 11).

The oxygen content of syngas/PICVD-treated SWCNTs (S-T-SWCNTs, Experimental treatment 1) climbed to 60.1%, with the balance being carbon (18.1%) and iron (21.8%) (Supplementary Figure A1). The presence of iron (binding energy of 714.4 eV) can be attributed to iron

pentacarbonyl (Fe(CO)$_5$) in the CO tank, a common impurity that forms over time in steel tanks exposed to CO; it can readily decompose under the action of heat or UVC light [194]. Figure 21A and 21B show C1s and O1s HR-XPS spectra of P-SWCNTs to provide comparison with the treated SWCNTs. According to the C1s HR-XPS spectra (Figure 21C), the syngas-based coating was composed of C-C, hydroxyl (-OH), carboxylic acid (COOH), and carbonate groups, corresponding to binding energies of 285, 286.7, 288.9, and 289.8 eV, respectively. Interestingly, the C1s peak for the treated sample became wider, compared to the untreated sample's more sharp and narrow peak, implying that the coating completely covered the SWCNT surface [195]. Based on the O1s spectra (Figure 21D), S-T-SWCNTs have two major peaks at binding energies of 530 and 531.65 eV, which are assigned to O-Fe (or Fe$_2$O$_3$) and C-OH, respectively (though Fe(OH)$_3$, phenol and O=C-O-Fe are also possible) [193]. Based on the Fe2p high resolution XPS spectra (Figure 21E), deposited iron species consisted of Fe$_2$O$_3$, FeOOH, and Fe$_3$O$_4$ based on peaks at binding energies of 710.55, 713.55, and 718.75 eV, respectively [193]. The Fe$_2$O$_3$ and Fe$_3$O$_4$ are likely the result of decomposition initiated by the 185 nm peak (as discussed earlier), or through degradation of Fe(CO)$_2$ radicals through collision with reactive species and hydrogen peroxide. Overall, the iron content is essentially in the form of HO-Fe-O, Fe(OH)$_3$ and FeCO due to chemical bond beween iron and carbon.
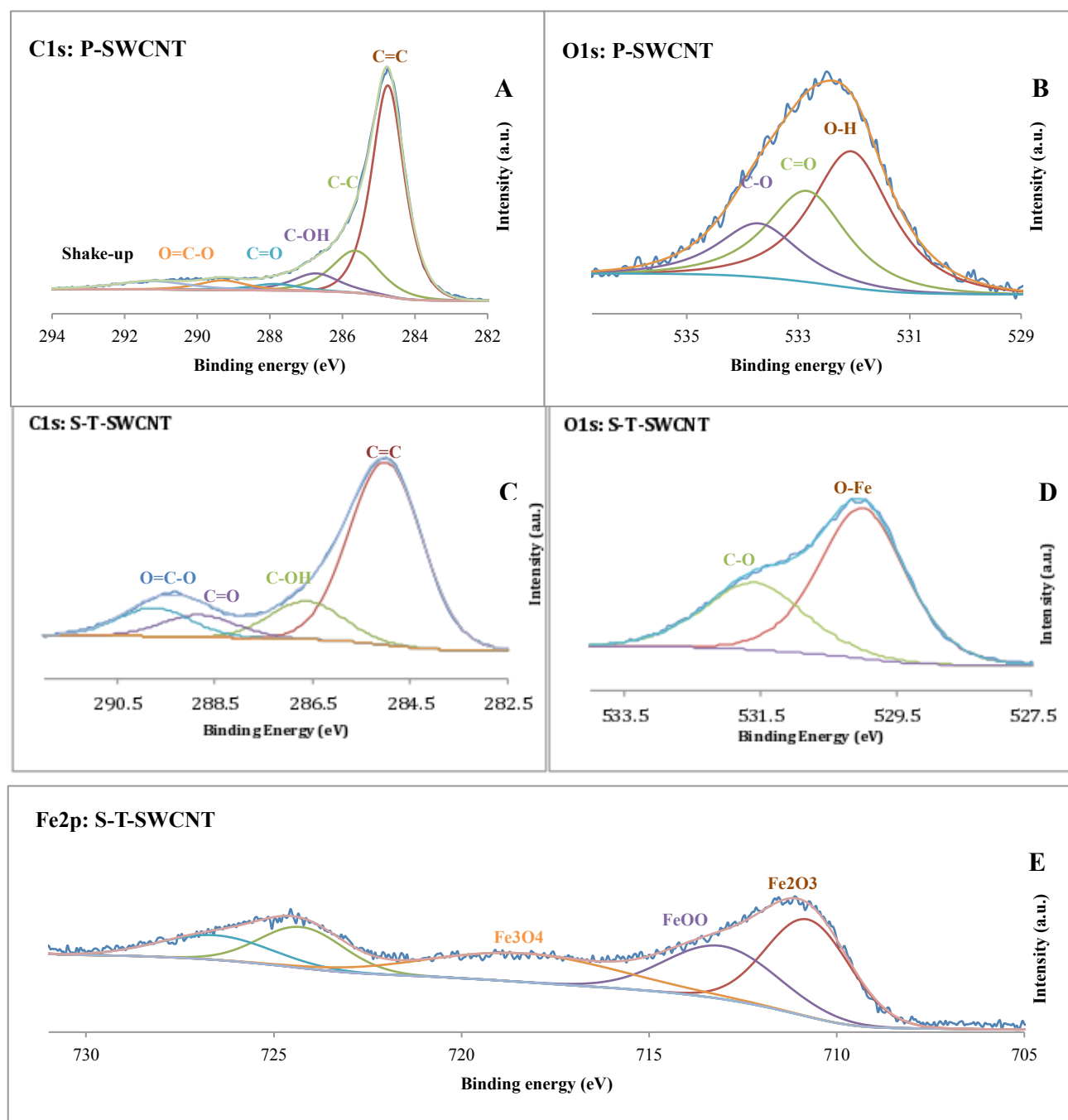
Figure 21. A: High resolution C1s spectra of P-SWCNT (Experimental treatment 1); B: High resolution O1s spectra of P-SWCNT (Experimental treatment 1); C: High resolution C1s spectra of S-T-SWCNT (Experimental treatment 11); D: High resolution O1s spectra of Treated SWCNT (Experimental treatment 11); E: High resolution Fe2P spectra of T-SWCNT (Experimental treatment 11).

To elucidate the role and effect of each individual precursor (H_2, CO, H_2O_2) on coating composition, we performed some blank experiments on glass substrates (thereby eliminating interactions that may occur with SWCNT) (supplementary Table A2). The C1s HR-XPS spectra for bare glass (supplementary Figure A4A) showed four peaks at binding energies of 285, 286.75, 288.78 and 288.46 eV, assigned to aliphatic carbon or C-C, C-OH and carboxylic acid (COOH) groups, respectively (carbon sourced from airborne contaminants). The O1s spectra (supplementary Figure A4B) showed two peaks at binding energies of 531.30 and 532.62 eV, corresponding to OH and SiO_2 groups, respectively. After treatment with CO, H_2 and H_2O_2, the same results and structure as those observed on SWCNTs were obtained. Compared to bare glass, the C1s spectra (supplementary Figure A4C) showed two additional peaks, namely C-Fe and carbonyl groups at binding energies of 284.1 and 290.26 eV, respectively. Moreover, treated glass exhibited decreased hydroxyl groups and significantly increased carboxylic groups. The O1s spectra (supplementary Figure A4D) showed three new peaks at binding energies of 530.18, 531.67 and 532.61 eV assigned to O-Fe, C-OH groups and O=C-O-Fe, respectively.

In the absence of H_2O_2 (CO and H_2 only), treatment lead to the appearance of two extra peaks compared to bare glass, at binding energies of 284.33 and 289.55 eV (supplementary Figure A4E). These correspond to C-Fe (or C-Si, as Si could be still seen after treatment in survey peaks), and carbonate groups (adsorbed CO_2), respectively. The spectra are generally similar to the CO+H_2+H_2O_2 case, with increased carboxylic (COOH or COOC) and decreased carbon-bonded hydroxyl groups in the structure. The O1s spectra (supplementary Figure A4F) also showed three peaks at binding energies of 530.18, 531.67 and 532.61 eV assigned to O-Fe, OH and O=C-O-Fe, respectively. While the chemical differences appear small, the film produced in the absence of H_2O_2 showed significant morphological differences: it appeared as a powder adsorbed on the substrate (not a bound film) and could be removed by shaking lightly. Based on this observation, we can conclude that H_2O_2 plays a determinant role as both a photo-initiator and during film formation.

Knowing that CO can absorb light below 200 nm [99] (including the 185 nm emission peak from the Hg lamps), and that it contains $Fe(CO)_5$, it may lead to deposition without the addition of H_2. When combining CO with H_2O_2 (without hydrogen), the C1s spectra (supplementary Figure A4G) shows two peaks not present for bare glass at binding energies of 283.9 and 287.3 eV, assigned to C-Fe and C=O, respectively. The peak at binding energy 289.3 eV was also quite

significant compared to its bare glass counterpart – it corresponds to carboxylic acid groups bonded to carbon. The O1s spectra (supplementary Figure A4H) showed three peaks (530.19, 532.06 and 533.05 eV) assigned to Fe-O (or Fe(OH)O or Fe_3O_4), O-Si and chemisorded H_2O. As expected, combining H_2O_2 with only H_2 lead to no deposit and HR-XPS spectra (supplementary Figure A4I and A4J) identical to bare glass.

4.3.2.1 Thermal Stability and Defects

In order to quantify deposited functionalities on SWCNTs, we performed TGA analyses. Figure 22 shows TGA and Derivative Thermogravimetric Analysis (DTGA) of P-SWCNTs (experimental treatment 1), S-T-SWCNTs ($CO+H_2+H_2O_2$, experimental treatment 11) and SWCNT exposed to UVC light as a blank experiment. The DTGA graph of P-SWCNT shows two peaks around 618.5 and 542.4 °C, assigned to SWCNTs with sp^2 hybridization and disordered SWCNTs with sp^3 hybridizations, respectively [196]. The P-SWCNTs showed 77.2% carbon with sp^2 hybridization and 14.9% residue which corresponds to metallic and inorganic impurities. There are no significant differences or decomposition shifts between P-SWCNT and SWCNT exposed to UV light. Using the mass loss of P-SWCNTs at 360 °C as a reference (10%), the mass loss of S-T-SWCNTs is about 26%, meaning that treatment leads to decomposition at a lower temperature. This is consistent with previous work where it was shown that a higher amount of functionalities leads to a lower degradation temperature because of more treatment-induced physical defects on the tubes' surfaces and end-caps [87]. The DTGA of S-T-SWCNT shows two new peaks around ca. 113°C and 329°C which are related to oxygen-containing groups and carbon coating on SWCNTs, respectively [197]. The SWCNT peak is also shifted to lower temperatures (from 618.5 to 451.3°C) after treatment (consistent with mass loss results). S-T-SWCNTs presented 0.7% humidity, 19.5% deposited carbon with sp^3 hybridization, 38.7% carbon with sp^2 hybridization and 35% metallic residue. The increase of iron content agrees with XPS results (presence of iron).
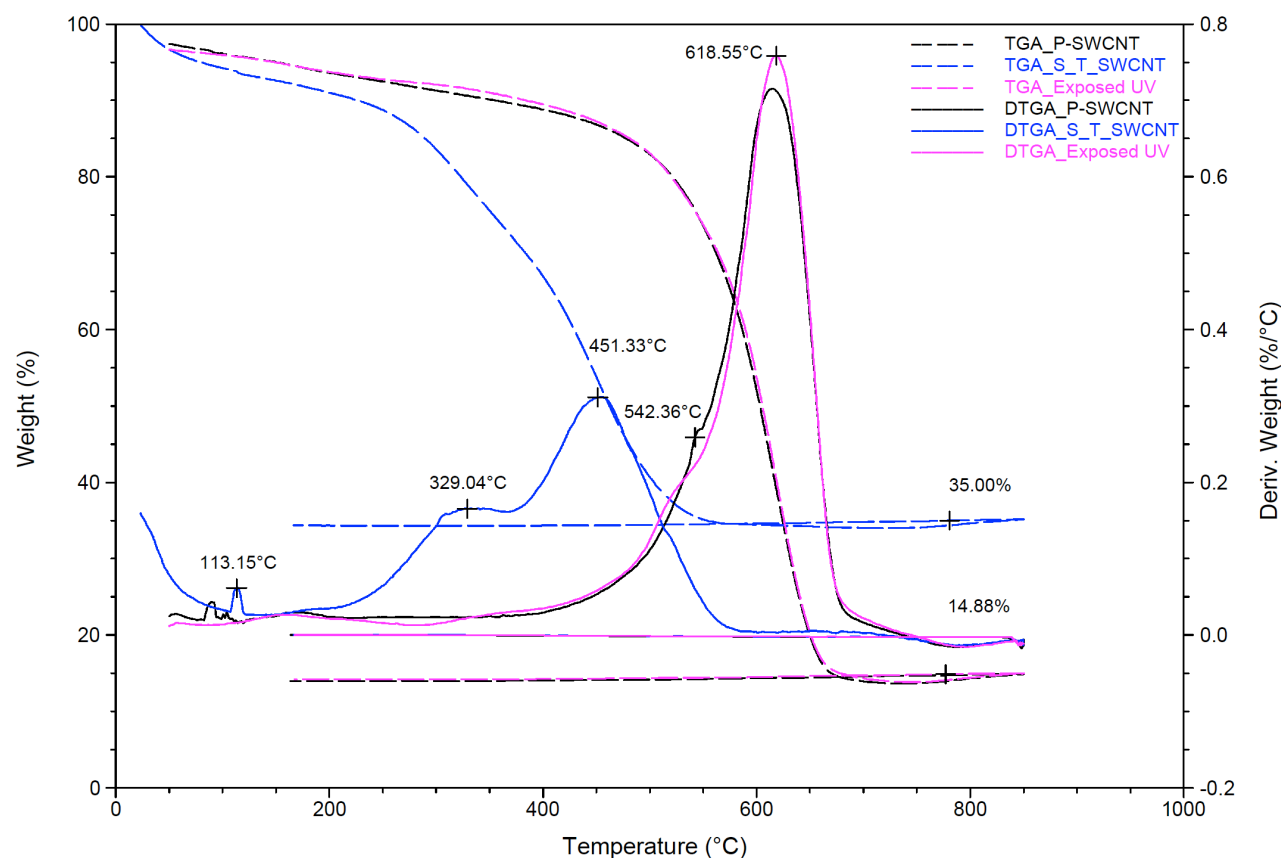
Figure 22. TGA/DTGA graphs comparing thermal mass loss of P-SWCNTs (Experimental treatment 1), SWCNTs exposed to UV and S-T-SWCNTs treated (Experimental treatment 11).

We characterized T-SWCNTs by Raman spectroscopy to study their hexagonal structure after treatments. Table 8 (extracted from Figure A5 in supplementary results) shows the Raman spectrum results used to assess SWCNT integrity. The ratio of D- to G-bands in Raman spectra presents defects produced in the hexagonal structure [181]. This ratio is lower for P-SWCNT and increases as a function of treatment time, confirming the tensiometry and XPS findings. If we assume that the D/G ratio is assigned strictly to presence of functionalities producing structural defect sites, the Raman results are also in agreement with the TEM observations (longer treatment leads to a thicker, amorphous carbon coating – from experimental treatment 1 (0 min) to experimental treatment 9 (60 min) to experimental treatment 11 (120 min) to experimental treatment 12 (180 min)) [154]. In the case of 2h treatments, two different molar ratios, namely 0.12 and 2, were evaluated (Experiments 11 and 21). The higher molar ratio (Experimental treatment 21) leads to higher D/G ratio, even higher than that of the long treatment time at low

ratio (Experimental treatment 12). This could be explained by the fact that increasing the H_2/CO molar ratio leads to an organic film with a higher amount of saturated carbon (with oxygen carried away, likely in the form of water).

Table 8. D/G band ratio of SWCNTs before and after treatment at different time obtained by Raman spectra.

Samples	Related Experimental Treatment	Time (h)	D/G Bond Ratio
P-SWCNT	1	-	0.29
S-T-SWCNT	9	1	0.34
S-T-SWCNT	11	2	0.36
S-T-SWCNT	12	1	0.43
S-T-SWCNT	21	2	0.58

4.3.3 Treatment Homogeneity and Dispersibility of SWCNTs

Homogeneous treatment of SWCNT buckypapers will be an important factor in many applications, including polymer nanocomposites or sensors, in which unfunctionalizaed areas may deteriorate mechanical and electrical properties and overshadow the SWCNT's performance improvements [198]. We have performed XPS mapping of three typical SWCNT samples to verify homogeneity of surface coatings (Table 9, experimental treatments 1, 9 and 11) at three different regions on the samples (the head/position P1, middle/P2 and end/P3). Carbon, oxygen and iron content is nearly identical at all positions, confirming that the treatment is homogeneous.

Table 9. XPS mapping results and their experimental conditions.

Samples		Characterization								
		O1s			C1s			Fe2p		
		P1	P2	P3	P1	P2	P3	P1	P2	P3
Test 1	1	6.4	6.9	6.6	92.7	92	92	-	-	-
	9	11	12	11	85.7	84.6	85.3	2.4	2.4	2.5
	11	20.5	20.8	17.8	67.5	66.4	72.4	10.5	11	8.2
Test 2	9	8	9	7	90	88.4	91.3	0.7	1.1	0.7
	11	19.3	15.4	16.6	70	78.7	75	9	4.6	7.2

However, this homogeneity may not hold over the full thickness of the bucky paper sample used. Given that many biological assays are conducted SWCNTs in suspension, through-the-thickness heterogeneity may be an issue. To evaluate dispersion, samples exhibiting superhydrophilic behaviors (Experimental treatment 11) were dispersed in deionized water at a concentration of 0.05 g/mL. After sonicating for 60 minutes, the samples were allowed to settle. Untreated SWCNT samples from areas not reached by the PICVD treatment settled out, while treated S-T-SWCNTs remained in suspension (Figure 23A). Sediments were removed through decantation and the supernatants remained stable for at least 24 h (Figure 23B). The "supernatant SWCNTs" are the samples that could be used for cytotoxicity assessments before applying them in biomedical devices. Furthermore, the treatment resists sterilization by immersion of the sample container in a boiling water bath for 30 min (variation in CA <5° before and after boiling, data not reported).

Beyond sterilization in suspension, the S-T-SWCNTs exhibited exceptional stability, hydrophobic samples (from experimental treatment 8) remained at 151±2° after 7 days (ambient conditions), while hydrophilic samples (from experimental treatments 11 and 12) increased to 7±4°. This so-called "hydrophobic recovery" of the hydrophilic-treated sample is a well-documented ageing phenomenon, dependent on absorption of contaminations, reorientation and reconstruction of dangling groups on the surface [13, 46]. However, this phenomenon can be significantly reduced in cross-linking modified surfaces [199]. These dispersion assays demonstrate the change in wettability of individual S-T-SWCNT; dispersion into a wide variety of solvents is the focus of on-going work.
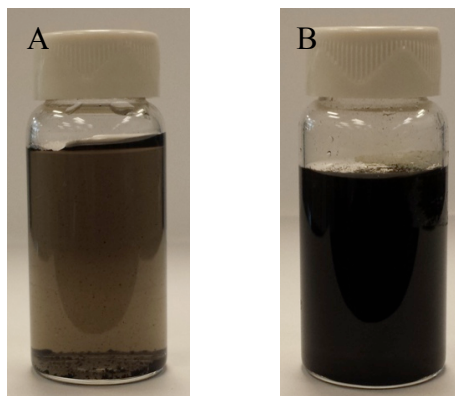
Figure 23. A) Dispersion of T-SWCNTs in deionized water after 24h, B) Well dispersion of T-SWCNTs under vacuum in deionized water upon treatment.

4.4 Conclusions

In this study, we compared treatment of SWCNTs by ozone/UV and syngas/PICVD. The main objective of this project was to functionalize SWCNTs with various surface energies ranging from superhydrophilic to superhydrophobic. Although treatment of SWCNTs by ozone/UV was straightforward and superhydrophilic SWCNTs could be obtained in a short time, this method could not meet the main goal of the project. Syngas/PICVD on the other hand provides an efficient method to fabricate functionalized SWCNTs with oxygen-containing groups in a full range of surface energies (ranging from superhydrophilic to superhydrophobic behaviour). Molar ratio of the H_2/CO precursor mix, pressure and treatment time were found to have significant effects during treatment. The PICVD induced coating on the SWCNTs was chemically characterized and proved to be homogeneous (on the surface) and exceptionally stable (including being subjected to boiling for sterilization purposes). This approach is therefore viable as a technique to be used in various applications such as nanocomposites, aerospace and bio applications, in which various degrees of functionality (and consequently surface energies) are desirable. Furthermore, this method will be applicable to investigate the true effect of surface energy on cytotoxicity, which will be the focus of subsequent work.

Acknowledgments

CHAPTER 5   ARTICLE 2: REACTION KINETICS AND TEMPERATURE EFFECTS IN SYNGAS PHOTO-INITIATED CHEMICAL VAPOUR DEPOSITION ON SINGLE-WALLED CARBON NANOTUBES

Seyedehsan Hosseininasab [a], Nathalie Faucheux [b], Gervais Soucy [b] and Jason R. Tavares [a,*]

[a] *Department of Chemical Engineering, Polytechnique Montreal, Montreal, Québec H3T 1J4, Canada*

[b] *Department of Chemical and Biotechnological Engineering, Université de Sherbrooke, Sherbrooke, Québec J1K 2R1, Canada*

ABSTRACT

Photo-initiated chemical vapor deposition (PICVD) is a solvent-free process that can be used to produce thin films on a variety of substrates, with applications in fields ranging from biomedicine to optics and microelectronics. This study presents a kinetic analysis for this process using syngas ($CO+H_2$) as a precursor for the surface treatment of single walled carbon nanotubes (SWCNT) with average dimensions of 1.5×100 nm (diameter $\times$ length), and addresses the role of iron pentacarbonyl ($Fe(CO)_5$), a photo-active contaminant found in CO. This work builds upon previously-developed reaction schemes for PICVD, based mainly on surface characterizations, by coupling these analyses with gas-phase monitoring. This allows us to propose two separate reaction schemes for the gas and surface phase reactions and consider temperature effects. On-line FTIR, off-line GC-MS and on-line GC characterized the gas phase, while for surface characterizations, XPS and TGA were used. Characterizations showed that a coating with a general formula of $C_nO_{3n}Fe_n$ was deposited, corresponding to 0.29 ± 0.04 mg carbon and 0.49 ± 0.03 mg iron on the SWCNT substrate over the course of treatment. The $Fe(CO)_5$ was identified as the key reactant in syngas/PICVD reactions and was nearly completely consumed (94%). Mass balances derived from the gas phase characterization showed that $Fe(CO)_5$ inputted to the plug flow reactor could potentially contribute the entire amount of 0.49 ± 0.03 mg of Fe and 0.29 ± 0.04 mg of C to the coating on the SWCNT, indicating that syngas/PICVD can be optimized in the future to decrease gas throughput. Temperature did not show a significant effect in the case of PICVD. However, in the absence of ultraviolet light, its role becomes determinant, with rising temperatures causing more Fe deposition.

5.1 Introduction

Chemical vapor deposition (CVD) is a process used in the semiconductor industry to produce thin films. The use of thin solid films is widespread - they are used in different technological areas such as microelectronics (integrated circuits, transistors), optical devices (laser, fibers), magnetic materials, solar energy conversion and the ceramics industry [99]. CVD can be classified into three major processes, namely thermally activated CVD (TACVD), plasma enhanced CVD (PECVD), and photo-initiated CVD (PICVD). In PICVD, chemical reactions are initiated by light photons [95, 99] making use of various photo-sensitive precursors such as

ethylene (C_2H_4) [86, 154], butadiene (C_4H_6) [86], hydrogen sulfide (H_2S) [86], ammonia (NH_3) [85], and ozone (O_3) [87] to synthesize the desired coatings. For example, Kasparek et al. (2016) co-polymerized a gas mixture of ethylene/butadiene with hydrogen sulfide (H_2S) to obtain thiol-terminated thin films under vacuum-ultraviolet (VUV) irradiation [86]. Precursor selection depends on the desired film properties and the available excitation wavelength of the light source [101]. The resulting film features are affected by kinetic and operational parameters such as choice of precursors, their respective flow rates (and molar ratio), their residence time in the system, the total pressure in the reactor, and the substrate temperature [16, 101]. In particular, residence time can be directly related to other processing parameters such as treatment time, sample position inside the reactor and total flow rate of precursors, namely when using syngas ($CO+H_2$) as the precursor (identified herein as syngas/PICVD or PICVD) [200]. PICVD has demonstrated wide potential as a solvent-free surface engineering tool, able to deposit coatings and treat various surface geometries (nanoparticles to flat substrates) under ambient conditions. This ability to operate at or near atmospheric pressure simplifies implementation, but complexifies the chemistry, as various simultaneous and interdependent processes take place, including homogeneous gas phase reactions (leading to reactive species formation), transport of these reactive species to the surface by passing the boundary layer, chemisorption/physisorption and desorption at the substrate surface [201], and heterogeneous reactions on the substrate yielding a solid functional deposit. This complexity is compounded by the presence of unexpected compounds, such iron pentacarbonyl ($Fe(CO)_5$), a photo-active contaminant found in CO [96].

$Fe(CO)_5$ forms over time inside steel CO cylinders, through a reaction with the cylinder wall at high-pressure [202]. Its absorption cross section peaks at wavelengths between 200 and 350 nm [203], meaning that it is readily dissociated by the light emitted by low-pressure Hg discharge germicidal ultraviolet C (UVC) lamps used in recent PICVD work to form reactive intermediates [203, 204]. The thermal decomposition of $Fe(CO)_5$ is reported between 160 and 300 °C and forms Fe (III) oxide intermediates and iron oxide particles [205, 206]. Our group previously suggested a preliminary kinetic model for PICVD based on surface characterizations [95, 99]. Dion et al. (2014) applied PICVD to functionalize flat surfaces under UVC light (253.7 nm) and they proposed a set of reactions based on Fischer–Tropsch synthesis [99]. In their kinetic model, CO and H_2 played the leading roles and the $Fe(CO)_5$ contribution was not considered. Farhanian

et al. (2017) further detailed the reaction kinetics when treating silicon substrates - although $Fe(CO)_5$ was considered in this kinetic model, the growth and termination reactions were mostly based on CO and H_2 [95]. Considering the fact that syngas/PICVD is a flexible and promising method to change the surface properties of nanomaterials, it is necessary to clarify the reaction mechanisms at play for process scale-up to be eventually considered.

Our previous work [200] aimed to tailor the surface properties of single-wall carbon nanotubes (SWCNTs) using PICVD, as these fascinating materials have various applications exploiting their unique properties (such as high electrical conductivity and tensile strength [207]), but require surface modification for example to alter their wettability to facilitate their use in polar media (a key requirement for biomedical applications). Given the potential of these nanomaterials, and the need to improve our understanding of the PICVD process, the present work deals with the in-depth kinetic modeling of PICVD considering both gas and surface phase reactions, as well as temperature effects on the functionalization of SWCNTs. To see how temperature affects precursor concentrations and deposition rates, we also investigated the functionalization of SWCNTs with TACVD, in which the light excitation of PICVD is replaced by heating. In the proposed model, we considered various kinetic parameters such as reaction rate of $Fe(CO)_5$ and temperature. The kinetic parameters are obtained experimentally.

5.2 Materials and Methods

5.2.1 Materials

Pure SWCNTs (P-SWCNTs) (96.5% w/w), syngas (CO and H_2, 99.97%), argon (99.9%) and hydrogen peroxide (H_2O_2, 50% (w/w)), were purchased from Raymor-NanoIntegris, Air Liquide, and Fisher Scientific (Montreal, Quebec), respectively. Liquid iron pentacarbonyl ($Fe(CO)_5$, >99.99%) was purchased from Sigma-Aldrich. CO and CO_2 calibration gas cylinders were purchased from Air Liquide. Two 96 cm-long UVC germicidal lamps (Model T-97505-80, Cole-Parmer Inc, low pressure Hg discharge, irradiance of 0.01 W/cm^2 at 3.5 cm) with the main and minor emission peaks at 253.7 and 185 nm, respectively, were used for all experimental treatments.

5.2.2 Experimental Procedures and Conditions

The PICVD reactor used in this study consisted of a 25-mm internal diameter quartz tube reactor illuminated by two UVC lamps, with gas flow supplied through three mass flow controllers (Brooks, series 5850E) and a syringe pump for photo-initiator (PI) injection (Figure 24) [200]. SWCNT samples to be treated (in the form of bucky paper) were placed 30 cm from the reactor inlet, on a sample holder held at 45° with respect to the gas flow. After purging the reactor with argon, CO (containing traces of $Fe(CO)_5$, evaluated at 6.7±0.2 ppm/min, Figure B1 in supplementary results) and H_2 were injected with a molar ratio of 0.12 and a total flow of 400 ml/min. Hydrogen peroxide was continuously injected at a flow rate of 1 mL/h flow rate during the treatment. Except when otherwise specified, all surfaces were treated for 60 min under a pressure of 18.5 kPa (gauge pressure). Various temperatures (25-200 ℃) were applied to the sample holder, using a built-in electrical heater. A thermocouple was located right below the sample to monitor the temperature. In the course of this study, error bars (±) represent the standard deviation.
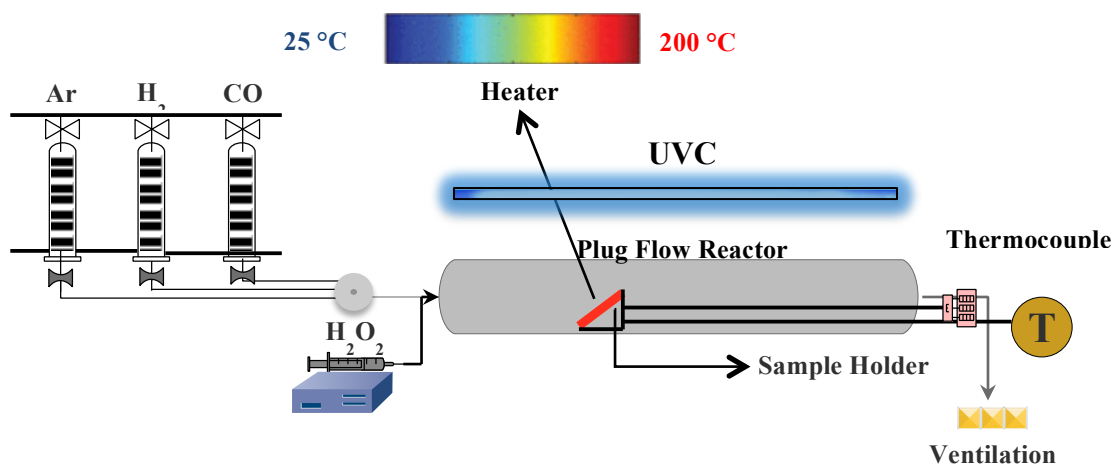
Figure 24. Schematic of the PICVD reactor.

5.2.3 Surface and Gas Phase Characterization

The outlet gas (composed mainly of CO, H_2 and $Fe(CO)_5$) was analyzed with a Nicolet iS5 Fourier Transform Infrared (FT-IR) spectrometer operated in transmission mode with a quartz flow cell (Pike). Each spectrum is the result of 256 scans ranging from 500 to 4000 cm^{-1} at resolutions of 16 cm^{-1}. Gas chromatography mass spectroscopy (GC-MS) (Agilent 5975C VL

MSD Triple Axis) equipped with two columns (Molsieve 5A and HayeSep N columns, California, USA) characterized gas samples. For CO and CO_2 quantifications, the HayeSep N column (80/100 Mesh 0.5m×1.8") was used, while less stable components such as organic materials or $Fe(CO)_5$ were characterized with the Molsieve 5A column (13×80/100 Mesh 1.5m×1/8"). Helium served as carrier gas (flow rate of 0.5 mL/min). The gas samples analyzed were collected from the PICVD reactor using a Tedlar bag. For $Fe(CO)_5$ quantifications, 10 µl volume samples were injected to the GC-MS, while in the case of CO/CO_2, the column was first purged and then filled by the sample. The oven temperature had an isotherm at 45 °C for 20 min, and then increased linearly from 45 to 230 °C, until a total analysis time of 90 min was reached. Three $Fe(CO)_5$ samples diluted in toluene with concentrations of 0.1, 0.5, and 100 ppm were used for calibration of the GC-MS signal (Figure B1, supplementary information). Here, based on the NIST 2010 library, components with a quality percentage over 90% are identified and reported [208] . To further quantify H_2, CO, O_2, N_2, C_2-C_4 hydrocarbons and CO_2, micro-gas chromatography (Varian CP-4900 Micro Gas Chromatograph) was used as well.

All treated samples (SWCNT sheets) were characterized via X-ray photoelectron spectroscopy (XPS) (VG ESCALAB 3 MKII system using a Mg Kα source), with 100 eV pass energy in 1 eV energy step size applied for survey scans. To obtain more insight into the composition of treated samples, high-resolution (HR) spectra were collected, with 20 eV pass energy in 0.05 eV increments. All peaks were fitted as per Yang and Sacher's approach [179].

Thermogravimetric analyses (TGA) of the treated SWCNTs were performed with a Q500 TA instrument under air, over a temperature range of 30-800 °C and a heating rate of 10 °C/min (around 4.5 mg samples in a platinum TGA pan).

5.3   Results and Discussion

5.3.1 Surface Characterization

5.3.1.1 X-ray Photoelectron Spectroscopy

We previously studied surface treatment of SWCNTs using PICVD and characterized the surface chemistry extensively by XPS [200]. Briefly, the survey XPS spectra showed approximately 20% at. carbon (C), 20% at. iron (Fe) and 60% at. oxygen (O) on the surface (Figure 25). Conversion

of these values into weight percentages leads to 46.7 wt% of Fe, 11.1 wt% of C, and 42.2 wt% of O. The surface chemistry (atomic percentage of functional groups) does not vary as a function of treatment time, for treatment times greater than 35 min, at which point the SWCNT surfaces were covered completely by the coating [95]. This implies that an oligomeric coating with a surface atomic structure of "$C_nO_{3n}Fe_n$" deposited on the surface of SWCNT buckypapers. Farhanian et al. (2017) previously showed a linear relation between film thickness and treatment time in syngas/PICVD treatments, on a silicon substrate, with a deposition rate of 0.7 nm/min (for a total syngas flow of 400 mL/min, a residence time of 0.6 min, and treatments durations of 30-180 min) [95]. Studying the high-resolution C1s peak, treated SWCNTs show four major functionalities compared to purified, untreated SWCNTs (P-SWCNTs): C-C, -OH, -COOH and carbonate groups with binding energies of 285, 286.7, 288.9, and 289.8 eV, respectively. As previously shown, the surface is completely and homogeneously covered by the coating [200]. The O1s peak shows two peaks of interest at binding energies of 530 and 531.65 eV, assigned to O-Fe (or Fe_2O_3) and C-OH (or $Fe(OH)_3$), respectively [193]. The Fe2p peak confirms that Fe is in the form of Fe_2O_3, $Fe(OH)_n$ and Fe_3O_4 with subpeaks at binding energies of 710.55, 713.55, and 718.75 eV, respectively [193].
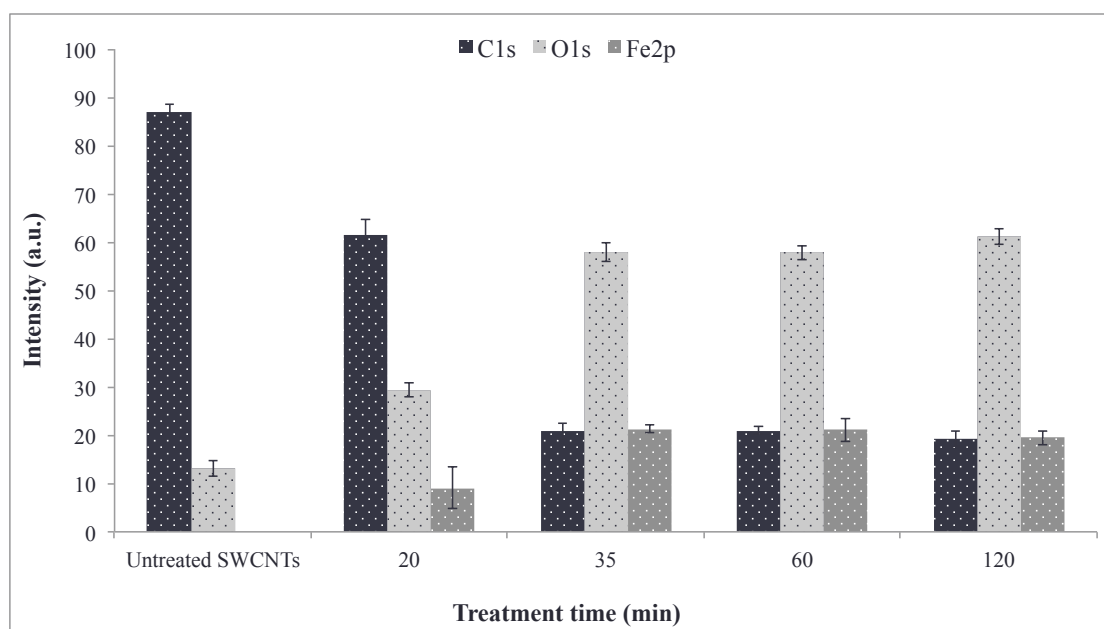
Figure 25. Elemental surface composition of SWCNTs treated by PICVD without heating as a function of treatment time.

Temperature is a key thermodynamic parameter that can influence the surface chemistry of coatings [16, 209]. Therefore, we varied the substrate temperature (both with and without UVC illumination, from 25 to 200°C) and assessed the surface composition via XPS (Figure 26). From 100°C onwards (with the UVC lamps on), we never had complete surface coverage of the substrate, illustrated by the appearance of C=C bands from the SWCNT surface in high-resolution XPS scans (Figure B2, supplementary results). The coating thickness was therefore either below the detection limit of the XPS (detection limit of XPS at most 10 nm) or completely absent in certain areas. In other words, the adsorption of reactive species is limited by rising temperature (thermal desorption) [210]. Coating composition is generally similar, namely with respect to O-Fe and O-C functionalities, although oxygen-containing functionalities do increase with temperature (Figure 27).
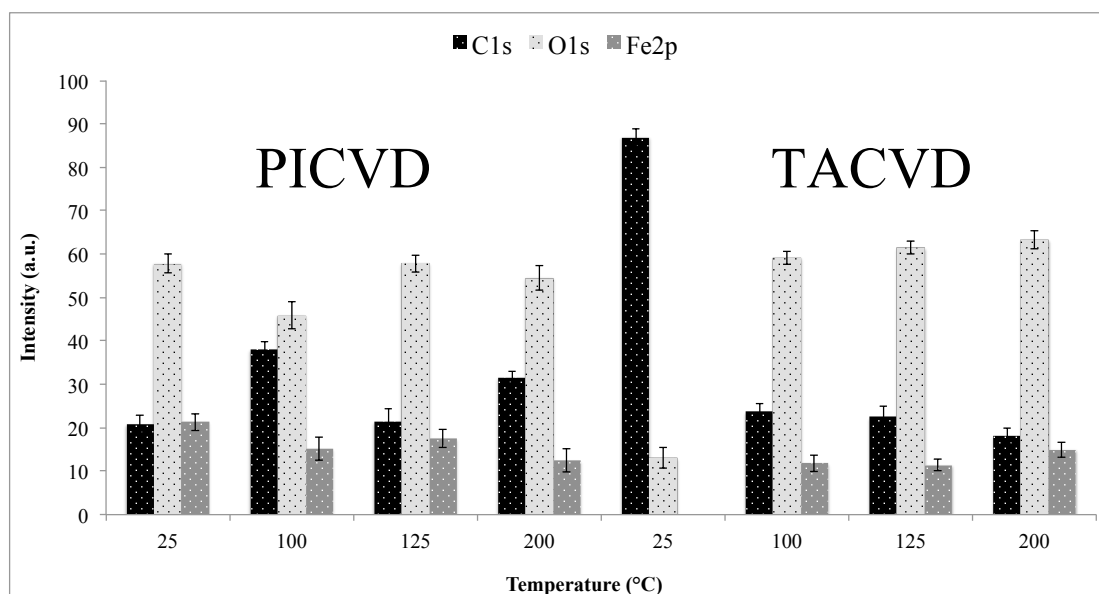
Figure 26. Atomic percentage of carbon, iron and oxygen deposited on SWCNTs after PICVD (left) and TACVD (right) treatments at temperatures ranging from 25 to 200 °C.

When the UVC light is off (TACVD), the effect of temperature can clearly be assessed. At room temperature, there is no deposition (the elemental composition corresponds directly to that of P-SWCNTs). Based on XPS survey scans, as temperature increases, C content decreases, while Fe increases. HR-XPS results showed that the preponderance of Fe functionalities (such as O-Fe) is greater than O-C functionalities - which is different from the case where heat is combined with

UVC (Figure B3, supplementary results) – and this is accentuated by increasing temperature. Based on an overlay of C1s HR-XPS (Figure B3, supplementary results), TACVD treatments led to a coating with a higher content of oxygen-containing groups compared to PICVD (with or without heat), consistent with observations by [205, 206]. This demonstrates that the heat- and light-driven decomposition pathways for Fe(CO)$_5$ are different. That being said, according to Figure 26, a TACVD treatment at 200 °C, leads to an elemental surface composition close to that of room-temperature PICVD. The addition of heat is not without effect however – at temperatures higher than that of the thermal decomposition of Fe(CO)$_5$ (160°C) in the case of PICVD, coatings with different composition (more oxygen containing functionalities, especially COOH) compared to room-temperature PICVD were formed (Figure 27). It is worth mentioning that after all UVC-based treatments, the PICVD reactor and SWCNT substrates became yellowish, while TACVD treatments did not lead to any color change.
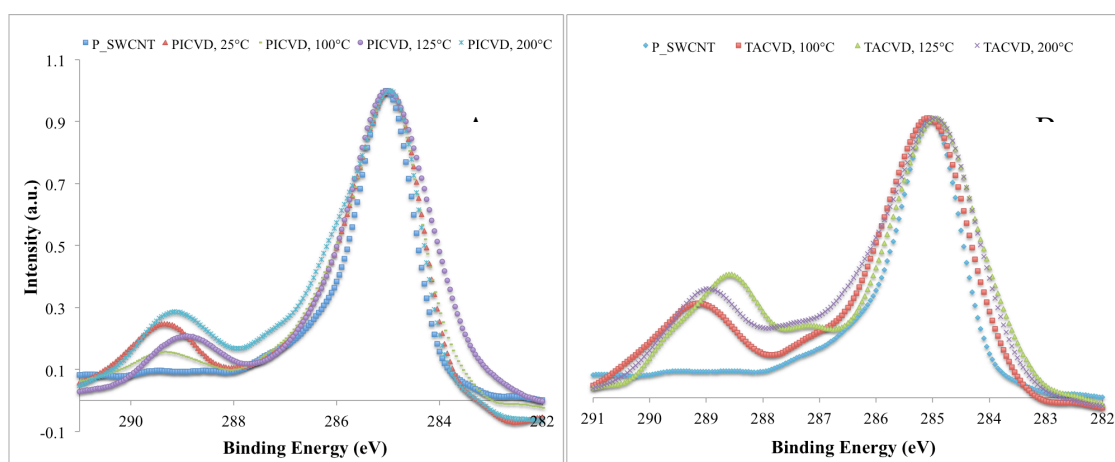
Figure 27. HR-XPS C1s peak of (A) treated SWCNTs by PICVD at temperatures of 25, 100, 125, and 200 °C; (B) treated SWCNTs by TACVD at temperatures 25, 100, 125, and 200 °C while they are compared with (P-SWCNTs).

5.3.1.2 TGA Characterization

The deposits formed both with and without UVC illumination, at room temperature and at 200 °C, were quantified via TGA analyses. The data presented in Figure 28 is extracted from the raw TGA and DTGA information presented in Figure B4 in supplementary information. This interpretation, based on [196, 197], shows that a 4.51 mg samples of P-SWCNTs is composed of 3.43±0.11 mg C=C carbon (76.1±3.0% w/w, from the SWCNT structure), 0.42±0.03 mg

humidity (9.5±0.8%, w/w) and 0.65±0.11 mg residue (14.5±2.9%, w/w). The residue is composed of graphitic C, soot and most importantly metallic species such as Fe (sourced in this case from the catalyst used for SWCNT growth [211, 212]). After PICVD treatment, SWCNT samples weighing 4.27 mg were composed of 1.98±0.04 mg C=C carbon (46.4±0.9%, w/w) and 1.64±0.03 mg residue (38.5±0.7%, w/w), with a new DTGA peak assigned to deposited C (in the form of C-C) accounting for 0.29±0.04 mg (6.7±1.0%, w/w) (remainder is humidity). In the absence of UVC light (TACVD), the treated SWCNT sample (3.09 mg) consisted of 1.37±0.03 mg C=C carbon (44.3±1.2%, w/w), 1.43±0.03 mg residue (46.3±1.1%, w/w) and only 0.24±0.02 mg deposited C (7.8±0.8%, w/w) (remainder humidity). To confirm that Fe (derived from iron pentacarbonyl) is responsible for the increased residual fraction measured after the various treatments, we characterized the residue using XPS. For PICVD samples, the residual fraction was composed of 10.0±1.4% at. Fe, 58.8±1.7% at. O and 31.2±0.3% at. C (graphitic C). Conversion of the atomic % of Fe to wt% gives the value of 30.0±1.4 wt%. Given the weight of the residue for treated SWCNTs samples (determined via TGA characterization, 1.64±0.03 mg), we can therefore calculate that the PICVD process was responsible for the addition of 0.49±0.03 mg of Fe. In other words, PICVD leads to a total deposition of 0.78±0.07 mg of C and Fe over 60 min, or a total deposition rate of 0.013±0.001 mg/min. Considering 10.0±1.4% at. deposited Fe (30.0±1.4 wt%. Fe) in the case of TACVD, 0.43±0.03 mg of Fe is deposited on the samples after 60 min of treatment. Therefore, by taking the deposited mass of Fe (0.49±0.03 and 0.43±0.03 mg for PICVD and TACVD, repectively) and the related initial mass of analyzed samples (4.27 mg and and 3.09 mg of SWCNTs treated by PICVD and TACVD, respectively), 11.5% w/w of treated PICVD samples and 14% w/w of treated TACVD ones consist of Fe. This shows that TACVD leads to coatings with more Fe rather than PICVD (the main component in the residue), also in agreement with the XPS findings, as well as previous works by [205, 206].
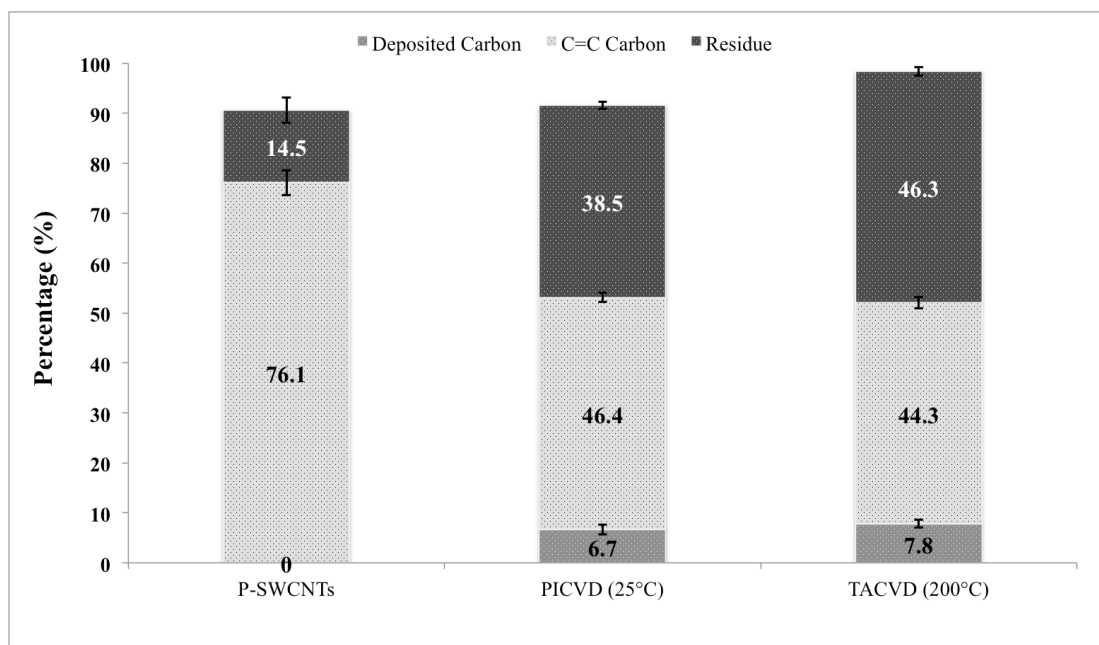
Figure 28. TGA characterization of P-SWCNT and SWCNTs treated by PICVD.

5.3.2 Gas-Phase Characterizations

5.3.2.1 Fourier Transform Infrared Spectroscopy

Having confirmed that measurable deposits form on the surface of SWCNTs, we investigated the reaction products to better understand the PICVD process by using an on-line FTIR system connected to the reactor outlet. Argon and H_2 were fed to the reactor as control samples, as they are not expected to show any IR absorption (UVC lamps were inactive) (Figure 29). When CO and H_2 are injected (UVC lamps inactive), the collected spectra showed two double peaks at wavenumbers of 2000/2050 cm^{-1} and 2100/2150 cm^{-1}, attributed to $Fe(CO)_5$ and CO, respectively [213] . The fourth spectrum corresponds to syngas injection when the UVC light is on. As expected given its known photodissociation, activating the UVC light causes a decrease in the intensity of the $Fe(CO)_5$ peak. Upon injection of H_2O_2 (as a photo-initiator (PI) [214]), the $Fe(CO)_5$ peak almost completely disappears - this can be explained by the reaction of the remaining $Fe(CO)_5$ with the hydroxyl (OH) radicals produced by photodissociation of H_2O_2 [215]. The FTIR results therefore corroborate consumption of $Fe(CO)_5$ under UVC light, and qualitatively show the effect of hydrogen peroxide during PICVD processing.
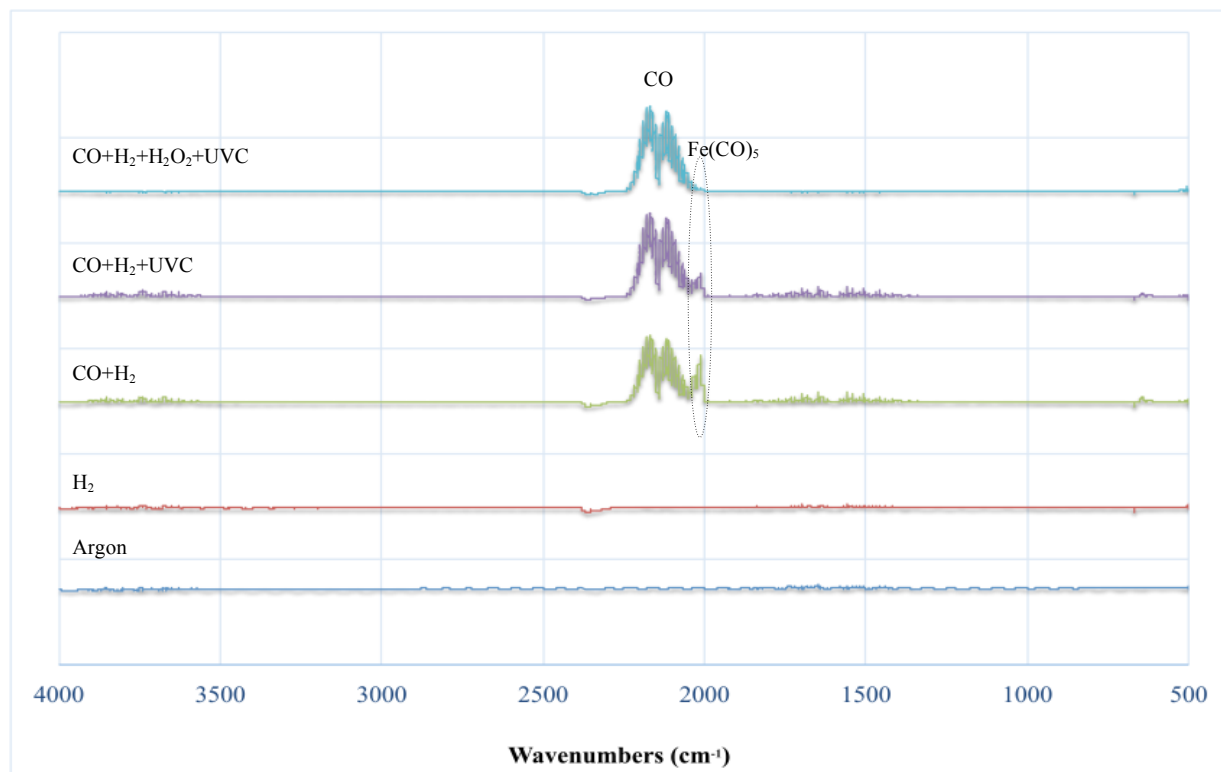
Figure 29. Online FTIR characterization of gaseous species at the PICVD reactor outlet. From bottom top, we present the outlet following the injection of Argon only, H_2 only, $CO+H_2$ (UVC lamp off) $CO+H_2$ (UVC lamp on), and finally $CO+H_2$ with H_2O_2 injection (UVC lamp on).

5.3.2.2 Gas Chromatography

Building upon the qualitative FTIR results, GC-MS was performed to identify and quantify the concentrations of chemical compounds at the inlet and outlet. Analysis at the PICVD reactor inlet (Figure B5A in supplementary results) identified CO and $Fe(CO)_5$ as the sole products (90% match in the GC-MS library). These compounds had retention times of 9.4 and 1.22 min, respectively, and were identified using their mass spectra (with peaks at $m/z = 56$, 84 and 112 for $Fe(CO)_5$ and 12, 16 and 28 for CO). The same compounds were detected at the reactor outlet (Figure B5B in supplementary results), but with different concentrations since the UVC lamp was on. To quantify the consumption of gas species during PICVD treatment, the GC-MS was calibrated for CO, CO_2 and $Fe(CO)_5$ with two different columns (HayeSep N and Molsieve 5A columns). The calibration for $Fe(CO)_5$ was performed at concentrations of 0.1, 0.5 and 100 ppm in toluene. For CO and CO_2 quantification, calibration was performed using calibrating gas cylinders at purities of 1, 10 and 99.99%. Each concentration was analyzed at least three times by

GC-MS to generate the calibration curves (see Figure B1, B6A and B6B in supplementary results). Based on this calibration, the initial concentration of $Fe(CO)_5$ and CO at the reactor inlet were 6.7±0.2 ppm and 75±2%, respectively (Figure 30A and 30B), when co-injecting CO, H_2 and H_2O_2. After a 20 min exposure to UVC light (with SWCNTs in the system), the concentrations of $Fe(CO)_5$ drops to 0.4±0.1 ppm, while CO remained relatively constant (any difference was below the detection limit of the instrument). In other words, 94±1% of the $Fe(CO)_5$ was consumed (which is reasonable given its strong absorption cross-section at the UVC lamps' peak emission [216]). When heating to 200 °C with UVC irradiation (also for 20 min), $Fe(CO)_5$ consumption did not change significantly (from 94±1% to 96±1%), in agreement with XPS results; CO also remains constant. If heating is applied independently (i.e. UVC lights remain off), the consumption of $Fe(CO)_5$ drops to 90±3% (i.e. final concentration of 0.7±0.2 ppm), with CO remaining unchanged (1h treatment time and total flow rate of 400 mL/min). Because GC-MS is unable to detect hydrogen, off-line micro GC was used. This analysis further serves to confirm the CO trends in GC-MS. At the inlet, CO and H_2 concentrations were 75±2% and 25±2%, respectively, while they were 75±2% and 25±2% at the outlet (Figure 30C). In other words, gas-phase analysis showed no measurable consumption of CO and H_2 during the PICVD process [99, 191, 192, 200]. Comparing the gas-phase characterizations with the previously described TGA results helps to clarify the roles of CO and H_2 and complete the mass balance. TGA analyses combined with XPS results showed that 0.49±0.20 mg of Fe and 0.29±0.04 mg of C were deposited onto the surface over the course of a 60 min PICVD treatment. Considering an inlet concentration of $Fe(CO)_5$ (6.7±0.2 ppm) in the CO stream (fed at 300 mL/min, the total number of moles over 60 min of treatment: 850 μmol, 18.5 kPa, 25 ºC), the iron pentacarbonyl alone can account for a maximum of 47.3±1.4 mg of Fe, 50.9±1.5 mg of C, and 67.8±2.0 mg of O deposited within the entire reactor over the course of a 60 min treatment (for every Fe atom present in the coating, 5 atoms of C and 5 atoms of O are deposited). Knowing that $Fe(CO)_5$ represents the sole source of Fe, and that 0.49±0.20 mg of Fe were deposited onto the SWCNT sample, this implies that approximately 1% of the inbound Fe is part of the coating. If we assume the same ratio applies to the C from $Fe(CO)_5$, then up to 0.53 mg of C could be traced back to that compound – this is greater than the amount of C actually deposited (0.29 mg), thus implying that $Fe(CO)_5$ is likely the sole source of C and Fe for deposition reaction and the CO fed to the reactor

does not participate in the reactions. Even with the margin for error on the Fe estimate (±0.23 mg), this remains true for the lowest value of Fe.

Based on these findings and previously discussed FTIR results, we can infer that $Fe(CO)_5$ and H_2O_2 are the sole active contributors to the reaction. In addition, measuring the weight of SWCNT buckypapers with a microbalance before and after treatment by PICVD revealed that 1.21 mg of coating was added to the surface over the 60 min reaction. Since 0.49 and 0.29 mg are already assigned to Fe and C, respectively, this leaves 0.43 mg for the O and H present on the surface. If we can assume that O deposits in the same ratio as C sourced from $Fe(CO)_5$ (0.57%) onto the SWCNT sample, we can account for 0.39 mg. The remainder (0.04 mg) is sourced from H_2O_2 – assuming a 1:1 atomic ratio, 0.003 mg are H and 0.04 mg is O. In other words, the final surface composition is 0.29 mg of C (24 wt%, 24 μmol), 0.43 mg of O (35 wt%, 27 μmol), 0.49 mg of Fe (40 wt%, 9 μmol), and 2.35 μg of H (0.2 wt%, 3 μmol). This corresponds to an approximate composition of $C_{38}H_5O_{43}Fe_{14}$. This bulk chemical formula is different from the one obtained through the near-surface analysis using XPS ($C_{21}O_{60}Fe_{19}$). The difference can be justified by a different structure of the bulk from the surface coating. It can be also assigned to the presence of unreacted radicals on the treated surfaces that can be oxidized upon the exposure to the air [97].

5.3.2.3 Concentration of $Fe(CO)_5$ Over Time

The mass balance used to confirm the role of CO in the mechanism also identifies that deposition occurs away from the SWCNT sample. This is apparent visually, as the quartz tube reactor become more opaque over time, which can be measured by light transmission through the tube (Figure 31 inset). The decreased amount of light also means that $Fe(CO)_5$ consumption decreases as a function of treatment time – the impact on $Fe(CO)_5$ concentration at the reactor outlet becomes significant for treatment times longer than 30 min (Figure 31). Therefore, reaction efficiency decreases over time during PICVD processing. It is interesting to note that there is no significant effect on $Fe(CO)_5$ decomposition for the first 20 min of treatment, despite a clear decrease in irradiance (Figure 31 inset) – this implies that $2x10^{-4}$ W/cm^2 is sufficient energy for the $Fe(CO)_5$ decomposition reaction to move forward.
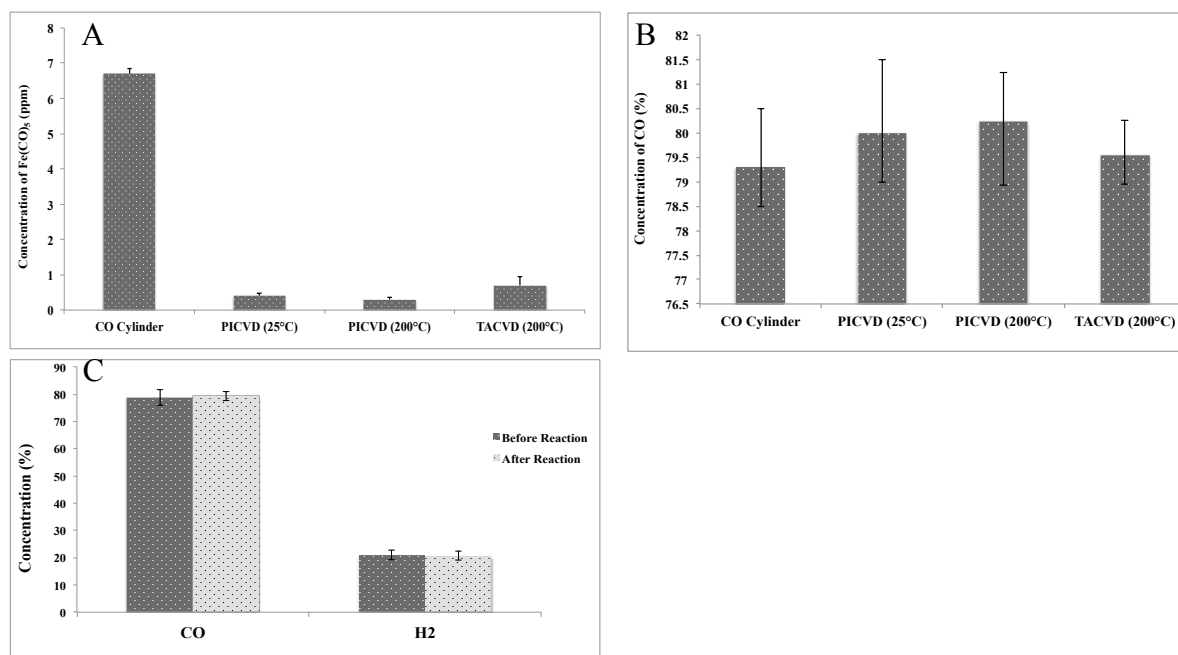
Figure 30.Measured concentrations of A) $Fe(CO)_5$ obtained from GC-MS, B) CO obtained from GC-MS , C) CO and H_2 obtained from micro GC.
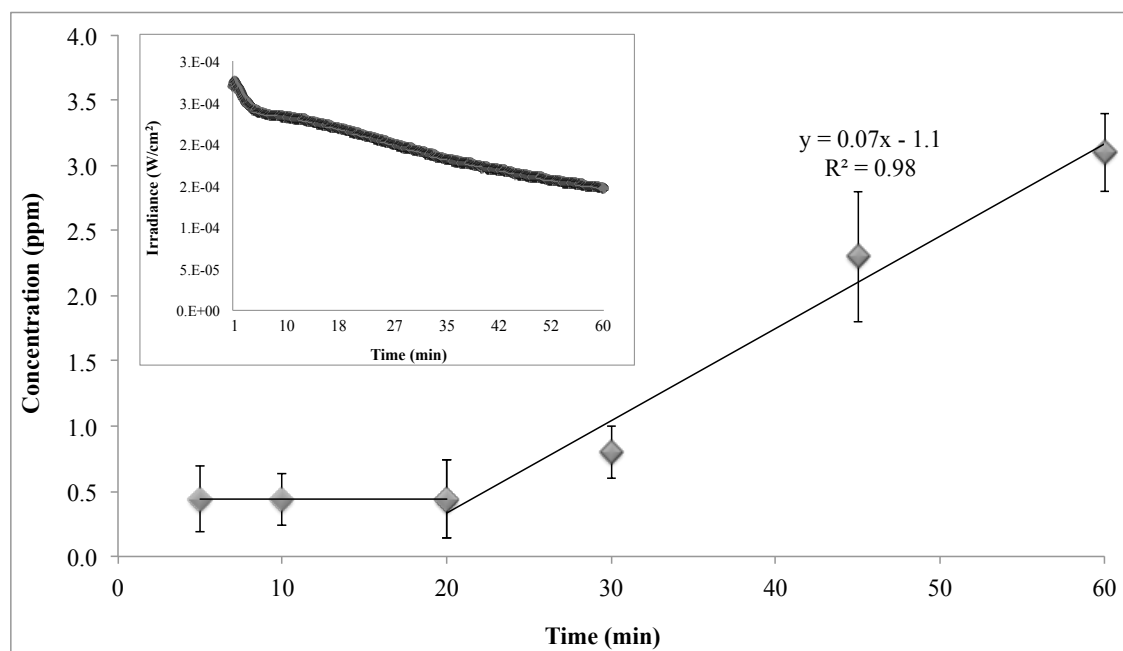
Figure 31. Concentration of $Fe(CO)_5$ at the reactor outlet shown in Y axis versus treatment time in X axis. Inset: measured irradiance of UVC light during the PICVD process [95].

5.3.3   Kinetic Model

The kinetic model and proposed mechanism for PICVD in this study include both gas-phase and surface reactions focused on the decomposition of $Fe(CO)_5$ and H_2O_2 as the main precursors (Tables 10 and 11).

5.3.3.1 Gas-phase Reactions

According to the GC analysis, 94±1% of $Fe(CO)_5$ is consumed during PICVD processing (20 min treatment), in agreement with this compound's high absorption cross-section in the 200 to 350 nm range (overlapping with the UVC lamps' major emission peak at 253.7 nm) [203]. As Seder et al. (1986) reported, the photo-dissociation pathway of this compound is sequential, from $Fe(CO)_4$ to $Fe(CO)_3$ and $Fe(CO)_2$ at 248 nm (very close to the present work, reactions G1-G3, Table 10) with corresponding reaction rate constants of $(3.5 \pm 0.9) \times 10^{10}$, $(1.3 \pm 0.2) \times 10^{13}$ and $(1.8 \pm 0.3) \times 10^{13}$ $cm^3/mol.s$ [204]. The dissociation energies for $Fe(CO)_5$, $Fe(CO)_4$, $Fe(CO)_3$, $Fe(CO)_2$ $Fe(CO)$, and Fe are reported to be around 56, 60, 91.5, 114.5 and 140 kcal/mol, respectively. A UVC light at 253.7 nm can provide energy equal to 112.5 kcal/mol [217, 218]. Therefore, except $Fe(CO)$ and Fe, all other intermediates ($Fe(CO)_5$, $Fe(CO)_4$, $Fe(CO)_3$, $Fe(CO)_2$) can be formed in the reactor (reactions G1-G3, Table 10) [217, 218]. However, the UVC lamp also emits a secondary peak at 185 nm, which carries a photon energy of 155 kcal/mol. Therefore, it is possible to produce both $Fe(CO)$ and Fe (Reactions G4 and G5, Table 10). Given H_2O_2's wide absorption range (180-340 nm), it can dissociate into two hydroxyl radicals ($OH^\bullet$) under UVC light (reaction G6, Table 10). According to the FTIR analysis, H_2O_2 injection increased $Fe(CO)_5$ consumption. This is evidence of the Fenton reaction, in which $OH^\bullet$ radicals (formed from dissociation of H_2O_2) and $Fe(CO)_5$ react to form $Fe^\bullet(CO)_2OH$ and $3CO$ (reaction G7, Table 10) . Formed $OH^\bullet$ can then react with H_2O_2 to form $HO_2^\bullet$ radical and H_2O (reaction G8, Table 10). Further, $Fe(CO)_2$ can also react with the $OH^\bullet$ radical to form $FeOH$ and $2CO$ (reaction G9, Table 10) [219]. $CO^\bullet$ and H_2 can participate in chain reactions (reaction G10, Table 10) to produce $HCO^\bullet$ and $H^\bullet$ radicals. Carboxylic acid groups can be created by reacting CO and H_2O_2 (reaction G11, Table 10). Fe-containing intermediates can collide with each other to produce various iron oxide components in the gas phase, which subsequently deposit on the surfaces inside the reactor (reaction G12, Table 10).

Table 10. Proposed gas phase reaction mechanism for PICVD (FeCO$_5$+H$_2$O$_2$).

Samples	Reactions	Ref.
	Decomposition of iron pentacarbonyl	
G1	$Fe(CO)_5 + hv \leftrightarrow Fe(CO)_4 + C\bullet O$	[204]
G2	$Fe(CO)_4 + hv \leftrightarrow Fe(CO)_3 + C\bullet O$	[204]
G3	$Fe(CO)_3 + hv \leftrightarrow Fe(CO)_2 + C\bullet O$	[204]
G4	$Fe(CO)_2 + hv \rightarrow Fe (CO) + C\bullet O$	[220]
G5	$Fe(CO) + hv \rightarrow Fe^* + C\dot{}O$	[220]
G6	$H_2O_2 + hv \rightarrow 2OH\dot{}$	[221]
	Free radical reactions	
G7	$Fe(CO)_5 + OH\dot{} \rightarrow Fe\dot{}(CO)_2OH + 3CO$	[216]
G8	$HO\dot{} + H_2O_2 \rightarrow HO_2\dot{} + H_2O$	[222]
G9	$Fe(CO)_2 + OH\dot{} \rightarrow FeOH + 2CO^*$	[221]
G10	$C\dot{}O + H_2 \rightarrow HC\dot{}O + H\dot{}$	[95]
G11	$C\dot{}O + H_2O_2 \rightarrow COOH^* + OH\dot{}$	[223]
G12	$Fe(CO)_2 + Fe(CO)_2 \rightarrow Fe_2(CO)_3 + C\dot{}O$	[224]

5.3.3.2 Surface Reactions

The surface reactions can be approximated as chemisorption and adsorption of the main gaseous species (H$_2$O$_2$, CO, Fe(CO)$_5$ and H$_2$) to the surface by passing through the boundary layer above the SWCNT substrate (reactions S1-S6, Table 11). Reaction S6 describes chemisorption of OH$\dot{}$ radicals which forms from the photo-dissociation of H$_2$O$_2$ in the gas phase participate in the radical chain reactions to form COOH and hydroxyl iron (Fe(OH)$_n$) derivatives through attachment to the free C/Fe sites on the surface (S20 and S29, Table 11). They also generate available free sites for the deposition of other reactive species via subsequent desorption of produced gases. After adsorption of reactive species and precursors, the mechanism continues by dissociation and excitation of adsorbed components (reactions S7 to S14, Table 11). We assume the same photo-dissociation of Fe(CO)$_5$ to Fe(CO)$_4$, Fe(CO)$_3$, Fe(CO)$_2$, Fe(CO) and Fe, sequentially, occur on the surface as in the gas phase (reactions S7-S11, Table 11). The reaction of Fe(CO)$_5$ and OH$\dot{}$ radicals (Fenton reaction) leads to Fe$\dot{}$ (CO)$_2$OH$_s$ and 3CO (reaction S12,

Table 11). $CO^{\bullet}$ radicals detached from $Fe(CO)_5$ can deposit on available Fe, oxygen and carbon sites [225-227]. $CO^{\bullet}$ radicals can react with H_2 to produce $CH_2^{\bullet}/CO_2$ and $HCO^{\bullet}/H^{\bullet}$ radicals (reaction S13 and S14, Table 11). $Fe(CO)_2$ colliding with reactive species under UVC light leads to excited Fe (Fe*, reaction S15). The recombination reactions (or propagation steps) occur on the surface and various Fe components, such as Fe_{II}, Fe_{III}, FeCO, $Fe(OH)_3$, and Fe_2O_3, can be formed according to reactions S15-S21 (Table 11). In the propagation reactions, various hydrocarbon and $H^{\bullet}$ radicals can be formed through reactions S22 to S24 (Table 11). Reactive hydrocarbon species are assumed to adsorb onto both free sites on the SWCNT surface, and onto already adsorbed C species [228]. CO_2 and H radical can be obtained through reaction 25 (Table 11) in which termination happens by reacting $CO^{\bullet}$ and $OH^{\bullet}$ radicals. The collision of reactive species with each other terminates chain reactions, leading to various products such as FeOH, H_2O, COOH, CO, H_2, etc. on or near the SWCNT surfaces (reactions S26 to S29, Table 11). Film growth can continue through reaction S30 to form olefins and by the overall reactions (S1-S30) leading to metal-organic compounds (Table 11).

5.4 Conclusions

In this study, we presented a kinetic model and reaction pathway for syngas PICVD based on both gas phase- and surface phase- characterizations. We also investigated the effect of temperature on PICVD as the main kinetic parameter for the first time and compared it with the results obtained from TACVD. The results showed that heat leads to a greater fraction of deposited Fe. While XPS results revealed the surface compositional structure of coating approximated as $C_{21}O_{60}Fe_{19}$ based on the atomic percentage (with mainly carboxylic, hydroxyl, $Fe(CO)_n$, and $Fe(OH)_n$ chemical moieties), TGA and gas-phase characterizations revealed a bulk coating structure of $C_{38}H_5O_{43}Fe_{14}$. A reaction scheme based on surface and gas phase reactions helps explain the appearance of the surface functional groups. GC-MS characterizations revealed the significant effect of $Fe(CO)_5$ in the photochemical reaction: 94% is consumed and it is a major contributor to the oligomeric coating, though H_2O_2 also contributes, but to a lesser extent (only 0.016% of the H_2O_2 feed is deposited on ther surface). This points to a processing opportunity: if iron pentacarbonyl concentration can be controlled, it will be possible to significantly reduce CO and H_2 consumption compared to what was previously thought.

Table 11. Proposed surface reaction mechanism for PICVD (FeCO$_5$+H$_2$O$_2$) (*s* refers to oxygen, iron, and carbon free sites).

Samples	Reactions	Ref.
Adsorption and Desorption		
S1	$Fe(CO)_5 + s \leftrightarrow Fe(CO)_{5s}$	*n/a*
S2	$C^{\bullet}O + s \leftrightarrow C^{\bullet}O_s$	*n/a*
S3	$Fe^{\bullet}(CO)_2 + s \leftrightarrow Fe^{\bullet}(CO)_{2s}$	*n/a*
S4	$(CO)_2FeOH + s \leftrightarrow (CO)_2FeOH_s$	*n/a*
S5	$Fe_2(CO)_3 + s \leftrightarrow Fe_2(CO)_{3s}$	*n/a*
S6	$OH^{\bullet} + s \leftrightarrow OH_s$	*n/a*
Initiation		
S7	$Fe(CO)_{5s} + hv \rightarrow Fe\,(CO)_{4s} + C^{\bullet}O$	*[204]*
S8	$Fe(CO)_{4s} + hv \rightarrow Fe\,(CO)_{3s} + C^{\bullet}O$	*[204]*
S9	$Fe(CO)_{3s} + hv \rightarrow Fe\,(CO)_{2s} + C^{\bullet}O$	*[204]*
S10	$Fe(CO)_{2s} + hv \rightarrow Fe\,(CO)_s + C^{\bullet}O$	*[220]*
S11	$Fe(CO)_s + hv \rightarrow Fe^*_s + C^{\bullet}O$	*[220]*
S12	$Fe(CO)_{5s} + OH \rightarrow Fe\bullet(CO)_2OH_s + 3C^{\bullet}O$	*[221]*
S13	$2C^{\bullet}O + H_2 \rightarrow C^{\bullet}H_{2s} + CO_2$	*[95]*
S14	$C^{\bullet}O_s + H_{2s} \rightarrow HC^{\bullet}O_s + H^{\bullet}$	*[95]*
Propagation		
S15	$Fe^{\bullet}(CO)_{2s} \rightarrow Fe_s + 2C^{\bullet}O$	*[224]*
S16	$Fe_s^{\bullet} + Fe^{\bullet}(CO) \rightarrow Fe^{II}{}_s{}^* + C^{\bullet}O$	*[224]*
S17	$Fe^{II}{}_s + Fe^{\bullet}(CO) \rightarrow Fe^{III}{}_s{}^* + C^{\bullet}O$	*[224]*
S18	$Fe^{II} + H_2O_2 \rightarrow Fe^{III} + OH^- + OH^{\bullet}$	*[229]*
S19	$Fe^{III} + H_2O_2 \rightarrow Fe^{II} + H^+ + HO_2^{\bullet}$	*[229]*
S20	$Fe^{III} + 3OH^{\bullet} \leftrightarrow Fe(OH)_{3s}{}^*$	*[230]*
S21	$2Fe(OH)_{3s} \rightarrow Fe_2O_{3s} + 3H_2O$	*[231]*
S22	$HC^{\bullet}O_s + H_2 \rightarrow H_2C^{\bullet}O_s + H^{\bullet}$	*[95]*
S23	$C^{\bullet}H_{2s} + H_2 \rightarrow C^{\bullet}H_{3s} + H^{\bullet}$	*[95]*
S24	$C^{\bullet}H_3 + 2C^{\bullet}O \rightarrow CH_3CO + C^{\bullet}O$	*[95]*
S25	$C^{\bullet}O_s + OH^{\bullet} \rightarrow CO_2 + H^{\bullet}$	*[95]*
Termination		
S26	$Fe^{\bullet}(CO)_2 + OH^{\bullet} \rightarrow FeOH + 2CO$	*[95]*
S27	$2\,H_s{}^* \rightarrow H_2 + 2s$	*[201]*
S28	$2\,OH^{\bullet}_s \rightarrow H_2O + s$	*[201]*
S29	$C^{\bullet}O_s + OH^{\bullet} \rightarrow COOH_s$	*[232]*
S30	$n(C^{\bullet}O) + 2n\,(H_2) \rightarrow C_nH_{2n+1} + nH_2O$	*[95]*

ACKNOWLEDGMENTS

CHAPTER 6   GENERAL DISCUSSION

Carbon nanotubes have gained significant interest in various applications considering their individual properties. Depending on the application, a different wettability property and functionality are suitable for them. For example, in the nanocomposite industry, CNTs have been used to reinforce mechanical and physical properties. Whereas raw SWCNTs are able to disperse in non-polar polymers, to be dispersed in polar ones, they must be functionalized. In the biotechnology and pharmaceutical industries, there are extensive studies focusing on either the compatibility or cytotoxicity of CNTs, many of which are in contradiction. Many of these contradictions stem from CNT properties, such as aspect ratio, size, functionalities, functionalization degree, and hydrophilicity or hydrophobicity as well as defective sites on their hexagonal surface structure. The interesting point is that many of these properties are caused by functionalization methods. For example, the functionalization of CNTs with wet chemistry leads to many defective sites on their hexagonal structure and uncontrolled surface energy, hydrophilicity, and functionality. Therefore, the demand for a new solvent-free, gas-phase treatment approach for SWCNTs, which can apply a range of wettability to the surface with the same functionality, is clear. Accordingly, PICVD has been chosen based on its advantages and disadvantages, as highlighted in the literature review. From an engineering point of view, treatment costs on an industrial scale should be reasonable. To keep precursor costs low, and to increase the processing versatility (to make both hydrophilic and hydrophobic surfaces), syngas has been chosen as the main precursor. Therefore, the first objective of this study stands on the evaluation of the syngas/PICVD ability to make a full range of wettability on the SWCNT surfaces followed by the successful optimization of effective operational parameters. To gain more insight into the syngas/PICVD process, the second objective of this project was to understand and investigate the kinetic parameters, reaction mechanism, and reaction rates of syngas/PICVD.

6.1 Proof of Concept: Applicability of Syngas/PICVD to Treat SWCNTs

In the first paper (Chapter 4), we introduced surface functionalities on SWCNT surfaces reproduced to a controlled functionalization degree. To see if it was successfully functionalized, we used various analysis techniques, such as XPS, TEM, and TGA. Survey XPS results showed a 53% increase in terms of oxygen content after treatment. HR-XPS was done to understand the

chemical structure of coatings. HR-XPS revealed that the coating structures mostly consist of C-C, C-OH, $Fe(OH)_3$, COOH, O=C-F-Fe, Fe_2O_3, Fe-O, and FeOOH. Quantitative TGA results proved that 19.5% C-C carbon and 20% residue is added to the SWCNT surfaces after treatment. The iron was coming from the $Fe(CO)_5$ source as an impurity in the CO tank.

TEM images revealed the morphology of syngas/PICVD coatings around the SWCNT bundles. Coatings were mostly deposited around a bundle of SWCNTs rather than individual ones. However, we did find SWCNTs treated individually. This is probably the most important challenge in the functionalization of SWCNTs using syngas/PICVD, where a bundle of aggregated SWCNTs is trapped by the coating. This problem was expected due to utilizing a plug flow reactor and SWCNTs in the form of bulky papers. However, we could clearly promote the dispersibility of SWCNTs in polar solutions.

In this work we investigated several operating parameters, such as flow rate, treatment time, the molar ratio of H_2/CO, pressure, the position of samples inside the reactor, the effect of UV light, and the concentration of PI. According to the results, we could introduce a vast range of wettability (from super-hydrophilic to super-hydrophobic) to the SWCNT surfaces. To monitor the surface wettability, we used contact angle measurements using a tensiometer and Raman spectroscopy. The surface energy of treated SWCNTs was approximated using the Owens-Went method based on wettability results and consequently plotted versus the aspect ratio of H_2/CO. Figure 32 shows an increasing wettability of SWCNTs as a function of the molar ratio of H_2/CO. Experimental data clearly showed (contact angle measurements) that changing the pressure and position of samples inside the reactor completely changed the surface wettability while the surface oxygen content did not substantially change. Therefore, the hypothesis is that the physical arrangement of functionalities affects the surface wettability of SWCNTs rather than the chemical attachment of oxygen-containing groups.
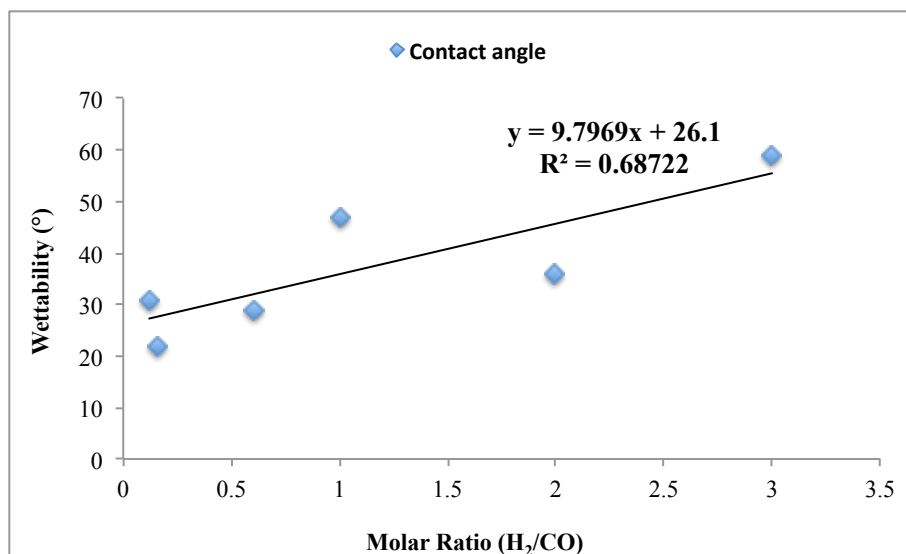
Figure 32. Wettability of SWCNTs in terms of molar ratio of H_2/CO.

Another effective parameter in the syngas/PICVD process was the use of hydrogen peroxide as a photo-initiator. In fact, hydrogen peroxide can easily decompose into two hydroxyl radicals ($OH^\bullet$) under UVC light. Short-lived hydroxyl radicals are highly reactive. This form of reactive oxygen is one of the most destructive forms, which can easily cause oxidation and peroxidation lipids and molecules. For the first time, Fenton showed that hydrogen peroxide, as the most available source of hydroxyl radicals, can be oxidized to $OH^\bullet$ with ferrous salts [233]. Oxygen molecules can get an electron from metal ions, including Fe^{2+} and Fe^{3+} and produce hydroxyl radicals. In the syngas/PICVD system, we have both Fe^{2+} and Fe^{3+} based on XPS characterizations. Therefore, oxidation and reduction reactions are taking place on the surface. It thus makes sense that by increasing the concentration of the PI (H_2O_2), more hydroxyl radicals are provided for the system and more functionality is expected to deposit on the SWCNT surfaces as shown in the XPS results. Survey XPS results showed up to 60% of oxygen is introduced on the SWCNTs surfaces.

6.2 Investigating Kinetic Parameters of Syngas/PICVD

Before this study, there was no information about the mass balance of syngas/PICVD and related gas-phase kinetic parameters that could demonstrate temperature was the most important

thermodynamic factor. Previous mechanisms of the reaction were suggested only based on surface characterizations while the mechanisms were mostly defined based on reaction syngas. In this study, by applying both gas- and surface-phase analysis, we could understand the effect of each precursor quantitatively. Doing many experiments with various CO cylinders presenting different concentrations led to a graph (Figure 33) in which XPS-identified functionalities (i.e., FeO, OH, CO, and COOH) were plotted versus the concentration of $Fe(CO)_5$. The results surprisingly showed that there were no functionalities on the SWCNT surfaces when the CO cylinder contained low $Fe(CO)_5$ concentration.
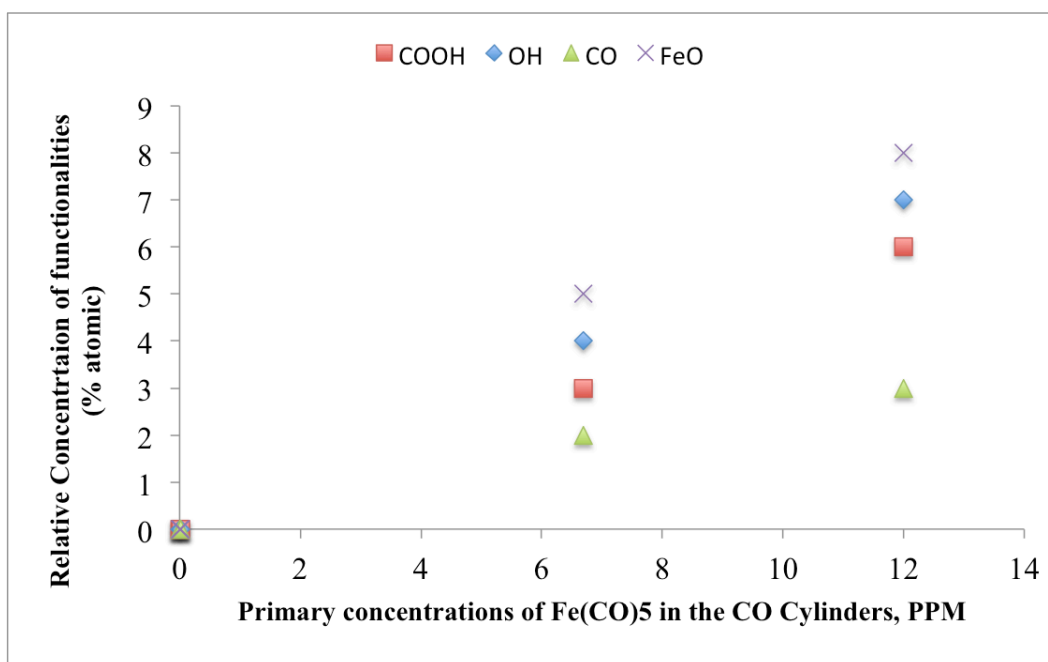
Figure 33. Syngas/PICVD treatment of SWCNTs with various CO cylinders showing different $Fe(CO)_5$ content.

Therefore, the main point of this graph is that CO does not contribute to the reaction and the key role is playing by $Fe(CO)_5$, a contaminant in CO cylinders. Considering its high absorption cross-section at the wavelength of 253.54 nm and low stability at atmospheric pressure and room temperature, significant consumption of this contaminant was expected along the reactor during the reaction. GC, GC-MS, and FTIR were the main gas-phase analytical methods and they revealed 94% consumption of this molecule during the treatment. In parallel with $Fe(CO)_5$ consumption, the introduction of the above-mentioned functionalities, such as CCOH and OH

groups, was observed on the SWCNT surfaces. The key role of $Fe(CO)_5$ in the syngas/PICVD as an initiator was evident.

The main point to discuss here is whether H_2O_2 is consumed in the PICVD reactor or not. FTIR results presented in Figure 29 clearly show that H_2O_2 is affecting the concentration of $Fe(CO)_5$. The Fenton reaction can be considered here in which the oxidation and reduction of iron are taking place inside the reactor in parallel (Equations 16 and 17).

$$Fe^{2+} + H_2O_2 \rightarrow Fe^{3+} + OH + OH^- \qquad \qquad \text{Equation 16}$$

$$Fe^{3+} + H_2O_2 \rightarrow Fe^{2+} + OOH + H^+ \qquad \qquad \text{Equation 17}$$

H_2O_2 has an appropriate absorption cross-section at the wavelength of 254.53 nm, showing this molecule can form two OH radicals upon being exposed to UV light. In this case, we can expect Fenton reactions, too. The challenging point in this study was that the gas-phase analysis did not show any consumption for CO and H_2. On the other hand, no deposition is formed using the CO cylinders with low concentration of $Fe(CO)_5$. Regarding the quantitative mass of deposited carbon and iron from TGA results along with the carbon mass balance calculations showing that $Fe(CO)_5$ could account for all the carbon deposited. Therefore, by sing a ppm concentration of $Fe(CO)_5$, 1 mL of H_2O_2it would be possible to obtain a similar coating. XPS analysis was used as a complementary characterization method to reveal the surface chemistry of coatings during this study. The XPS results showed the same surface mass percentage for the coating over time, $C_{21}O_{60}Fe_{19}$ whereas the bulk characterization showed a different coating structure, $C_{24}H_3O_{27}Fe_9$. Based on the mass balance calculations and characterizations, the coating should present a chemical structure as in Figure 34. Based on the study done by Farhanian et al. (2017), the film thickness growth is following a linear equation as Y=0.7t where Y and t are film thickness (nm) and treatment time (min), respectively. Accordingly, we expected to have a 42 nm coating thickness by applying a syngas/PICVD treatment for 1h (Figure 34).
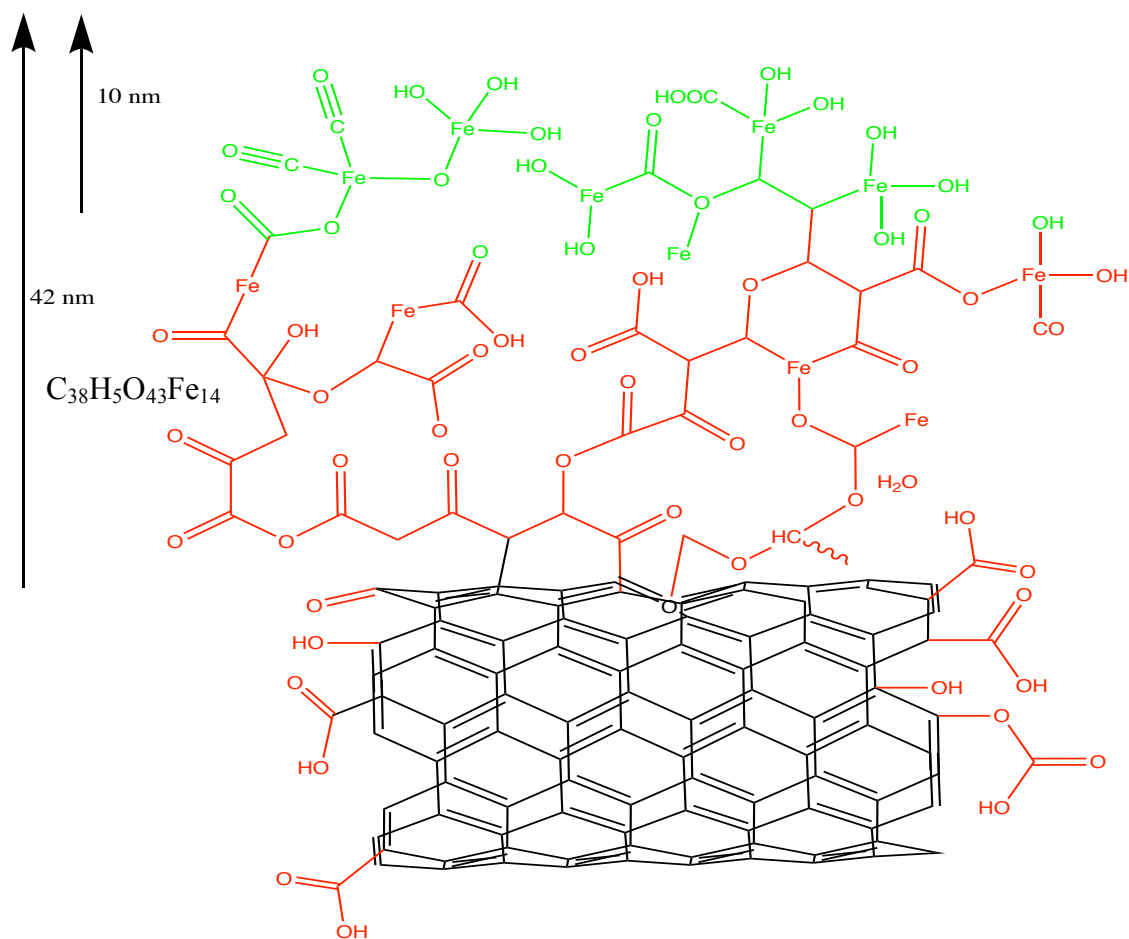
Figure 34. The structure of coatings on top of SWCNT samples deposited from syngas/PICVD treatments.

CHAPTER 7   CONCLUSION AND RECOMMENDATIONS

7.1   Conclusions

In this thesis, we investigated the treatment of SWCNTs by applying a simple, inexpensive, method: syngas/PICVD. In the first part of the study, we proved that syngas/PICVD is able to apply a full range of wettabilities of SWCNTs by changing the operating parameters. Apart from this, we obtained other key results listed in the following:

1) By increasing the ratio of H_2/CO, surface wettability (surface energy) increased possibly because of concentration of $Fe(CO)_5$.

2) The existence of Fe^{II}, Fe^{III}, COOH, OH, and CO bonded chemically to the coating surface on the treated SWCNTs.

3) Changing the pressure from slightly negative to positive as well as the position of substrate inside the reactor (from the beginning to the end of the reactor) leads to hydrophobic surfaces.

4) We tried to obtain the same range of wettability using the UV/ozone treatment. However, even after a few minutes, the surface would be super-hydrophilic.

5) TEM images indicated that the coating layer covered a bundle of SWCNTs rather than individual SWCNTs. However, we could detect individually treated SWCNTs.

6) XPS mapping of treated SWCNTs showed a uniform coating on the SWCNT surfaces.

In the second part of this research, we studied the kinetics and reaction mechanism of the syngas/PICVD process on the SWCNTs. The results highlighted the high impact of $Fe(CO)_5$ on the syngas/PICVD process while treatments with low $Fe(CO)_5$-content cylinders indicated no functionalities on the surface. In addition to 94% of $Fe(CO)_5$ H_2O_2 was consumed. In the first 20 minutes, $Fe(CO)_5$ was consumed linearly while the consumption started to decrease due to a yellowish-colored coating stuck to the reactor wall (led to intensity decrease). The other key parameters collected from this study are listed in the following:

1) Utilizing both gas- and surface- phase analysis revealed the structure of the coating on the SWCNT surfaces. The structure on the surface ($C_{21}O_{60}Fe_{19}$) is different from the bulk $C_{38}H_5O_{43}Fe_{14}$.

2) Treatment time does not affect the coating structure. It only allowed the coating thickness to grow.

3) Syngas/TACVD leads to coatings with a higher iron content.

4) The temperature did not significantly affect syngas/PICVD treatments.

7.2 Original contributions

This thesis led to several major scientific contributions listed below.

1) For the first time, it was demonstrated that SWCNTs could be treated in a full range of wettabilities by the same method and precursors in a controlled manner. The range started from $<5º$ up to $>150º$ and could be controlled by effective operating parameters. The previous studies reported a small wettability range or they used different precursors to obtain this range.

2) We can describe the kinetics and reaction mechanism of syngas/PICVD, including $Fe(CO)_5$ with both gas- and surface-phase characterizations. Previous works reported a reaction mechanism for syngas/PICVD based only on surface analysis while the role of $Fe(CO)_5$ was not included.

3) This study indicated the limited role of temperature in the syngas/PICVD process for the first time.

4) This study can provide insight regarding the mass balance of syngas/PICVD for the first time. We can now understand that no syngas is consumed during the process.

7.3 Recommendations

According to the obtained results in the present study, the following issues are recommended for future studies in three categories including short-term and long-term recommendations as well as potential projects:

7.3.1 Short-term recommendations

1) Obtaining the overall reaction rate/reaction rate constants related to the UV light intensity based on the Beer-Lambert law and simulating/modeling the syngas/PICVD process to predict its behavior at higher temperatures and various precursor concentrations.

2) Online monitoring of outlet gas and internal flow detection of the syngas/PICVD at different points along the reactor would be an interesting future work as it would provide valuable information regarding the reaction intermediates, their conversions, and effects on the final product of the syngas/PICVD reactor.

7.3.2 Long-term recommendations

1) Considering the obtained results, a huge amount of syngas is wasted during the process. I recommend redesigning the system using a lamp with higher energy or different precursors in the range of UV light.

2) Investigation of the syngas/PICVD behavior in the presence of nitrogen-containing photoinitiators/organic reagents to deposit amine groups.

7.4 Potential projects

1) The preliminary obtained results showed the possibility of enhancing mechanical properties of treated surfaces due to a cross-section network forming on the surface. It would be interesting to increase the mechanical properties of CNT bulky papers.

2) Based on XPS results, the total pressure of the syngas/PICVD reactor affects the electrical (and maybe thermal) conductivity of SWCNTs. Working under pressure made C1s XPS spectra start with a binding energy of 292 eV (a behavior like a nonconductive material) while working under vacuum made it start from the binding energy of 285 eV (like untreated SWCNTs which were electrically conductive). Therefore, the measurement of th eelectrical conductivity of treated SWCNTs by PICVD would be a potentially interesting project in the future.

3) Considering the unwanted existence of iron on the treated surface and key role of iron pentacarbonyl in the syngas/PICVD process, there will be a huge potential application for them in the bio-capturing membrane industry to kill E. coli bacteria.

BIBLIOGRAPHY

[1]   I. Fenoglio, M. Tomatis, D. Lison, J. Muller, A. Fonseca, J. B. Nagy, *et al.*, "Reactivity of carbon nanotubes: free radical generation or scavenging activity?," *Free Radic Biol Med,* vol. 40, pp. 1227-33, Apr 1 2006.

[2]   M. I. Keun Su Kim, Ali Shahverdi, Yasaman Alinejad, and Gervais Soucy, "Single-Walled Carbon Nanotubes Prepared by Large-Scale Induction Thermal Plasma Process: Synthesis, Characterization, and Purification," *J. Phys. Chem. C,* vol. 113, pp. 4340–4348, 2009,.

[3]   C. A. Dorval Dion and J. R. Tavares, "Photo-initiated chemical vapor deposition as a scalable particle functionalization technology (a practical review)," *Powder Technology,* vol. 239, pp. 484-491, 2013.

[4]   J. M. Makar and J. J. Beaudoin, "Carbon nanotubes and their application in the construction industry," in *1st International Symposium on Nanotechnology in Construction*, Paisley, Scotland, 2003, pp. pp. 331-341.

[5]   J. H. Du, J. Bai, and H. M. Cheng, "The present status and key problems of carbon nanotube based polymer composites," *Express Polymer Letters,* vol. 1, pp. 253-273, 2007.

[6]   P. D. Bradford and A. E. Bogdanovich, "Electrical Conductivity Study of Carbon Nanotube Yarns, 3-D Hybrid Braids and their Composites," *Journal of Composite Materials,* vol. 42, pp. 1533-1545, 2008.

[7]   E. T. Thostenson, Z. Ren, and T.-W. Chou, "Advances in the science and technology of carbon nanotubes and their composites: a review," *Composites Science and Technology,* vol. 61, pp. 1899–1912, 2001.

[8]   N. Kotagiri and J. W. Kim, "Stealth nanotubes: strategies of shielding carbon nanotubes to evade opsonization and improve biodistribution," *Int J Nanomedicine,* vol. 9 Suppl 1, pp. 85-105, 2014.

[9]   O. Zeni, R. Palumbo, R. Bernini, L. Zeni, M. Sarti, and M. R. Scarfi, "Cytotoxicity Investigation on Cultured Human Blood Cells Treated with Single-Wall Carbon Nanotubes," *Sensors,* vol. 8, pp. 488-499, 2008.

[10]   Y. Alinejad, N. Faucheux, and G. Soucy, "Preosteoblasts behavior in contact with single-walled carbon nanotubes synthesized by radio frequency induction thermal plasma using various catalysts," *J Appl Toxicol,* vol. 33, pp. 1143-55, Oct 2013.

[11]   C. B. Dong, A. S. Campell, R. Eldawud, G. Perhinschi, Y. Rojanasakul, and C. Z. Dinu, "Effects of acid treatment on structure, properties and biocompatibility of carbon nanotubes," *Applied Surface Science,* vol. 264, pp. 261-268, Jan 1 2013.

[12]   S. Vardharajula, S. Z. Ali, P. M. Tiwari, E. Eroglu, K. Vig, V. A. Dennis, *et al.*, "Functionalized carbon nanotubes: biomedical applications," *Int J Nanomedicine,* vol. 7, pp. 5361-74, 2012.

[13]   W. Lu and L. Dai, "Carbon Nanotube Supercapacitors," ed IntechOpen.

[14]   D. C. Vennerberg, R. L. Quirino, Y. Jang, and M. R. Kessler, "Oxidation behavior of multiwalled carbon nanotubes fluidized with ozone," *ACS Appl Mater Interfaces,* vol. 6, pp. 1835-42, Feb 12 2014.

[15]   M. Terrones, "Carbon nanotubes: synthesis and properties, electronic devices and other emerging applications," *International Materials Reviews,* vol. 49, pp. 325-377, 2013.

[16]   E. Andrzejewska, "Photopolymerization kinetics of multifunctional monomers," *Prog. Polym. Sci.,* vol. 26, pp. 605-665, May 2001.

[17]   S. M. Tabakman, K. Welsher, G. S. Hong, and H. J. Dai, "Optical Properties of Single-Walled Carbon Nanotubes Separated in a Density Gradient: Length, Bundling, and Aromatic Stacking Effects," *Journal of Physical Chemistry C,* vol. 114, pp. 19569-19575, Nov 25 2010.

[18]   P. A. Denis and F. Iribarne, "On the Applicability of Cluster Models to Study the Chemical Reactivity of Carbon Nanotubes," *Journal of Computational Chemistry,* vol. 32, pp. 2397-2403, Aug 2011.

[19]   M. C. Serrano, M. C. Gutiérrez, and F. del Monte, "Role of polymers in the design of 3D carbon nanotube-based scaffolds for biomedical applications," *Progress in Polymer Science,* vol. 39, pp. 1448-1471, 2014.

[20]   H. Kataura, Y. Kumazawa, Y. Maniwa, I. Umezu, S. Suzuki, Y. Ohtsuka*, et al.*, "Optical properties of single-wall carbon nanotubes," *Synthetic Metals,* vol. 103, pp. 2555-2558, Jun 1999.

[21]   J.-J. Liang, Y. Huang, F. Zhang, N. Li, Y.-F. Ma, F.-F. Li*, et al.*, "High microwave absorption performances for single-walled carbon nanotube—epoxy composites with ultra-low loadings," *Chinese Physics B,* vol. 23, p. 088802, 2014.

[22]   P. Newman, A. Minett, R. Ellis-Behnke, and H. Zreiqat, "Carbon nanotubes: their potential and pitfalls for bone tissue regeneration and engineering," *Nanomedicine,* vol. 9, pp. 1139-58, Nov 2013.

[23]   P.-X. Hou, C. Liu, and H.-M. Cheng, "Purification of carbon nanotubes," *Carbon,* vol. 46, pp. 2003-2025, 2008.

[24]   A. Eatemadi, H. Daraee, H. Karimkhanloo, M. Kouhi, N. Zarghami, A. Akbarzadeh*, et al.*, "Carbon nanotubes: properties, synthesis, purification, and medical applications," *Nanoscale Res Lett,* vol. 9, p. 393, 2014.

[25]   Teresa Mikolajczyk, Stanisław Rabiej, Grzegorz Szparaga, Maciej Boguń, Aneta Fraczek-Szczypta, and S. Błażewicz, "Strength Properties of Polyacrylonitrile (PAN) Fibres Modi ed with Carbon Nanotubes with Respect to Their Porous and Supramolecular Structure," *FIBRES & TEXTILES* vol. 17, 2009.

[26]   C. Journet, W. K. Maser, P. Bernier, A. Loiseau, M. L. delaChapelle, S. Lefrant*, et al.*, "Large-scale production of single-walled carbon nanotubes by the electric-arc technique," *Nature,* vol. 388, pp. 756-758, Aug 21 1997.

[27]   Z. Liu, Y. Liu, and D. Peng, "Hydroxylation of multi-walled carbon nanotubes reduces their cytotoxicity by limiting the activation of mitochondrial mediated apoptotic pathway," *J Mater Sci Mater Med,* vol. 25, pp. 1033-44, Apr 2014.

[28]   J. Prasek, J. Drbohlavova, J. Chomoucka, J. Hubalek, O. Jasek, V. Adam*, et al.*, "Methods for carbon nanotubes synthesis—review," *Journal of Materials Chemistry,* vol. 21, p. 15872, 2011.

[29]   N. Arora and N. N. Sharma, "Arc discharge synthesis of carbon nanotubes: Comprehensive review," *Diamond and Related Materials,* vol. 50, pp. 135-150, Nov 2014.

[30]   J. Chrzanowska, J. Hoffman, A. Małolepszy, M. Mazurkiewicz, T. A. Kowalewski, Z. Szymanski*, et al.*, "Synthesis of carbon nanotubes by the laser ablation method: Effect of laser wavelength," *physica status solidi (b),* vol. 252, pp. 1860-1867, 2015.

[31]   K. Koziol, B. O. Boskovic, and N. Yahya, "Synthesis of Carbon Nanostructures by CVD Method," vol. 5, pp. 23-49, 2010.

[32]   W. Zhou, L. Ding, and J. Liu, "Role of catalysts in the surface synthesis of single-walled carbon nanotubes," *Nano Research,* vol. 2, pp. 593-598, 2009.

[33] G. Lolli, L. Zhang, L. Balzano, N. Sakulchaicharoen, Y. Tan, and D. E. Resasco, "Tailoring (n,m) structure of single-walled carbon nanotubes by modifying reaction conditions and the nature of the support of CoMo catalysts," *J Phys Chem B,* vol. 110, pp. 2108-15, Feb 9 2006.

[34] S. Jalili, M. Jafari, and J. Habibian, "Effect of Impurity on Electronic Properties of Carbon Nanotubes," *Journal of the Iranian Chemical Society,* vol. 5, pp. 641-645, Dec 2008.

[35] S. Y. Madani, A. Mandel, and A. M. Seifalian, "A concise review of carbon nanotube's toxicology," *Nano Rev,* vol. 4, Dec 3 2013.

[36] M. Allegri, D. K. Perivoliotis, M. G. Bianchi, M. Chiu, A. Pagliaro, M. A. Koklioti*, et al.*, "Toxicity determinants of multi-walled carbon nanotubes: The relationship between functionalization and agglomeration," *Toxicol Rep,* vol. 3, pp. 230-243, 2016.

[37] Y. Zhu and W. Li, "Cytotoxicity of carbon nanotubes," *Science in China Series B: Chemistry,* vol. 51, pp. 1021-1029, 2008.

[38] M. A. Turgunov, J. O. Oh, and S. H. Yoon, "Surface Modification of Multiwall Carbon Nanotubes by Sulfuric Acid and Nitric Acid," pp. 22-25, 2014.

[39] P.-A. Tsai, H.-Y. Kuo, W.-M. Chiu, and J.-H. Wu, "Purification and Functionalization of Single-Walled Carbon Nanotubes through Different Treatment Procedures," *Journal of Nanomaterials,* vol. 2013, pp. 1-9, 2013.

[40] N. W. S. Kam, M. O'Connell, J. A. Wisdom, and H. J. Dai, "Carbon nanotubes as multifunctional biological transporters and near-infrared agents for selective cancer cell destruction," *Proceedings of the National Academy of Sciences of the United States of America,* vol. 102, pp. 11600-11605, Aug 16 2005.

[41] S. Lanone, P. Andujar, A. Kermanizadeh, and J. Boczkowski, "Determinants of carbon nanotube toxicity," *Adv Drug Deliv Rev,* vol. 65, pp. 2063-9, Dec 2013.

[42] T. R. Nayak, L. Jian, L. C. Phua, H. K. Ho, Y. P. Ren, and G. Pastorin, "Thin Films of Functionalized Multiwalled Carbon Nanotubes as Suitable Scaffold Materials for Stem Cells Proliferation and Bone Formation," *Acs Nano,* vol. 4, pp. 7717-7725, Dec 2010.

[43] M. VANDROVCOVÁ and L. BAČÁKOVÁ, "Adhesion, Growth and Differentiation of Osteoblasts on Surface- Modified Materials Developed for Bone Implants," *Physiol. Res.,* vol. 60, pp. 403-417, 2011.

[44] B. M. Abdallah and M. Kassem, "Human mesenchymal stem cells: from basic biology to clinical applications," *Gene Ther,* vol. 15, pp. 109-16, Jan 2008.

[45] M. Navarro, A. Michiardi, O. Castano, and J. A. Planell, "Biomaterials in orthopaedics," *J R Soc Interface,* vol. 5, pp. 1137-58, Oct 6 2008.

[46] M. Kalbacova, M. Kalbac, L. Dunsch, and U. Hempel, "Influence of single-walled carbon nanotube films on metabolic activity and adherence of human osteoblasts," *Carbon,* vol. 45, pp. 2266-2272, 2007.

[47] S.E. Hosseininasab, N. Faucheux, G. Soucy, and J.R. Tavares, "Surface Modification of Single-Wall Carbon Nanotubes (SWCNTs) by Photo- Initiated Chemical Vapor Deposition (PICVD) Using Syngas," in *TechConnect Briefs 2015*, 2015.

[48] E. T. Thostenson, Z. F. Ren, and T. W. Chou, "Advances in the science and technology of carbon nanotubes and their composites: a review," *Composites Science and Technology,* vol. 61, pp. 1899-1912, 2001.

[49] P. Supronowicz, K. Ullmann, P. Ajayan, B. Arulanandam, D. A.-N. Metzger, and R. Bizios, "ELECTRICAL STIMULATION PROMOTES OSTEOBLAST FUNCTIONS

PERTINENT TO OSTEOGENESIS," presented at the 47th Annual Meeting, Orthopaedic Research Society, San Francisco, California, 2001.

[50]   G U A N G J I A , H A I F A N G W A N G , L E I Y A N , X I A N G W A N G , R O N G J U A N P E I , T A O Y A N *, et al.*, "Cytotoxicity of carbon nanomaterials: single-wall nanotube, multi-wall nano- tube, and fullerene," *Environ. Sci. Technol.,* vol. 39, pp. 1378-1383, 2005.

[51]   D. Cui, F. Tian, C. S. Ozkan, M. Wang, and H. Gao, "Effect of single wall carbon nanotubes on human HEK293 cells," *Toxicol Lett,* vol. 155, pp. 73-85, Jan 15 2005.

[52]   A. O. Lobo, M. A. Corat, S. C. Ramos, J. T. Matsushima, A. E. Granato, C. Pacheco-Soares*, et al.*, "Fast preparation of hydroxyapatite/superhydrophilic vertically aligned multiwalled carbon nanotube composites for bioactive application," *Langmuir,* vol. 26, pp. 18308-14, Dec 7 2010.

[53]   A. O. Lobo, E. F. Antunes, M. B. Palma, C. Pacheco-Soares, V. J. Trava-Airoldi, and E. J. Corat, "Monolayer formation of human osteoblastic cells on vertically aligned multiwalled carbon nanotube scaffolds," *Cell Biol Int,* vol. 34, pp. 393-8, Mar 12 2010.

[54]   A. O. Lobo, E. F. Antunes, M. B. S. Palma, C. Pacheco-Soares, V. J. Trava-Airoldi, and E. J. Corat, "Biocompatibility of multi-walled carbon nanotubes grown on titanium and silicon surfaces," *Materials Science and Engineering: C,* vol. 28, pp. 532-538, 2008.

[55]   G. Jia, H. Wang, L. Yan, X. Wang, R. Pei, T. Yan*, et al.*, "Cytotoxicity of Carbon Nanomaterials: Single-Wall Nanotube, Multi-Wall Nanotube, and Fullerene," *Environmental Science & Technology,* vol. 39, pp. 1378-1383, 2005.

[56]   F. Tian, D. Cui, H. Schwarz, G. G. Estrada, and H. Kobayashi, "Cytotoxicity of single-wall carbon nanotubes on human fibroblasts," *Toxicol In Vitro,* vol. 20, pp. 1202-12, Oct 2006.

[57]   J. Wang, P. Sun, Y. Bao, J. Liu, and L. An, "Cytotoxicity of single-walled carbon nanotubes on PC12 cells," *Toxicol In Vitro,* vol. 25, pp. 242-50, Feb 2011.

[58]   Z. Liu, X. Dong, L. Song, H. Zhang, L. Liu, D. Zhu*, et al.*, "Carboxylation of multiwalled carbon nanotube enhanced its biocompatibility with L02 cells through decreased activation of mitochondrial apoptotic pathway," *J Biomed Mater Res A,* vol. 102, pp. 665-73, Mar 2014.

[59]   G. Vuković, A. Marinković, M. Obradović, V. Radmilović, M. Čolić, R. Aleksić*, et al.*, "Synthesis, characterization and cytotoxicity of surface amino-functionalized water-dispersible multi-walled carbon nanotubes," *Appl. Surf. Sci.,* vol. 255, pp. 8067-8075, 2009.

[60]   D. Liu, C. Yi, D. Zhang, J. Zhang, and M. Yang, "Inhibition of proliferation and differentiation of mesenchymal stem cells by carboxylated carbon nanotubes," *ACS Nano,* vol. 4, pp. 2185-95, Apr 27 2010.

[61]   S. L. Montes-Fonseca, E. Orrantia-Borunda, A. Aguilar-Elguezabal, C. Gonzalez Horta, P. Talamas-Rohana, and B. Sanchez-Ramirez, "Cytotoxicity of functionalized carbon nanotubes in J774A macrophages," *Nanomedicine,* vol. 8, pp. 853-9, Aug 2012.

[62]   R. A. MacDonald, B. F. Laurenzi, G. Viswanathan, P. M. Ajayan, and J. P. Stegemann, "Collagen-carbon nanotube composite materials as scaffolds in tissue engineering," *J Biomed Mater Res A,* vol. 74, pp. 489-96, Sep 1 2005.

[63]   Dandan Liu, Changqing Yi, Dawei Zhang, Jinchao Zhang, and Mengsu Yang, "Inhibition of Proliferation and Differentiation of Mesenchymal Stem Cells by Carboxylated Carbon Nanotubes<nn901479w.pdf>," *acsNANO,* vol. 4, pp. 2185–2195, 2010.

[64] M. Song, L. Zeng, S. Yuan, J. Yin, H. Wang, and G. Jiang, "Study of cytotoxic effects of single-walled carbon nanotubes functionalized with different chemical groups on human MCF7 cells," *Chemosphere,* vol. 92, pp. 576-82, Jul 2013.

[65] G. Vuković, A. Marinković, M. Obradović, V. Radmilović, M. Čolić, R. Aleksić*, et al.*, "Synthesis, characterization and cytotoxicity of surface amino-functionalized water-dispersible multi-walled carbon nanotubes," *Applied Surface Science,* vol. 255, pp. 8067-8075, 2009.

[66] M. Orecna, S. H. De Paoli, O. Janouskova, T. Z. Tegegn, M. Filipova, J. E. Bonevich*, et al.*, "Toxicity of carboxylated carbon nanotubes in endothelial cells is attenuated by stimulation of the autophagic flux with the release of nanomaterial in autophagic vesicles," *Nanomedicine,* vol. 10, pp. 939-48, Jul 2014.

[67] A. Hirsch, "Functionalization of single-walled carbon nanotubes," *Angew Chem Int Ed Engl,* vol. 41, pp. 1853-9, Jun 3 2002.

[68] D. M. Mattox. (2010). *Handbook of Physical Vapor Deposition (PVD) Processing.*

[69] T. Ramanathan, F. T. Fisher, R. S. Ruoff, and L. C. Brinson, "Amino-functionalized carbon nanotubes for binding to polymers and biological systems," *Chemistry of Materials,* vol. 17, pp. 1290-1295, Mar 22 2005.

[70] L. Y. Li, Y. Yang, G. L. Yang, X. M. Chen, B. S. Hsiao, B. Chu*, et al.*, "Patterning polyethylene oligomers on carbon nanotubes using physical vapor deposition," *Nano Letters,* vol. 6, pp. 1007-1012, May 2006.

[71] J. Y. Yook, J. Jun, and S. Kwak, "Amino functionalization of carbon nanotube surfaces with NH3 plasma treatment," *Applied Surface Science,* vol. 256, pp. 6941-6944, 2010.

[72] C. A. Dorval Dion, W. Raphael, E. Tong, and J. R. Tavares, "Photo-initiated chemical vapor deposition of thin films using syngas for the functionalization of surfaces at room temperature and near-atmospheric pressure," *Surface and Coatings Technology,* vol. 244, pp. 98-108, 2014.

[73] D. Farhanian, "Controlled functionalization of surfaces through syngas photo-initiated chemical vapor deposition," Philosophiae Doctor, Departement de genie chimique, École Polytechnique de Montreal, 2017.

[74] Q. Chen, L. Dai, M. Gao, S. Huang, and A. Mau, "Plasma Activation of Carbon Nanotubes for Chemical Modification," *J. Phys. Chem. B,* vol. 105, pp. 618-622, 2001.

[75] J. G. Jones, A. R. Waite, C. Muratore, and A. A. Voevodin, "Nitrogen and hydrogen plasma treatments of multiwalled carbon nanotubes," *Journal of Vacuum Science & Technology B: Microelectronics and Nanometer Structures,* vol. 26, p. 995, 2008.

[76] L. Vandsburger, E. J. Swanson, J. Tavares, J.-L. Meunier, and S. Coulombe, "Stabilized aqueous dispersion of multi-walled carbon nanotubes obtained by RF glow-discharge treatment," *Journal of Nanoparticle Research,* vol. 11, pp. 1817-1822, 2009.

[77] T. Xu, J. Yang, J. Liu, and Q. Fu, "Surface modification of multi-walled carbon nanotubes by O2 plasma," *Applied Surface Science,* vol. 253, pp. 8945-8951, 2007.

[78] Y. H. Yan, M. B. Chan-Park, Q. Zhou, C. M. Li, and C. Y. Yue, "Functionalization of carbon nanotubes by argon plasma-assisted ultraviolet grafting," *Applied Physics Letters,* vol. 87, p. 213101, 2005.

[79] D. Farhanian, " Controlled functionalization of surfaces through syngas photo-initiated chemical vapor deposition," Philosophiae Doctor, Departement de genie chimique, Chemical Engineering UNIVERSITÉ DE MONTRÉAL, 2017.

[80] M. Grujicic, G. Cao, A. M. Rao, T. M. Tritt, and S. Nayak, "UV-light enhanced oxidation of carbon nanotubes," *Applied Surface Science,* vol. 214, pp. 289-303, 2003.

[81] E. Najafi, J.-Y. Kim, S.-H. Han, and K. Shin, "UV-ozone treatment of multi-walled carbon nanotubes for enhanced organic solvent dispersion," *Colloids and Surfaces A: Physicochemical and Engineering Aspects,* vol. 284-285, pp. 373-378, 2006.

[82] J. K. Kim and M. L. Sham, "Functionalization of Carbon Nanotube Surface via UV/O$_3$ Treatment," *Solid State Phenomena,* vol. 121-123, pp. 1407-1410, 2007.

[83] M. Raja, "Surface Modification of Carbon Nanotubes with Combined UV and Ozone Treatments," *Fullerenes, Nanotubes and Carbon Nanostructures,* vol. 23, pp. 11-16, 2014.

[84] L. T. Cai, J. L. Bahr, Y. X. Yao, and J. M. Tour, "Ozonation of single-walled carbon nanotubes and their assemblies on rigid self-assembled monolayers," *Chemistry of Materials,* vol. 14, pp. 4235-4241, Oct 2002.

[85] P. L. Girard-Lauriault, R. Illgen, J. C. Ruiz, M. R. Wertheimer, and W. E. S. Unger, "Surface functionalization of graphite and carbon nanotubes by vacuum-ultraviolet photochemical reactions," *Appl. Surf. Sci.,* vol. 258, pp. 8448-8454, Sep 1 2012.

[86] E. Kasparek, J. R. Tavares, M. R. Wertheimer, and P.-L. Girard-Lauriault, "Sulfur-Rich Organic Films Deposited by Plasma- and Vacuum-Ultraviolet (VUV) Photo-Polymerization," *Plasma Process Polym,* pp. n/a-n/a, 2016.

[87] M. Raja, "Surface Modification of Carbon Nanotubes with Combined UV and Ozone Treatments," *Fuller Nanotub Car N,* vol. 23, pp. 11-16, 2014.

[88] J.-C. Ruiz, P.-L. Girard-Lauriault, F. Truica-Marasescu, and M. R. Wertheimer, "Plasma- and vacuum-ultraviolet (VUV) photo-polymerisation of N- and O-rich thin films," *Radiation Physics and Chemistry,* vol. 79, pp. 310-314, 2010.

[89] F. Truica-Marasescu, S. Pham, and M. R. Wertheimer, "VUV processing of polymers: Surface modification and deposition of organic thin films," *Nuclear Instruments and Methods in Physics Research Section B: Beam Interactions with Materials and Atoms,* vol. 265, pp. 31-36, 2007.

[90] E. Kasparek, J. R. Tavares, M. R. Wertheimer, and P.-L. Girard-Lauriault, "Sulfur-Rich Organic Films Deposited by Plasma- and Vacuum-Ultraviolet (VUV) Photo-Polymerization," *Plasma Processes and Polymers,* vol. 13, pp. 888-899, 2016.

[91] E. Kasparek, J. R. Tavares, M. R. Wertheimer, and P. L. Girard-Lauriault, "VUV Photodeposition of Thiol-Terminated Films: A Wavelength-Dependent Study," *Langmuir,* vol. 34, pp. 12234-12243, Oct 16 2018.

[92] T. Scherzer and U. Decker, "Kinetic investigations on UV-induced photopolymerization reactions by real-time FTIR-ATR spectroscopy: the e ciency of photoinitiators at 313 and 222 nm," *Nuclear Instruments and Methods in Physics Research B,* vol. 151, pp. 306-312, 1999.

[93] T. Scherzer, W. Knolle, S. Naumov, and R. Mehnert, "Direct initiation of the photopolymerization of acrylates by short-wavelength excimer UV radiation," *Nuclear Instruments & Methods in Physics Research Section B-Beam Interactions with Materials and Atoms,* vol. 208, pp. 271-276, Aug 2003.

[94] P.-L. Girard-Lauriault, R. Illgen, J.-C. Ruiz, M. R. Wertheimer, and W. E. S. Unger, "Surface functionalization of graphite and carbon nanotubes by vacuum-ultraviolet photochemical reactions," *Applied Surface Science,* vol. 258, pp. 8448-8454, 2012.

[95] D. Farhanian, G. De Crescenzo, and J. R. Tavares, "Kinetics, Chemistry, and Morphology of Syngas Photoinitiated Chemical Vapor Deposition," *Langmuir,* vol. 33, pp. 1780-1791, Feb 28 2017.

[96] H. Nasri Lari, D. Farhanian, D. C. Boffito, G. S. Patience, G. De Crescenzo, J. Chaouki, *et al.*, "Shedding light on iron pentacarbonyl photochemistry through a CVD case study," *Catalysis Communications,* vol. 100, pp. 19-23, 2017.

[97] E. Andrzejewska, "Photopolymerization kinetics of multifunctional monomers," *Progress in Polymer Science,* vol. 26, pp. 605-665, May 2001.

[98] T. Scherzer, "VUV-Induced Photopolymerization of Acrylates," *Macromolecular Chemistry and Physics,* vol. 213, pp. 324-334, 2012.

[99] C. A. Dorval Dion, W. Raphael, E. Tong, and J. R. Tavares, "Photo-initiated chemical vapor deposition of thin films using syngas for the functionalization of surfaces at room temperature and near-atmospheric pressure," *Surf. Coat. Technol.,* vol. 244, pp. 98-108, 2014.

[100] K. Balasubramanian and M. Burghard, "Chemically functionalized carbon nanotubes," *Small,* vol. 1, pp. 180-192, Feb 2005.

[101] K. L. Choy, "Chemical vapour deposition of coatings," *Prog. Mater Sci.,* vol. 48, pp. 57-170, 2003.

[102] Q. Chen, L. Dai, M. Gao, S. Huang, and A. Mau, "Plasma Activation of Carbon Nanotubes for Chemical Modification," *J. Phys. Chem.,* vol. 105, pp. 618-622, 2001.

[103] L. Vandsburger, E. J. Swanson, J. Tavares, J. L. Meunier, and S. Coulombe, "Stabilized aqueous dispersion of multi-walled carbon nanotubes obtained by RF glow-discharge treatment," *JNR,* vol. 11, pp. 1817-1822, Oct 2009.

[104] M. A. Behnajady, N. Modirshahla, and R. Hamzavi, "Kinetic study on photocatalytic degradation of C.I. Acid Yellow 23 by ZnO photocatalyst," *J Hazard Mater,* vol. 133, pp. 226-32, May 20 2006.

[105] U. Kogelschatza, H. Esromb, J.-Y. Zhangc, and I. W. Boyd, "High-intensity sources of incoherent UV and VUV excimer radiation for low-temperature materials processing," *Applied Surface Science,* vol. 168, pp. 29-36, 2000.

[106] W. Kowalski, *Ultraviolet Germicidal Irradiation Handbook*, 2009.

[107] Patrick Nuemberger, Daniel Wolper, Horst Weiss, and Gustav Gerber, "Femtosecond laser-assisted catalytic surface reactions of syngas and their optimization by tailored laser pulses," presented at the Ultrafast Phenomena XV: Proceedings of the 15th International Conference, Pacific Grove, USA, July 30 – August 4, 2006.

[108] H. J. Hageman, "Photoinitiators and photoinitiation mechanisms of free-radical polymerisation processes," ed: Photopoly- merization and photoimaging science and technology, London, New York: Elsevier, Applied Science,, 1989.

[109] E. Andrzejewska and M. Andrzejewski, "Polymerization Kinetics of Photocurable Acrylic Resins," *Journal of Polymer Science: Part A,* vol. 665–673, pp. 665–673, 1998.

[110] T. Y. Lee, C. A. Guymon, E. S. Jönsson, and C. E. Hoyle, "The effect of monomer structure on oxygen inhibition of (meth)acrylates photopolymerization," *Polymer,* vol. 45, pp. 6155-6162, 2004.

[111] Y. Yagci, S. Jockusch, and N. J. Turro, "Photoinitiated Polymerization: Advances, Challenges, and Opportunities," *Macromolecules,* vol. 43, pp. 6245-6260, 2010.

[112] I. Roppolo, A. Chiappone, K. Bejtka, E. Celasco, A. Chiodoni, F. Giorgis, *et al.*, "A powerful tool for graphene functionalization: Benzophenone mediated UV-grafting," *Carbon,* vol. 77, pp. 226-235, 2014.

[113] G. Colucci, A. Aluigi, C. Tonin, and R. Bongiovanni, "Photopolymerization of keratin-based thiol-ene coatings," *Progress in Organic Coatings,* vol. 77, pp. 1104-1110, 2014.

[114] A. K. O'Brien and C. N. Bowman, "Impact of Oxygen on Photopolymerization Kinetics and Polymer Structure," *Macromolecules,* vol. 39, pp. 2501-2506, 2006.

[115] W. F. Schroeder, S. L. Asmussen, W. D. Cook, and C. I. Vallo, "Efficiency of 4,4′-bis(N,N-diethylamino) benzophenone for the polymerization of dimethacrylate resins in thick sections," *Polymer International,* pp. n/a-n/a, 2011.

[116] N. S. Allen, *Photochemistry and Photophysics of Polymeric Materials*. John Wiley & Sons, 2010.

[117] D. S. Esen, N. Arsu, J. P. Da Silva, S. Jockusch, and N. J. Turro, "Benzoin type photoinitiator for free radical polymerization," *Journal of Polymer Science Part A: Polymer Chemistry,* vol. 51, pp. 1865-1871, 2013.

[118] P. Zhang and D. B. Henthorn, "Fabrication of pH- or temperature-responsive single wall carbon nanotubes via a graft from photopolymerization," *AIChE Journal,* vol. 58, pp. 2980-2986, 2012.

[119] A. Suresh, D. Anastasio, and D. D. Burkey, "Potential of Hexyl Acrylate Monomer as an Initiator in Photo-initiated CVD," *Chemical Vapor Deposition,* vol. 20, pp. 5-7, 2014.

[120] G. Bradley and R. S. Davidson, "Some aspects of the role of amines in the photoinitiated polymerisation of acrylates in the presence and absence of oxygen," *Recueil Des Travaux Chimiques Des Pays-Bas-Journal of the Royal Netherlands Chemical Society,* vol. 114, pp. 528-533, Nov-Dec 1995.

[121] R. S. Davidson, "The Role of Amines in UC Curing," in *Radiation Curing in Polymer Science abd Technology*. vol. 3, J. P. Fouassier, Ed., ed: Elsevier Science Publishers LTD, 1993.

[122] A. Voelkel, E. Andrzejewska, R. Maga, and M. Andrzejewski, "Examination of surfaces of solid polymers by inverse gas chromatography .1. Dispersive properties," *Polymer,* vol. 37, pp. 455-462, Feb 1996.

[123] E. Andrzejewska, "The Effect of Aliphatic Sulfides on the Photopolymerization of Diacrylates," *Polymer,* vol. 34, pp. 3899-3904, 1993.

[124] J. B. Guttenplan and S. G. Cohen, "Quenching and reduction of photoexcited benzophenone by thioethers and mercaptans," *The Journal of Organic Chemistry,* vol. 38, pp. 2001-2007, 1973.

[125] E. Andrzejewska, "Photopolymerization kinetics of multifunctional monomers," *Progress in Polymer Science,* vol. 26, p. 605±665, 2001.

[126] T. Y. Lee, C. A. Guymon, E. S. Jönsson, and C. E. Hoyle, "The effect of monomer structure on oxygen inhibition of (meth)acrylates photopolymerization," *Polymer,* vol. 45, pp. 6155-6162, 1/1/2004 2004.

[127] M. Höfer, N. Moszner, and R. Liska, "Oxygen scavengers and sensitizers for reduced oxygen inhibition in radical photopolymerization," *Journal of polymer science. Part A, Polymer chemistry,* 2008.

[128] A. Eitan, K. Jiang, D. Dukes, R. Andrews, and L. S. Schadler, "Surface Modification of Multiwalled Carbon Nanotubes: Toward the Tailoring of the Interface in Polymer Composites," *Chemistry of Materials,* vol. 15, pp. 3198-3201, 2003.

[129] G. R. TRYSON and A. R. SHULTZ, " A Calorimetric Study of Acrylate Photopolymerization," *Journal of Polymer Science,* vol. 17, pp. 2059-2075, 1979.

[130] F. H. R. Odont, C. F. Driscoll, and J. A. von Fraunhofer, "Effect of light source and time on the polymerization of resin cement through ceramic veneers," *Journal of Prosthodontics,* vol. 10, pp. 133-139, 2001.

[131] E. Mansfield, A. Kar, and S. A. Hooker, "Applications of TGA in quality control of SWCNTs," *Anal Bioanal Chem,* vol. 396, pp. 1071-7, Feb 2010.

[132] K. S. Kim, M. Imris, A. Shahverdi, Y. Alinejad, and G. Soucy, "Single-Walled Carbon Nanotubes Prepared by Large-Scale Induction Thermal Plasma Process: Synthesis, Characterization, and Purification," *Journal of Physical Chemistry C,* vol. 113, pp. 4340-4348, Mar 19 2009.

[133] Y. Matsuzawa, Y. Takada, T. Kodaira, H. Kihara, H. Kataura, and M. Yoshida, "Effective Nondestructive Purification of Single-Walled Carbon Nanotubes Based on High-Speed Centrifugation with a Photochemically Removable Dispersant," *The Journal of Physical Chemistry C,* vol. 118, pp. 5013-5019, 2014.

[134] P. Fardim and B. Holmbom, "ToF-SIMS imaging: a valuable chemical microscopy technique for paper and paper coatings," *Applied Surface Science,* vol. 249, pp. 393-407, Aug 15 2005.

[135] N. Vandencasteele and F. Reniers, "Plasma-modified polymer surfaces: Characterization using XPS," *Journal of Electron Spectroscopy and Related Phenomena,* vol. 178, pp. 394-408, May 2010.

[136] A. Paul, "Polymer functionalized single-walled carbon nanotube composites and semi-fluorinated quaternary ammonium polymer colloids and coatings," Doctor of Philosophy, Oklahoma State University, ProQuest Dissertations, 2012.

[137] M. AfzaliTabar, M. Alaei, R. R. Khojasteh, F. Motiee, and A. M. Rashidi, "Preference of multi-walled carbon nanotube (MWCNT) to single-walled carbon nanotube (SWCNT) and activated carbon for preparing silica nanohybrid pickering emulsion for chemical enhanced oil recovery (C-EOR)," *Journal of Solid State Chemistry,* vol. 245, pp. 164-173, Jan 2017.

[138] B. A. Kakade and V. K. Pillai, "Tuning the wetting properties of multiwalled carbon nanotubes by surface functionalization," *Journal of Physical Chemistry C,* vol. 112, pp. 3183-3186, Mar 6 2008.

[139] K. K. S. Lau, J. Bico, K. B. K. Teo, M. Chhowalla, G. A. J. Amaratunga, W. I. Milne*, et al.*, "Superhydrophobic carbon nanotube forests," *Nano Letters,* vol. 3, pp. 1701-1705, Dec 2003.

[140] Q. X. Li, J. S. Church, M. Naebe, and B. L. Fox, "Interfacial characterization and reinforcing mechanism of novel carbon nanotube - Carbon fibre hybrid composites," *Carbon,* vol. 109, pp. 74-86, Nov 2016.

[141] S. Hosseininasab, N. Faucheux, G. Soucy, and J. R. Tavares, "Full range of wettability through surface modification of single-wall carbon nanotubes by photo-initiated chemical vapour deposition," *Chemical Engineering Journal,* vol. 325, pp. 101-113, 2017.

[142] K. Safarova, A. Dvorak, R. Kubinek, M. Vujtek, and A. Rek, "Usage of AFM, SEM and TEM for the research of carbon nanotubes," *Modern Research and Educational Topics in Microscopy,* 2007.

[143] Z. L. Wang, "Transmission electron microscopy of shape-controlled nanocrystals and their assemblies," *Journal of Physical Chemistry B,* vol. 104, pp. 1153-1175, Feb 17 2000.

[144] J. P. Fouassier, X. Allonas, and D. Burget, "Photopolymerization reactions under visible lights: principle, mechanisms and examples of applications," *Progress in Organic Coatings,* vol. 47, pp. 16-36, 2003.

[145] C. L. X. Allonas, C. Bibaut, P. Jacques, J.P. Fouassier, "Investigation of the triplet quantum yield of thioxanthone by time-resolved thermal lens spectroscopy: solvent and population lens effects," *Chemical Physics Letters,* vol. 322, pp. 483–490, 2000.

[146] E. T. Thostenson, Z. F. Ren, and T. W. Chou, "Advances in the science and technology of carbon nanotubes and their composites: a review," *Compos. Sci. Technol.,* vol. 61, pp. 1899-1912, 2001.

[147] L. P. Zanello, B. Zhao, H. Hu, and R. C. Haddon, "Bone cell proliferation on carbon nanotubes," *Nano Lett,* vol. 6, pp. 562-7, Mar 2006.

[148] P. D. Bradford and A. E. Bogdanovich, "Electrical conductivity study of carbon nanotube yarns, 3-D hybrid braids and their composites," *J. Compos. Mater.,* vol. 42, pp. 1533-1545, Aug 2008.

[149] B. Kateb, M. Van Handel, L. Zhang, M. J. Bronikowski, H. Manohara, and B. Badie, "Internalization of MWCNTs by microglia: possible application in immunotherapy of brain tumors," *Neuroimage,* vol. 37 Suppl 1, pp. S9-17, 2007.

[150] N. Saito, Y. Usui, K. Aoki, N. Narita, M. Shimizu, N. Ogiwara*, et al.*, "Carbon nanotubes for biomaterials in contact with bone," *Curr Med Chem,* vol. 15, pp. 523-7, 2008.

[151] J. M. Wernik and S. A. Meguid, "Recent Developments in Multifunctional Nanocomposites Using Carbon Nanotubes," *Applied Mechanics Reviews,* vol. 63, p. 050801, Sep 2010.

[152] Y. Alinejad, N. Faucheux, and G. Soucy, "Preosteoblasts behavior in contact with single-walled carbon nanotubes synthesized by radio frequency induction thermal plasma using various catalysts," *J Appl Toxicol,* vol. 33, pp. 1143-1155, Oct 2013.

[153] B. Zhao, H. Hu, S. K. Mandal, and R. C. Haddon, "A bone mimic based on the self-assembly of hydroxyapatite on chemically functionalized single-walled carbon nanotubes," *Chem. Mater.,* vol. 17, pp. 3235-3241, Jun 14 2005.

[154] J. C. Ruiz, P. L. Girard-Lauriault, F. Truica-Marasescu, and M. R. Wertheimer, "Plasma- and vacuum-ultraviolet (VUV) photo-polymerisation of N- and O-rich thin films," *Radiat. Phys. Chem.,* vol. 79, pp. 310-314, Mar 2010.

[155] N. Ogihara, Y. Usui, K. Aoki, M. Shimizu, N. Narita, K. Hara*, et al.*, "Biocompatibility and bone tissue compatibility of alumina ceramics reinforced with carbon nanotubes," *Nanomedicine,* vol. 7, pp. 981-993, Jul 2012.

[156] S. Giannona, I. Firkowska, J. Rojas-Chapana, and M. Giersig, "Vertically aligned carbon nanotubes as cytocompatible material for enhanced adhesion and proliferation of osteoblast-like cells," *J. Nanosci. Nanotechnol.,* vol. 7, pp. 1679-1683, Apr-May 2007.

[157] Y. Wang, J. Wu, and F. Wei, "A treatment method to give separated multi-walled carbon nanotubes with high purity, high crystallization and a large aspect ratio," *Carbon,* vol. 41, pp. 2939-2948, 2003.

[158] J. Zhao, "Light Scattering Characterization of Carbon Nanotube Dispersions and Reinforcement of Polymer Composites," Doctor of Philosophy, Department of Chemical and Materials Engineering, University of Cincinnati, 2006.

[159] S. Z hang, T. Shao, S. S. Kaplan-Bekaroglu, and T. Karanfil, "The Impacts of Aggregation and Surface Chemistry of Carbon Nanotubes on the Adsorption of Synthetic Organic Compounds," *Environmental Science & Technology,* vol. 43, pp. 5719–5725, 2009.

[160] M. Foldvari and M. Bagonluri, "Carbon nanotubes as functional excipients for nanomedicines: II. Drug delivery and biocompatibility issues," *Nanomedicine,* vol. 4, pp. 183-200, Sep 2008.

[161] C. Ge, J. Du, L. Zhao, L. Wang, Y. Liu, D. Li, *et al.*, "Binding of blood proteins to carbon nanotubes reduces cytotoxicity," *Proc Natl Acad Sci U S A,* vol. 108, pp. 16968-73, Oct 11 2011.

[162] R. J. Chen, Y. Zhang, D. Wang, and H. Dai, "Noncovalent sidewall functionalization of single-walled carbon nanotubes for protein immobilization," *J Am Chem Soc,* vol. 123, pp. 3838-9, Apr 25 2001.

[163] Z. Rastian, A. A. Khodadadadi, F. Vahabzade, and Y. Mortazavi, "Functionalization of Multi -Walled Carbon Nanotubes for Lipase Immobilization," *JMTI,* vol. 1, pp. 54-71, 2013.

[164] A. H. Lu, E. L. Salabas, and F. Schuth, "Magnetic nanoparticles: synthesis, protection, functionalization, and application," *Angew Chem Int Ed Engl,* vol. 46, pp. 1222-44, 2007.

[165] C. A. Dorval Dion and J. R. Tavares, "Photo-initiated chemical vapor deposition as a scalable particle functionalization technology (a practical review)," *Powder Technol.,* vol. 239, pp. 484-491, 2013.

[166] H. Okabe, *Photochemistry of small molecules* vol. 431: Wiley New York, 1978.

[167] J. Y. Woo, D. Kim, J. Kim, J. Park, and C. S. Han, "Fast and Efficient Purification for Highly Conductive Transparent Carbon Nanotube Films," *Journal of Physical Chemistry C,* vol. 114, pp. 19169-19174, Nov 18 2010.

[168] E. P. Koumoulos and C. A. Charitidis, "Surface analysis and mechanical behaviour mapping of vertically aligned CNT forest array through nanoindentation," *Applied Surface Science,* vol. 396, pp. 681-687, Feb 28 2017.

[169] X. Liu, F. Xu, K. Zhang, B. Wei, Z. Gao, and Y. Qiu, "Characterization of enhanced interfacial bonding between epoxy and plasma functionalized carbon nanotube films," *Composites Science and Technology,* vol. 145, pp. 114-121, 2017.

[170] S. Min, J. Kim, C. Park, J.-H. Jin, and N. K. Min, "Long-term stability of superhydrophilic oxygen plasma-modified single-walled carbon nanotube network surfaces and the influence on ammonia gas detection," *Applied Surface Science,* vol. 410, pp. 105-110, 2017.

[171] M. Garzia Trulli, E. Sardella, F. Palumbo, G. Palazzo, L. C. Giannossa, A. Mangone, *et al.*, "Towards highly stable aqueous dispersions of multi-walled carbon nanotubes: the effect of oxygen plasma functionalization," *J Colloid Interface Sci,* vol. 491, pp. 255-264, Apr 01 2017.

[172] S. Wang, Y. Zhang, N. Abidi, and L. Cabrales, "Wettability and surface free energy of graphene films," *Langmuir,* vol. 25, pp. 11078-81, Sep 15 2009.

[173] R. Rajkhowa, A. Kafi, Q. T. Zhou, A. Kondor, D. A. V. Morton, and X. G. Wang, "Relationship between processing, surface energy and bulk properties of ultrafine silk particles," *Powder Technology,* vol. 270, pp. 112-120, Jan 2015.

[174] I. A. Sacui, R. C. Nieuwendaal, D. J. Burnett, S. J. Stranick, M. Jorfi, C. Weder, *et al.*, "Comparison of the properties of cellulose nanocrystals and cellulose nanofibrils isolated from bacteria, tunicate, and wood processed using acid, enzymatic, mechanical, and oxidative methods," *ACS Appl Mater Interfaces,* vol. 6, pp. 6127-38, May 14 2014.

[175] B. White, S. Banerjee, S. O'Brien, N. J. Turro, and I. P. Herman, "Zeta-potential measurements of surfactant-wrapped individual single-walled carbon nanotubes," *Journal of Physical Chemistry C,* vol. 111, pp. 13684-13690, Sep 20 2007.

[176] P. Bilalis, D. Katsigiannopoulos, A. Avgeropoulos, and G. Sakellariou, "Non-covalent functionalization of carbon nanotubes with polymers," *Rsc Advances,* vol. 4, pp. 2911-2934, 2014.

[177]   L. Chen, H. Xie, and W. Yu, "Functionalization Methods of Carbon Nanotubes and Its Applications," *Carbon Nanotubes Applications on Electron Devices,* 2011.

[178]   Y. L. Zhao and J. F. Stoddart, "Noncovalent functionalization of single-walled carbon nanotubes," *Acc Chem Res,* vol. 42, pp. 1161-71, Aug 18 2009.

[179]   D. Q. Yang and E. Sacher, "s-p hybridization in highly oriented pyrolytic graphite and its change on surface modification, as studied by X-ray photoelectron and Raman spectroscopies," *Surf. Sci.,* vol. 504, pp. 125-137, Apr 20 2002.

[180]   L. Yang, Y. W. Li, B. W. Sheldon, and T. J. Webster, "Altering surface energy of nanocrystalline diamond to control osteoblast responses," *J. Mater. Chem.,* vol. 22, pp. 205-214, 2012.

[181]   S. L. Rebelo, A. Guedes, M. E. Szefczyk, A. M. Pereira, J. P. Araujo, and C. Freire, "Progress in the Raman spectra analysis of covalently functionalized multiwalled carbon nanotubes: unraveling disorder in graphitic materials," *Phys Chem Chem Phys,* vol. 18, pp. 12784-96, May 14 2016.

[182]   H. Z. Wang, Z. P. Huang, Q. J. Cai, K. Kulkarni, C. L. Chen, D. Carnahan*, et al.*, "Reversible transformation of hydrophobicity and hydrophilicity of aligned carbon nanotube arrays and buckypapers by dry processes," *Carbon,* vol. 48, pp. 868-875, Mar 2010.

[183]   S. Banerjee and S. S. Wong, "Demonstration of diameter-selective reactivity in the sidewall ozonation of SWNTs by resonance Raman spectroscopy," *Nano Lett.,* vol. 4, pp. 1445-1450, Aug 2004.

[184]   S. Banerjee and S. S. Wong, "Rational sidewall functionalization and purification of single-walled carbon nanotubes by solution-phase ozonolysis," *J. Phys. Chem. B,* vol. 106, pp. 12144-12151, Nov 28 2002.

[185]   W. Wang, I. Ruiz, I. Lee, F. Zaera, M. Ozkan, and C. S. Ozkan, "Improved functionality of graphene and carbon nanotube hybrid foam architecture by UV-ozone treatment," *Nanoscale,* vol. 7, pp. 7045-50, Apr 28 2015.

[186]   N. Inagaki, *Plasma surface modification and plasma polymerization*: CRC Press, 1996.

[187]   A. Atkinson, "Mercury photosensitized reaction of tetrafluoroethylene," *Nature,* vol. 163, p. 291, Feb 19 1949.

[188]   J. Heicklen, V. Knight, and S. A. Greene, "Mercury-Photosensitized Oxidation of Tetrafluoroethylene," *J. Chem. Phys.,* vol. 42 p. 221, 1965.

[189]   J. Y. Tsao, "UV laser photopolymerization of volatile surface-adsorbed methyl methacrylate," *Appl. Phys. Lett.,* vol. 42, p. 997, 1983.

[190]   F. Truica-Marasescu, S. Pham, and M. R. Wertheimer, "VUV processing of polymers: Surface modification and deposition of organic thin films," *Nucl Instrum Methods Phys Res B,* vol. 265, pp. 31-36, Dec 2007.

[191]   V. Labonté, A. Marion, N. Virgilio, and J. R. Tavares, "Gas-Phase Surface Engineering of Polystyrene Beads Used to Challenge Automated Particle Inspection Systems," *Industrial & Engineering Chemistry Research,* vol. 55, pp. 7362-7372, 2016.

[192]   A. Berard, G. S. Patience, G. Chouinard, and J. R. Tavares, "Photo Initiated Chemical Vapour Deposition To Increase Polymer Hydrophobicity," *Sci Rep,* vol. 6, p. 31574, Aug 17 2016.

[193]   F. Vautard, S. Ozcan, F. Paulauskas, J. E. Spruiell, H. Meyer, and M. J. Lance, "Influence of the carbon fiber surface microstructure on the surface chemistry generated by a thermo-chemical surface treatment," *Appl. Surf. Sci.,* vol. 261, pp. 473-480, Nov 15 2012.

[194] D. V. Reha K. Tepe, Tracey Jacksier, Ramon M. Barnes, "Iron pentacarbonyl determination in carbon monoxide," *Spectrochimica Acta Part B* vol. 54, pp. 1861-1868, 1999.

[195] T. Susi, T. Pichler, and P. Ayala, "X-ray photoelectron spectroscopy of graphitic carbon nanomaterials doped with heteroatoms," *Beilstein J Nanotechnol,* vol. 6, pp. 177-92, 2015.

[196] F. Li, Y. Wang, D. Wang, and F. Wei, "Characterization of single-wall carbon nanotubes by N2 adsorption," *Carbon,* vol. 42, pp. 2375-2383, 2004.

[197] K. S. Kim, M. Imris, A. Shahverdi, Y. Alinejad, and G. Soucy, "Single-Walled Carbon Nanotubes Prepared by Large-Scale Induction Thermal Plasma Process: Synthesis, Characterization, and Purification," *J. Phys. Chem. C,* vol. 113, pp. 4340-4348, Mar 19 2009.

[198] O. Kanoun, C. Muller, A. Benchirouf, A. Sanli, T. N. Dinh, A. Al-Hamry*, et al.*, "Flexible carbon nanotube films for high performance strain sensors," *Sensors (Basel),* vol. 14, pp. 10042-71, 2014.

[199] J. M. Goddard and J. H. Hotchkiss, "Polymer surface modification for the attachment of bioactive compounds," *Prog. Polym. Sci.,* vol. 32, pp. 698-725, Jul 2007.

[200] S. Hosseininasab, N. Faucheux, G. Soucy, and J. R. Tavares, "Inducing a Full Range of Wettability through Surface Modification of Single-Wall Carbon Nanotubes by Photo-Initiated Chemical Vapor Deposition Using Syngas," *Chemical Engineering Journal,* vol. 325, pp. 101-113, 2017.

[201] N. K. Ingle, C. Theodoropoulos, T. J. Mountziaris, R. M. Wexler, and F. T. J. Smith, "Reaction kinetics and transport phenomena underlying the low-pressure metalorganic chemical vapor deposition of GaAs," *Journal of Crystal Growth,* vol. 167, pp. 543-556, 1996.

[202] T. C. Williams and C. R. Shaddix, "Contamination of Carbon Monoxide with Metal Carbonyls: Implications for Combustion Research," *Combustion Science and Technology,* vol. 179, pp. 1225-1230, 2007.

[203] M. Kotzian, N. Rosch, H. Schroder, and M. C. Zerner, "Optical-Spectra of Transition-Metal Carbonyls - Cr(Co)6, Fe(Co)5, and Ni(Co)4," *J. Am. Chem. Soc.,* vol. 111, pp. 7687-7696, Sep 27 1989.

[204] T. A. Seder, A. J. Ouderkirk, and E. Weitz, "The wavelength dependence of excimer laser photolysis of Fe(CO)5 in the gas phase. Transient infrared spectroscopy and kinetics of the Fe(CO)x (x=4,3,2) photofragments," *J. Chem. Phys.,* vol. 85, p. 1977, 1986.

[205] P. Wang, H. R. Li, and Z. W. Du, "Deposition of Iron on Graphite Felts by Thermal Decomposition of Fe(CO)(5) for Anodic Modification of Microbial Fuel Cells," *Int J Electrochem Sci,* vol. 8, pp. 4712-4722, Apr 2013.

[206] M. Fondell, F. Johansson, M. Gorgoi, L. von Fieandt, M. Boman, and A. Lindblad, "Phase control of iron oxides grown in nano-scale structures on FTO and Si(100): Hematite, maghemite and magnetite," *Vacuum,* vol. 117, pp. 85-90, Jul 2015.

[207] C. J. Lee, J. Park, Y. Huh, and J. Y. Lee, "Temperature effect on the growth of carbon nanotubes using thermal chemical vapor deposition," *Chem. Phys. Lett.,* vol. 343, pp. 33-38, Jul 27 2001.

[208] P. J. Linstrom and W. G. Mallard, "NIST Chemistry WebBook;," *NIST Standard Reference Database No. 69,* 2001.

[209] P. Mauron, C. Emmenegger, A. Zuttel, C. Nutzenadel, P. Sudan, and L. Schlapbach, "Synthesis of oriented nanotube films by chemical vapor deposition," *Carbon,* vol. 40, pp. 1339-1344, 2002.

[210] W. T. Leach, J. H. Zhu, and J. G. Ekerdt, "Thermal desorption effects in chemical vapor deposition of silicon nanoparticles," *Journal of Crystal Growth,* vol. 243, pp. 30-40, Aug 2002.

[211] M. Bystrzejewski, M. H. Rummeli, H. Lange, A. Huczko, P. Baranowski, T. Gemming*, et al.*, "Single-walled carbon nanotubes synthesis: a direct comparison of laser ablation and carbon arc routes," *J Nanosci Nanotechnol,* vol. 8, pp. 6178-86, Nov 2008.

[212] Y. Y. Wang, S. Gupta, and R. J. Nemanich, "Role of thin Fe catalyst in the synthesis of double- and single-wall carbon nanotubes via microwave chemical vapor deposition," *Appl. Phys. Lett.,* vol. 85, pp. 2601-2603, Sep 27 2004.

[213] R. K. Tepe, D. Vassallo, T. Jacksier, and R. M. Barnes, "Iron pentacarbonyl determination in carbon monoxide," *Spectrochim. Acta B,* vol. 54, p. 1861 1868, 1999.

[214] M. A. El-Sheikh, M. A. Ramadan, and A. El-Shafie, "Photo-oxidation of rice starch. Part I: Using hydrogen peroxide," *Carbohydrate Polymers,* vol. 80, pp. 266–269, 2010.

[215] M. Torrent, M. Sola, and G. Frenking, "Theoretical Study of Gas-Phase Reactions of Fe(CO)5 with OH- and Their Relevance for the Water Gas Shift Reaction," *Organometallics,* vol. 18, pp. 2801-2812, 1999.

[216] C. H. Liao and M. D. Gurol, "Chemical oxidation by photolytic decomposition of hydrogen peroxide," *Environ Sci Technol,* vol. 29, pp. 3007-14, Dec 1995.

[217] T. A. Seder, A. J. Ouderkirk, and E. Weitz, "The wavelength dependence of excimer laser photolysis of Fe(CO)5 in the gas phase. Transient infrared spectroscopy and kinetics of the Fe(CO)x (x=4,3,2) photofragments," *The Journal of Chemical Physics,* vol. 85, p. 1977, 1986.

[218] M. Poliakoff and E. Weitz, "Shedding light on organometallic reactions: the characterization of tetracarbonyliron (Fe(CO)4), a prototypical reaction intermediate," *Accounts of Chemical Research,* vol. 20, pp. 408-414, 2002.

[219] M. Castro, D. R. Salahub, and R. Fournier, "A density functional study of FeCO, FeCO−, and FeCO+," *J. Chem. Phys.,* vol. 100, pp. 8233-8239, 1994.

[220] F. D. Nasri H., Boffito D.C., Patience G.S., De Crescenzo G., Chaouki J., Tavares J.R., "Shedding Light on Iron Pentacarbonyl Photochemistry Through A CVD Case Study," *submitted to Chemical Communications,* 2016.

[221] Y. Chen, F. Zhang, C. Xu, J. Gao, D. Zhai, and Z. Zhao, "Theoretical investigation of water gas shift reaction catalyzed by iron group carbonyl complexes M(CO)5 (M = Fe, Ru, Os)," *J Phys Chem A,* vol. 116, pp. 2529-35, Mar 15 2012.

[222] J. J. Pignatello, E. Oliveros, and A. MacKay, "Advanced oxidation processes for organic contaminant destruction based on the Fenton reaction and related chemistry," *critical review: Environ. Sci. Technol,* vol. 36, pp. 1-84, 2006.

[223] P. Glarborg and P. Marshall, "The rate constant for the CO + H2O2 reaction," *Chem. Phys. Lett.,* vol. 475, pp. 40-43, Jun 16 2009.

[224] J. Z. Wen, C. F. Goldsmith, R. W. Ashcraft, and W. H. Green, "Detailed kinetic modeling of iron nanoparticle synthesis from the decomposition of Fe(CO)(5)," *J. Phys. Chem. C,* vol. 111, pp. 5677-5688, Apr 19 2007.

[225] A. M. Bradshaw and F. M. Hoffmann, "The chemisorption of carbon monoxide on palladium single crystal surfaces: IR spectroscopic evidence for localised site adsorption," *Surf. Sci.,* vol. 72, pp. 513-535, 1978.

[226] A. Linsebigler, G. Q. Lu, and J. T. Yates, "Co Chemisorption on Tio2(110) - Oxygen Vacancy Site Influence on Co Adsorption," *Journal of Chemical Physics,* vol. 103, pp. 9438-9443, Dec 1 1995.

[227] G. Brodén, G. Gafner, and H. P. Bonzel, "Co adsorption on potassium promoted Fe(110)," *Surf. Sci.,* vol. 84, pp. 295-314, 1979.

[228] B. Pan and B. Xing, "Adsorption mechanisms of organic chemicals on carbon nanotubes," *Environ Sci Technol,* vol. 42, pp. 9005-13, Dec 15 2008.

[229] M. González-Davila, J. M. Santana-Casiano, and F. J. Millero, "Oxidation of iron (II) nanomolar with H2O2 in seawater," *Geochimica et Cosmochimica Acta,* vol. 69, pp. 83-93, 2005.

[230] J. Majzlan, A. Navrotsky, and U. Schwertmann, "Thermodynamics of iron oxides: Part III. Enthalpies of formation and stability of ferrihydrite (~Fe(OH)3), schwertmannite (~FeO(OH)3/4(SO4)1/8), and ε-Fe2O3," *Geochimica et Cosmochimica Acta,* vol. 68, pp. 1049-1059, 2004.

[231] H. A. Moreno C., D. L. Cocke, J. A. G. Gomes, P. Morkovsky, J. R. Parga, E. Peterson*, et al.*, "Electrochemistry behind Electrocoagulation using Iron Electrodes," *ECS Transactions,* vol. 6, 2007.

[232] I. Kisacik, A. Stefanova, S. Ernst, and H. Baltruschat, "Oxidation of carbon monoxide, hydrogen peroxide and water at a boron doped diamond electrode: the competition for hydroxyl radicals," *Phys. Chem. Chem. Phys.,* vol. 15, pp. 4616-24, Apr 7 2013.

[233] Armin Saed-Moucheshi, Hassan Pakniyat, Hadi Pirasteh-Anosheh, and M. Azooz, "Role of ROS as Signaling Molecules in Plants," *Oxidative Damage to Plants,* pp. 585–620, 2014.

[234] X. L. Wang, H. Y. Hu, Q. Ye, T. T. Gao, F. Zhou, and Q. J. Xue, "Superamphiphobic coatings with coralline-like structure enabled by one-step spray of polyurethane/carbon nanotube composites," *J. Mater. Chem.,* vol. 22, pp. 9624-9631, 2012.

[235] M. Vandrovcova and L. Bacakova, "Adhesion, Growth and Differentiation of Osteoblasts on Surface- Modified Materials Developed for Bone Implants," *Physiol. Res.,* vol. 60, pp. 403-417, 2011.

[236] T.-J. Park, S. Banerjee, T. Hemraj-Benny, and S. S. Wong, "Purification strategies and purity visualization techniques for single-walled carbon nanotubes," *J. Mater. Chem.,* vol. 16, pp. 141-154, 2006.

[237] Z. Han and A. Fina, "Thermal conductivity of carbon nanotubes and their polymer nanocomposites: A review," *Progress in Polymer Science,* vol. 36, pp. 914-944, 2011.

[238] H. Zhang, C. H. Sun, F. Li, H. X. Li, and H. M. Cheng, "Purification of multiwalled carbon nanotubes by annealing and extraction based on the difference in van der Waals potential," *Journal of Physical Chemistry B,* vol. 110, pp. 9477-9481, May 18 2006.

[239] "99.9% purity multi-walled carbon nanotubes by vacuum high-temperature annealing."

[240] P. Rohringer, L. Shi, X. Liu, K. Yanagi, and T. Pichler, "Purification, separation and extraction of inner tubes from double-walled carbon nanotubes by tailoring density gradient ultracentrifugation using optical probes," *Carbon N Y,* vol. 74, pp. 282-290, Aug 2014.

[241] I. Pełech, K. Owodziń, and U. Narkiewicz, "Microwave-Assisted Acid Digestion Method for Purification of Carbon Nanotubes," *Fullerenes, Nanotubes and Carbon Nanostructures,* vol. 20, pp. 439-443, 2012.

[242] X. Xie, S. H. Jin, M. A. Wahab, A. E. Islam, C. Zhang, F. Du*, et al.*, "Microwave purification of large-area horizontally aligned arrays of single-walled carbon nanotubes," *Nat Commun,* vol. 5, p. 5332, Nov 12 2014.

[243] F.-H. Ko, C.-Y. Lee, C.-J. Ko, and T.-C. Chu, "Purification of multi-walled carbon nanotubes through microwave heating of nitric acid in a closed vessel," *Carbon,* vol. 43, pp. 727-733, 2005.

[244] S. Bandow, A. M. Rao, K. A. Williams, A. Thess, R. E. Smalley, and P. C. Eklund, "Purification of single-wall carbon nanotubes by microfiltration," *Journal of Physical Chemistry B,* vol. 101, pp. 8839-8842, Oct 30 1997.

[245] A. P. Yu, E. Bekyarova, M. E. Itkis, D. Fakhrutdinov, R. Webster, and R. C. Haddon, "Application of centrifugation to the large-scale purification of electric arc-produced single-walled carbon nanotubes," *Journal of the American Chemical Society,* vol. 128, pp. 9902-9908, Aug 2 2006.

[246] Y. Yang, L. Xie, Z. Chen, M. Liu, T. Zhu, and Z. Liu, "Purification and length separation of single-walled carbon nanotubes using chromatographic method," *Synthetic Metals,* vol. 155, pp. 455-460, 2005.

[247] N. Komatsu and F. Wang, "A Comprehensive Review on Separation Methods and Techniques for Single-Walled Carbon Nanotubes," *Materials (Basel),* vol. 3, pp. 3818-3844, Jun 30 2010.

[248] H. C. Shim, H. W. Lee, S. J. Yeom, Y. K. Kwak, S. S. Lee, and S. H. Kim, "Purification of Carbon Nanotubes through an Electric Field near a Microelectrode," *Journal of Physics: Conference Series,* vol. 61, pp. 1061-1065, 2007.

[249] S. K. Doorn, M. S. Strano, M. J. O'Connell, E. H. Haroz, K. L. Rialon, R. H. Hauge*, et al.*, "Capillary electrophoresis separations of bundled and individual carbon nanotubes," *Journal of Physical Chemistry B,* vol. 107, pp. 6063-6069, Jun 26 2003.

APPENDIX A – ARTICLE 1 SUPPLEMENTARY INFORMATION

Sample Preparation (Bucky papers)

15 mg of purified SWCNTs were dispersed in 10 mL of ethanol by bath sonication for 30 minutes (FS110, Fisher Scientific, power level of 135 W). 400 µL of dispersed SWCNTs were immediately deposited upon a glass substrate and placed in a vacuum oven for more than 3 h at a temperature of 100 °C to completely evaporate the ethanol.

Table A 1. Interfacial energy, dispersive and polar components of the liquids used for surface energy computations.

Liquids	γ_{sl} (mN/m)	γ_s^d (mN/m)	γ_s^p (mN/m)	Ref.
Deionized water	73±1	22±1	51	[234]
n-hexadecane	26±1	26±1	0±1	[234]

Table A 2. Blank experiments done based on glass substrates.

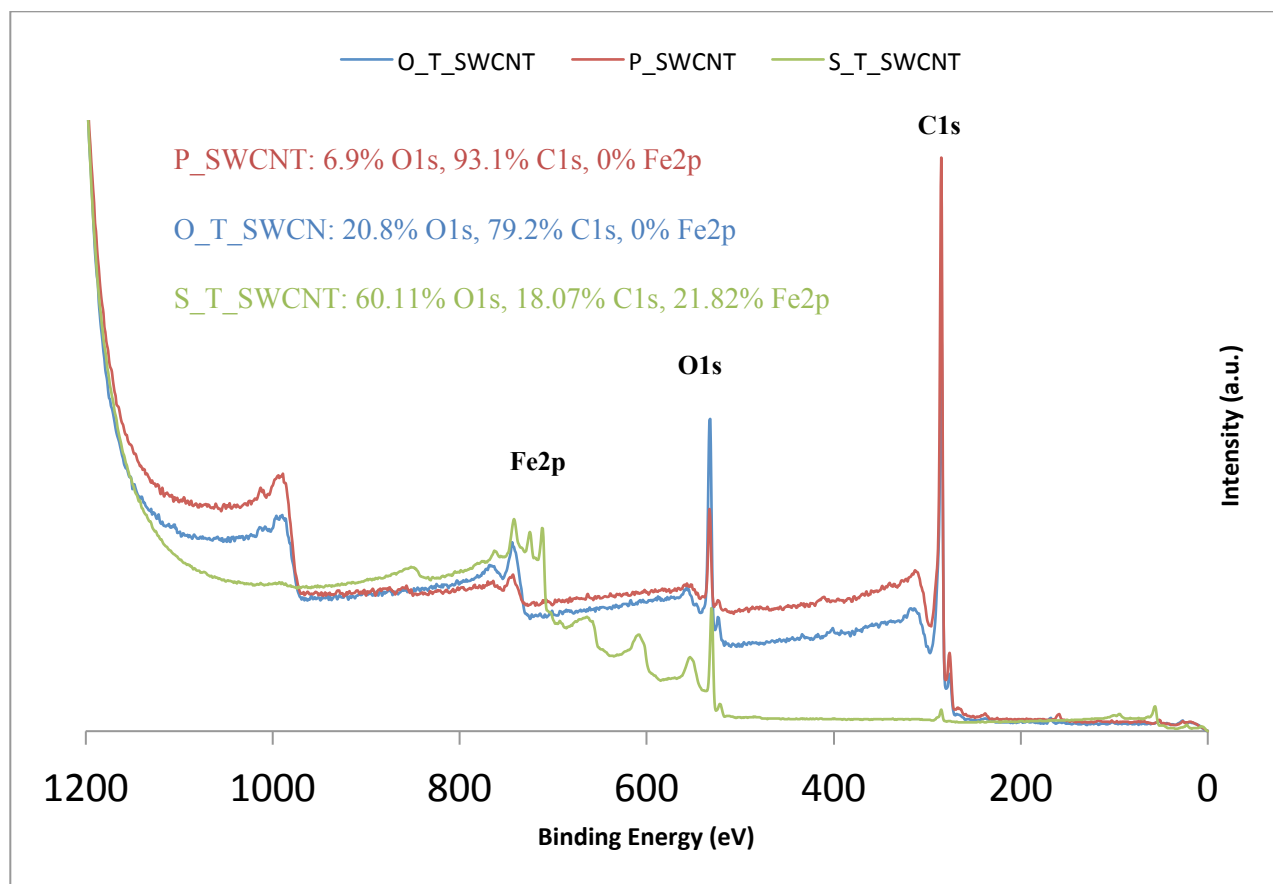| Conditions	Experimental conditions				
	Pressure (kPa)	Position (cm)	Treatment Time (min)	UV	Flow (ml/min)
Glass	n/a	n/a	n/a	n/a	n/a
CO+H$_2$+H$_2$O$_2$	0	50	120	Yes	350
CO+H$_2$	0	50	120	Yes	350
CO+H$_2$O$_2$+UV	0	50	120	Yes	350
H$_2$+H$_2$O$_2$+UV	0	50	120	Yes	350

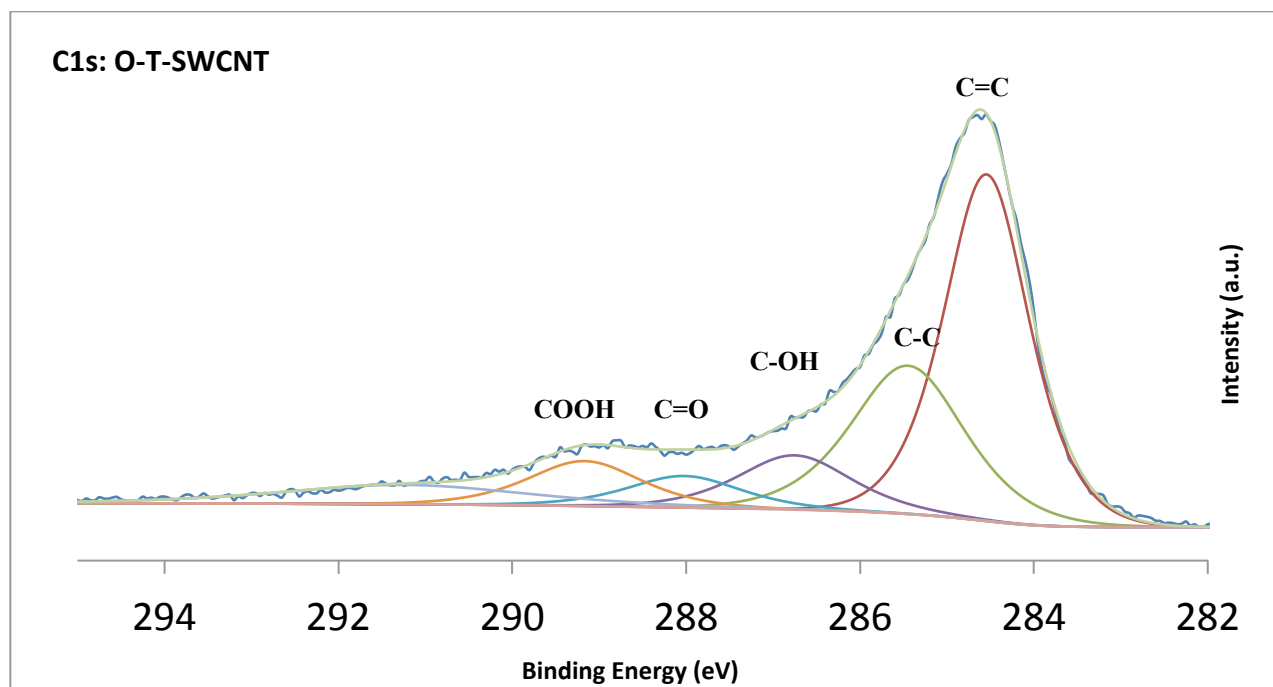Figure A 1. Survey peaks of S-T-SWCNT after treatment by PICVD.
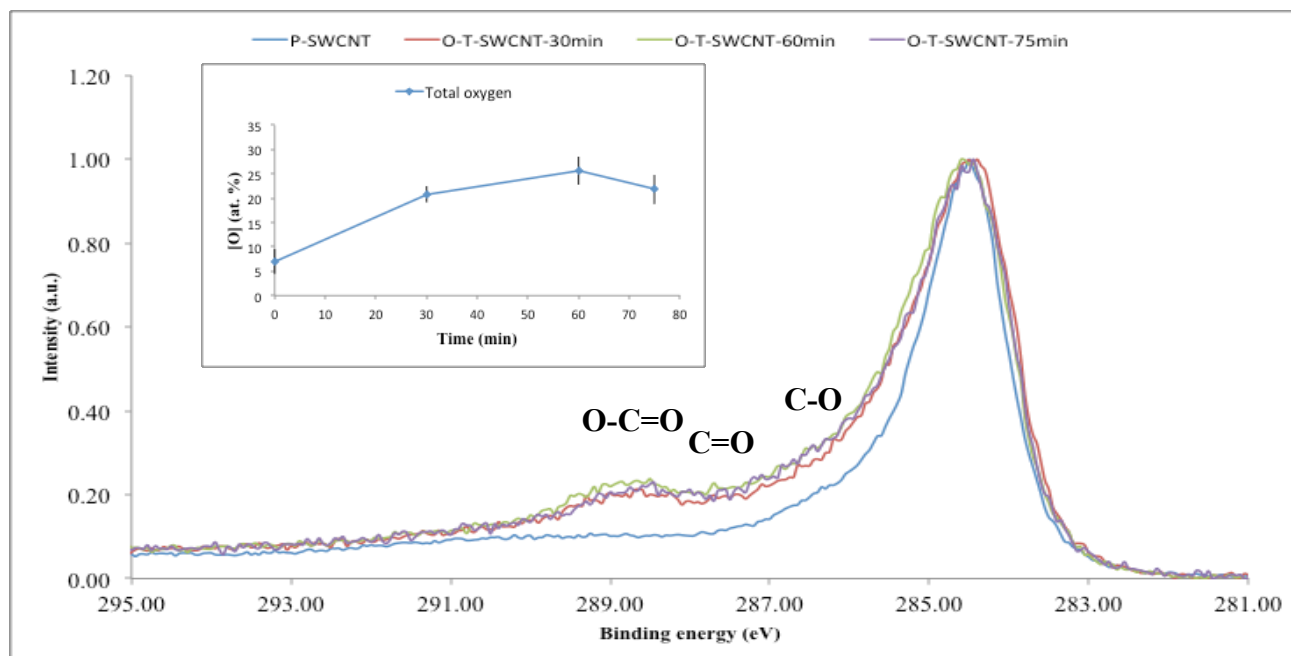
Figure A 2. High resolution XPS spectra of SWCNTs.

Figure A 3. A) Overlay of C1s XPS spectra, Blue line: ozone/UV treated for 30min, Violet line: ozone/UV SWCNTs treated for 60 min, Red line: P-SWCNTs, Green line: ozone/UV treated for 75 min, Inset: Evolution of survey XPS spectra for ozone/UV SWCNTs at different times (0, 30, 60 and 75 min). Error bars show standard deviation of three measurements.
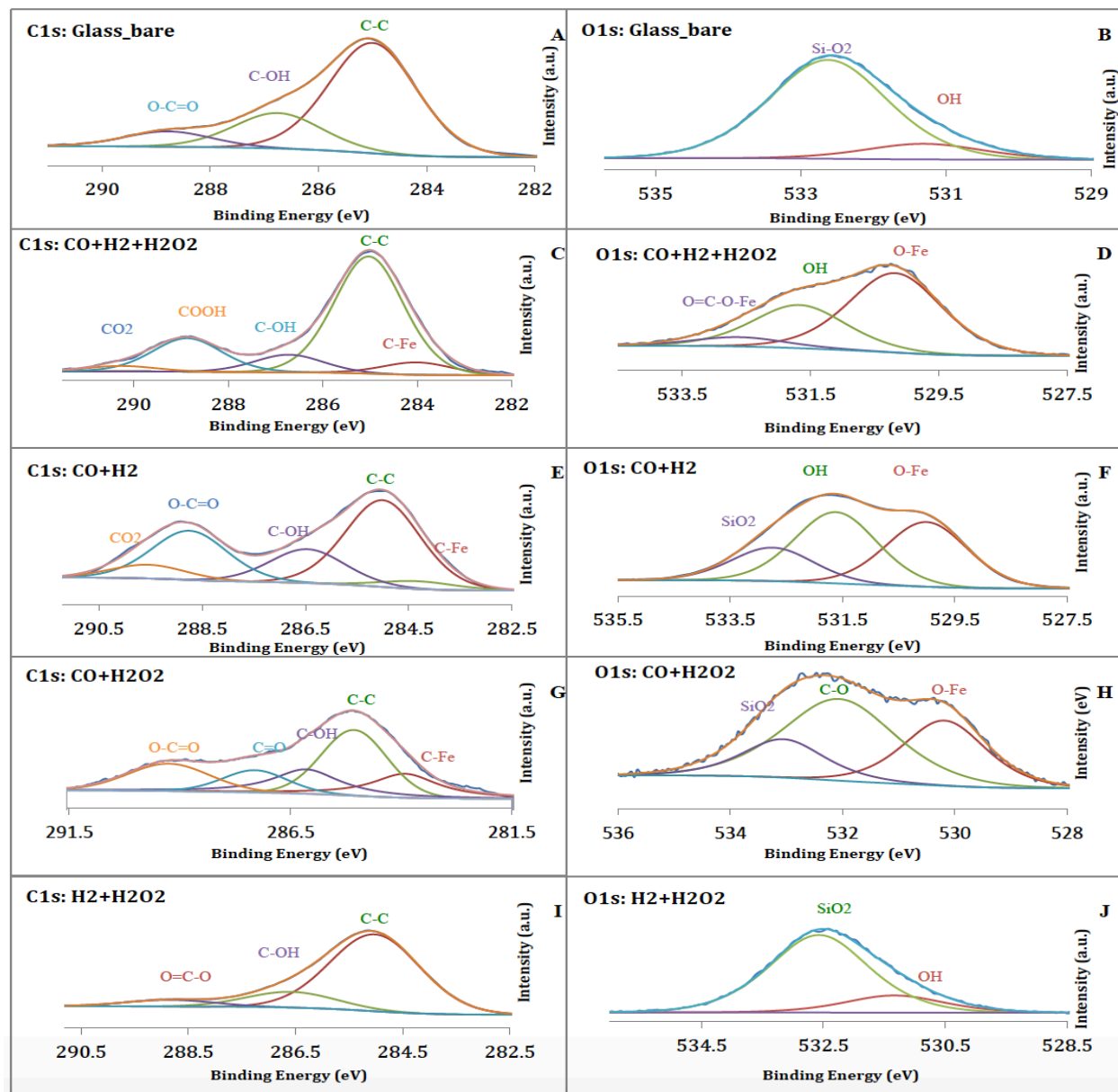
Figure A 4. A: High resolution C1s spectra of glass-bare; B: High resolution O1s spectra of glass-bare; C: High resolution C1s spectra of glass-CO+H_2+H_2O_2; D: High resolution O1s spectra of glass-CO+H_2+H_2O_2; E: High resolution C1s spectra of glass-CO+H_2; F: High resolution O1s spectra of glass-CO+H_2; G: High resolution C1s spectra of glass-CO+ H_2O_2; H: High resolution O1s spectra of glass-CO+H_2O_2; I: High resolution C1s spectra of glass-H_2+H_2O_2; J: High resolution O1s spectra of glass-H_2+H_2O_2.
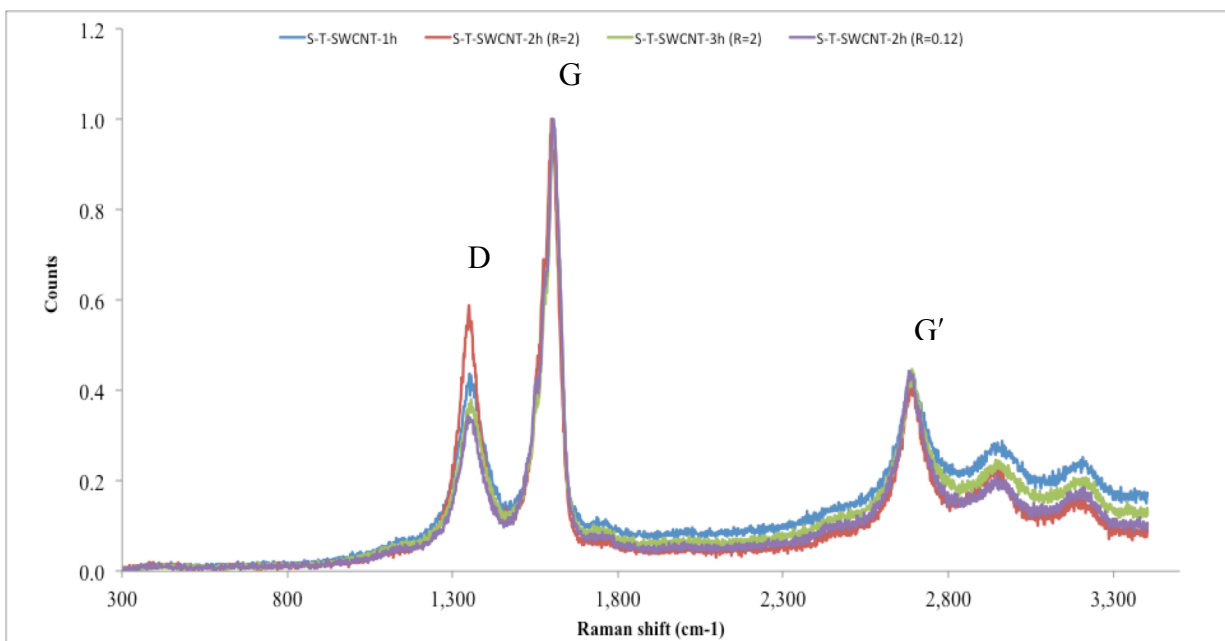
Figure A 5. Wide ranges of Raman spectra for the SWCNT materials Light Blue: P-SWCNTs, Violet: T-SWCNTs after 1h and molar ratio of 0.12, Green: T-SWCNTs after 2h and molar ratio of 0.12, Blue: T-SWCNTs after 3h and molar ratio of 0.12, Red: T-SWCNTs after 2h and the molar ratio of 2.
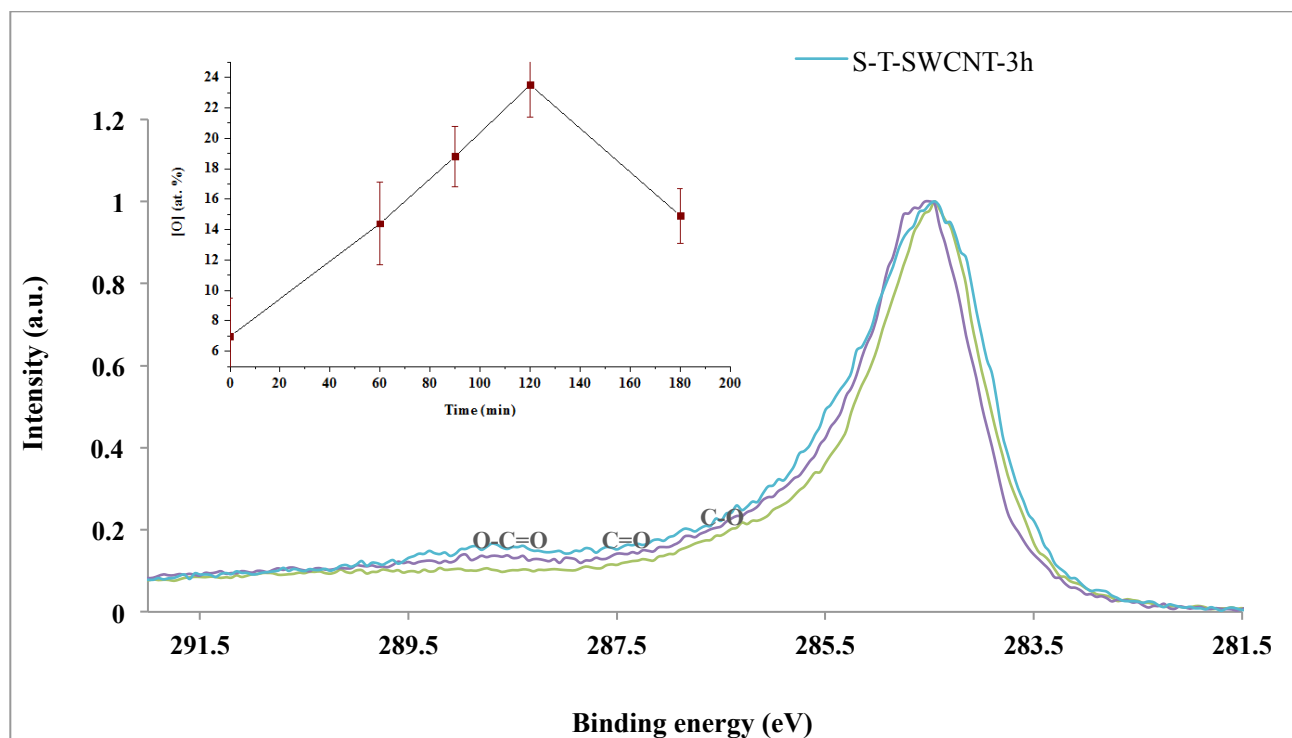
Figure A 6. Overlay of high-resolution C1s spectra of: Green color: P-SWCNT (Experiment 1), Violet color: S-T-SWCNTs treated for 2h (Experiment 11), Blue color: S-T-SWCNTs treated for 3h (Experiment 7). Inset: Evolution of survey XPS spectra for syngas/PICVD SWCNTs at different times (0, 60, 90, 120 and 180 min). Error bars show standard deviation of three measurements.
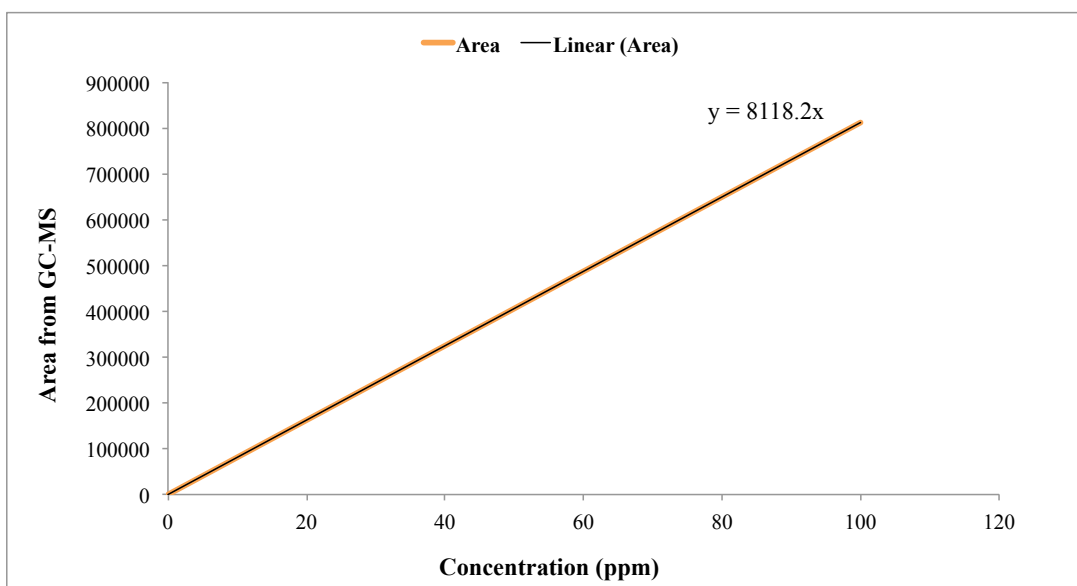
APPENDIX B – ARTICLE 2 SUPPLEMENTARY INFORMATION

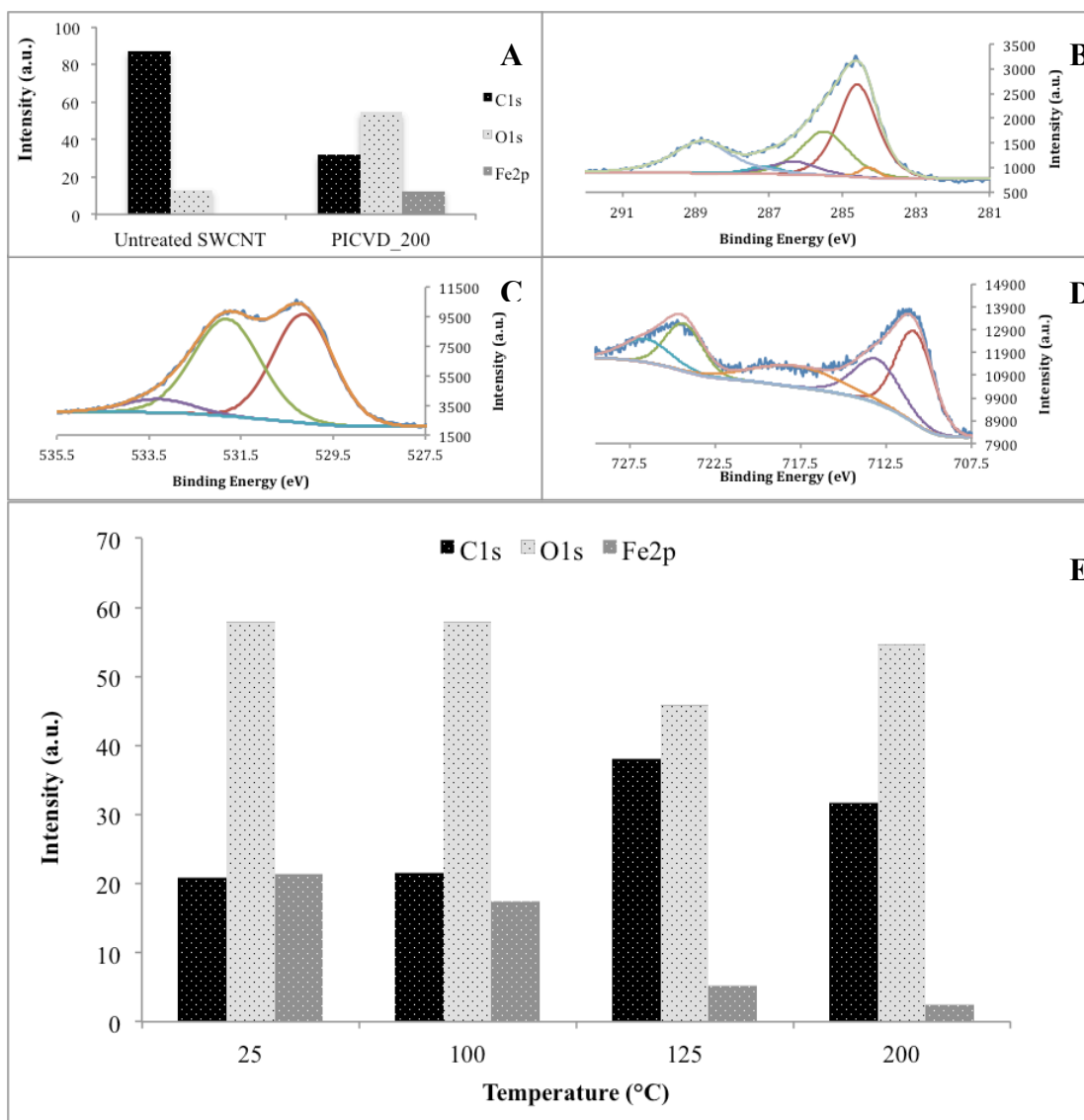Figure B 1. Calibration curve of $Fe(CO)_5$ performed at concentrations of 0.1, 0.5 and 100 ppm in toluene.

Figure B 2. A) Survey XPS spectra of treated SWCNT with syngas/PICVD_200 C, B) C1s HR-XPS of SWCNT treated with syngas/PICVD_200 C, C) O1s HR-XPS of SWCNT treated with syngas/PICVD_200 C, D) Fe2p HR-XPS of SWCNT treated with syngas/PICVD_200 C, E) Plotting of survey XPS spectra treated SWCNTs with syngas/PICVD over heat (the inset table is presenting the related numbers).
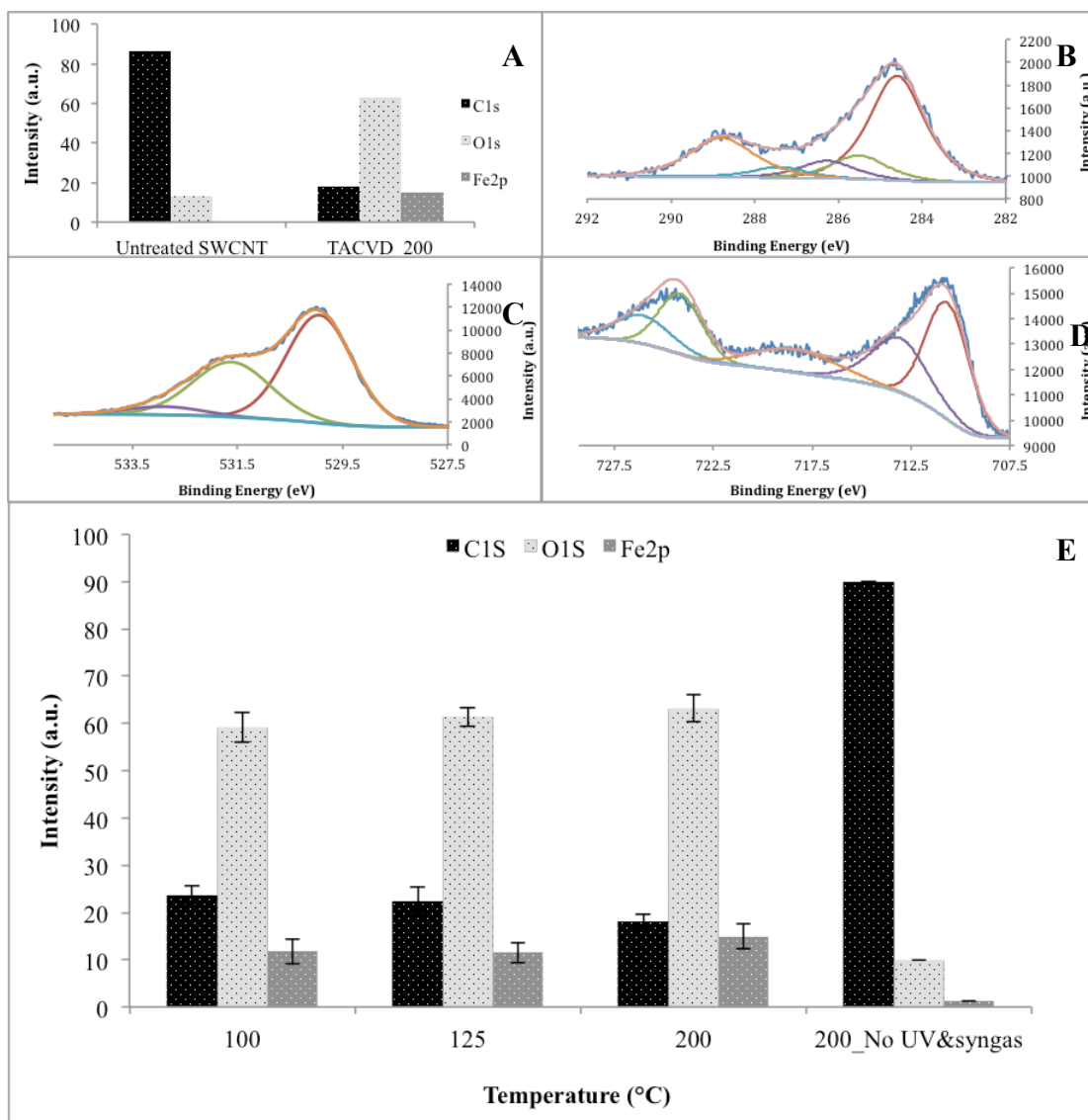
Figure B 3. A) Survey XPS spectra of treated SWCNT by syngas/TACVD_200 C, B) C1s HR-XPS of SWCNT treated by syngas/TACVD_200 C, C) O1s HR-XPS of SWCNT treated by syngas/TACVD_200 C, D) Fe2p HR-XPS of SWCNT treated by syngas/TACVD_200 C, E) Plotting of survey XPS spectra treated SWCNTs by syngas over heating (the inset table is presenting the related numbers).
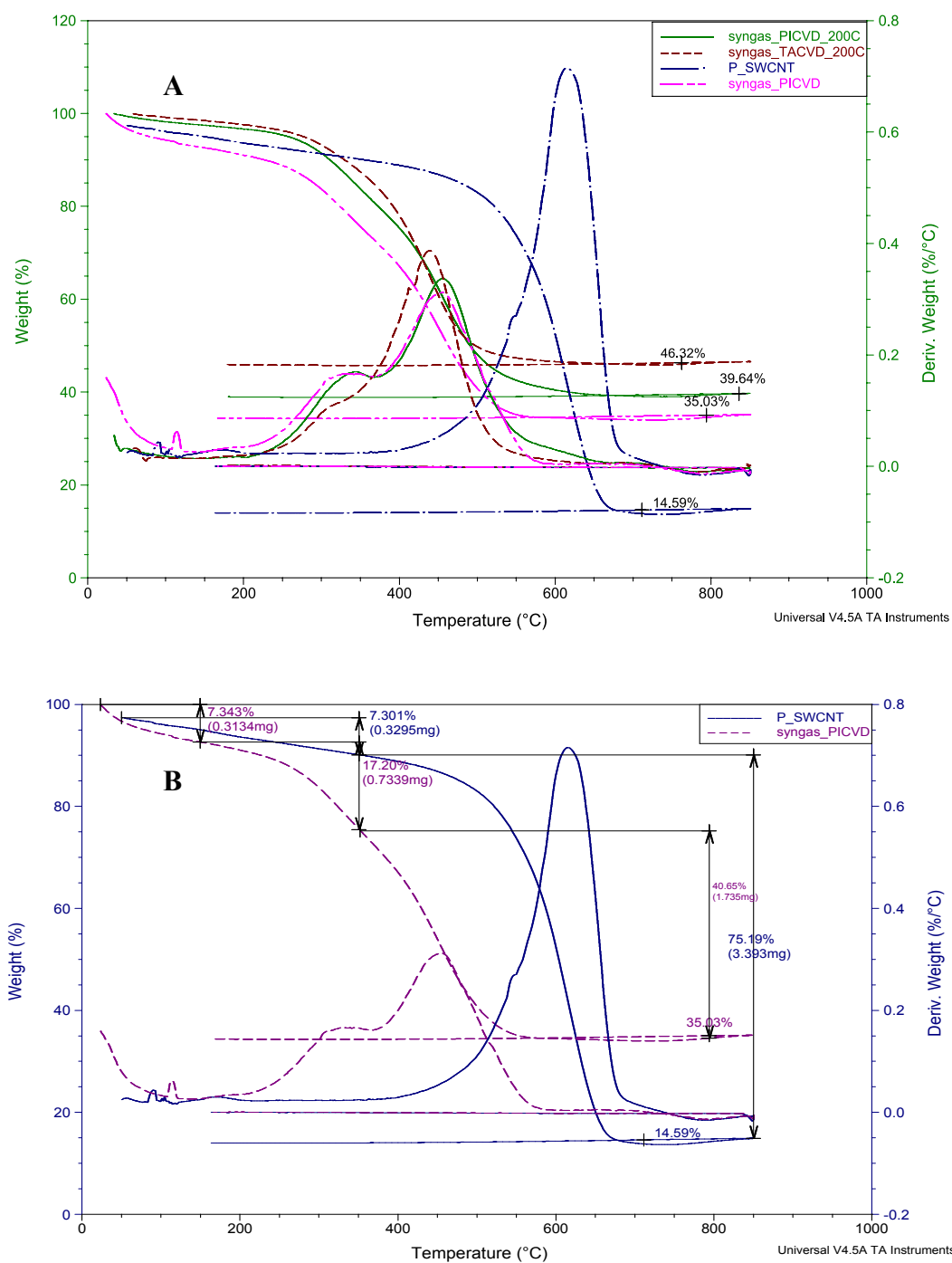
Figure B 4. A) Thermal decomposition analysis (TGA and DTG graphs) of P-SWCNTs, PICVD, TACVD and PICVD over 200 ºC heating; B) Comparison of P-SWCNT and PICVD treated SWCNTs in terms of thermal analysis.
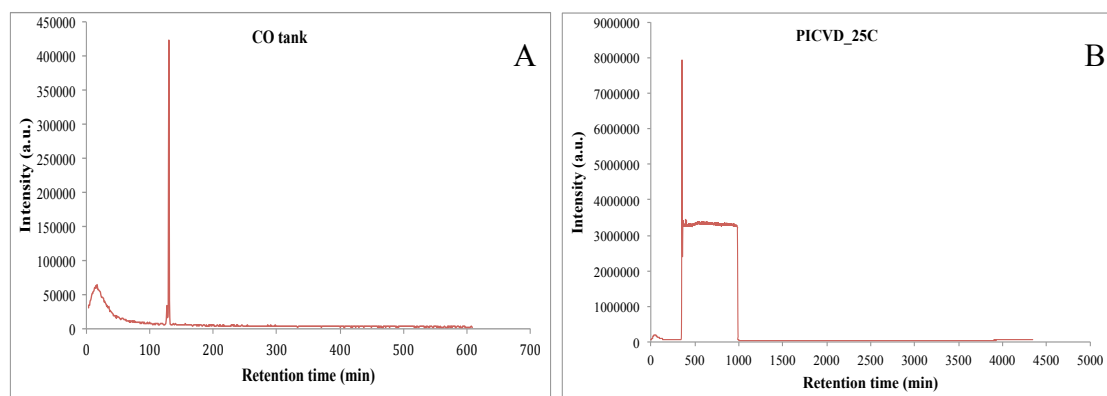
Figure B 5. GC-MS analysis of outlet gas of PICVD reactor A) before, and B) after syngas/PICVD reaction.
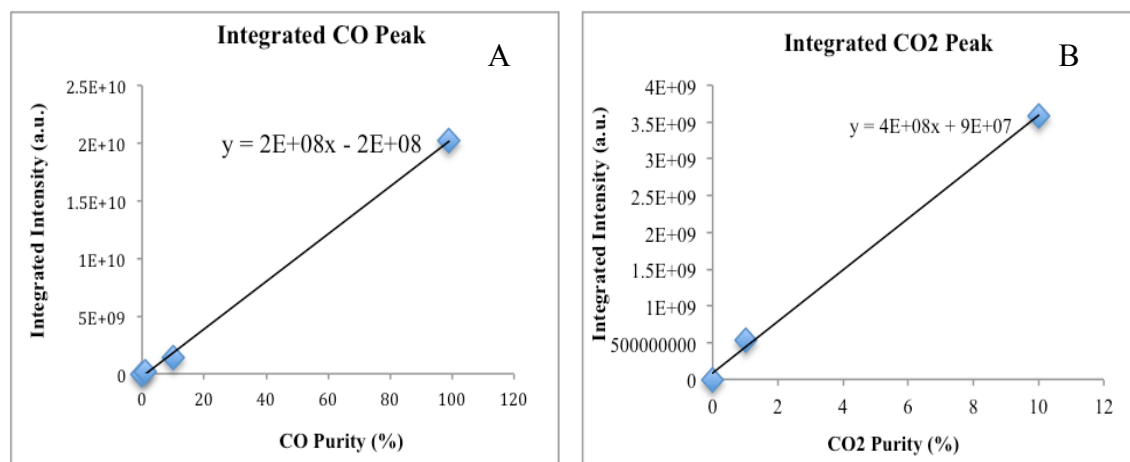

Figure B 6. Calibration curves of A) CO, B) CO_2 that performed according to calibrating gas cylinders at purities of 1, 10 and 99.99%.

APPENDIX C – INVESTIGATION OF CYTOTOXICITY OF TREATED SWCNTS WITH SYNGAS/PICVD ON A FULL RANGE OF WETTABILITY

Materials and Methods

Materials

Pure-SWCNTs with 1.5 nm average diameter and 100 μm average length synthesized by RF induction thermal plasma process as described previously (Kim et al., 2009a), were purchased from Raymor-NanoIntegris (96.5% w/w, Quebec, Canada). n-hexadecane (≥99%, EMD-Millipore) and Hydrogen peroxide (H_2O_2, 50% (w/w)) were purchased from Fisher Scientific (Montreal, Quebec). Syngas (chemically pure CO and H_2, Air Liquide) and argon (99.9%), were purchased from Air Liquide. UVC germicidal lamps (Model T-97505-80, Cole-Parmer Inc) were used as a photo-source for treatments of SWCNTs (Peak emission of 253.7 nm and irradiance of 0.01 W/cm^2 at 3.5 cm). C3H10T1/2 multipotent stem cells, Ethanol 70% (v/v), Sterile PBS (phosphate buffer saline) at pH 7.4, Fetal bovine serum (FBS)**,** penicillin (100 U/mL), streptomycin (100 μg/mL), trypsin-EDTA (0,25% (w/v)), and trypan blue noted Bleu de trypan 0,4% (w/v) were purchased from Sigma Aldrich.

Material Characterization

We used X-ray photoelectron spectroscopy (XPS) to obtain more insight about surface functionalities with a VG ESCALAB 3 MKII system (Mg Kα x-rays, with a pass energy of 100 eV for survey scans). We measured wettability of treated and untreated SWCNTs through sessile drop contact angle (CA) with an FDS OCA DataPhysics TBU 90E tensiometer (2 μL of water droplets for 3 s). We calculated surface energy using the Owens-Wendt method (using water and n-hexadecane liquids) [180]. Transmission electron microscopy (TEM, JEOL model JEM2100F) and scanning electron microscopy to identify carbonaceous impurities and observe cells on the SWCNT surfaces, respectively.

SWCNT Treatment

SWCNTs were treated by syngas/PICVD as described elsewhere. Briefly, 1*1 cm^2 of SWCNT

bucky papers were placed inside the PICVD reactor and precursors (iron pentacarbonyl, syngas and hydrogen peroxide) passed through the reactor. First of all, the reactor was purged with argon, then CO, $Fe(CO)_5$ and H_2 precursors were introduced at various to the reactor as well H_2O_2 as a radical photo-initiator via the syringe pump. By changing six operational parameters including precursor molar ratio (H_2/CO), the total pressure of reactor, treatment time, the flow rate of precursors and use of PI and position of samples inside the reactor, various wettabilities (surface energies) were obtained.

Cell Culture

10000 (or 2000) cellules/cm^2, C3H10T1/2 multipotent stem cells were grown in a minimum essential alpha medium (αMEM; GibcoW, Grand Island, NY, USA) supplemented with 10% heat-inactivated fetal bovine serum (FBS; Wisent, St-Bruno, Qc, Canada), 100 mgml^{-1} streptomycin (Invitrogen), and 100 U ml^{-1} penicillin (Invitrogen, Burlington, ON, Canada) at 37 ºC under a humidified 5% CO_2 atmosphere.

Sample Preparation and Cell Viability and Proliferation Assays

We prepared samples in dispersion form to investigate cell viability and proliferation of cells. Accordingly, treated SWCNTs prepared in various concentrations (0–100 mg ml^{-1}) were first sterilized by annealing at 180 C for 2h. Then, we made their suspension in αMEM culture media with FBS (10 % (v/v)). To make a uniform suspension, we dispersed them using an ultrasonic bath for 30 min. Further; we seeded C3H10T1/2 multipotent stem cells in a 24-well plate (10 000 cells/cm^2). We allow cells to reach 40% of confluence for proliferation and 80% of confluence for viability assays. After treating cells with SWCNT suspensions (500 mL/well), we incubated them 48 and 72 h under 5% of CO_2 atmosphere at 37 ºC. Each SWCNT concentration had a corresponding blank without cells.

Table C 1. Designed set of experiments to see effect of syngas/PICVD treatment on cytotoxicity of SWCNTs.

Samples	Contact Angle (°)	Concentrations of SWCNTs in the Cell Culture (µg/ml)	Sample form
Pure SWCNTs	79	0, 25, 50, 75, and 100	Suspension
S1	41	0, 25, 50, 75, and 100	Suspension
S2	58	0, 25, 50, 75, and 100	Suspension
S3	60	0, 25, 50, 75, and 100	Suspension
S4	49	0, 25, 50, 75, and 100	Suspension
S5	49	0, 25, 50, 75, and 100	Suspension
S6	58	0, 25, 50, 75, and 100	Suspension

Results and Discussion

Material Characterization

The main impurities remaining in the purchased P-SWCNTs were Fe, Ni, Y and amorphous carbon as identified by XPS results (Figure 14) and TEM measurements (Figure 16). After treatment of SWCNTs with syngas/PICVD, a lot of oxygen-containing groups such as COOH, OH, and CO deposited on their surfaces as indicated in the survey XPS analysis (Figure C1) and discussed deeply before in chapter 4 and 5. Energy-dispersive X-ray spectroscopy (EDS) characterization (Figure C2) gives a good idea of the surface impurities of SWCNTs in a qualitative manner. After coating of SWCNTs with syngas/PICVD, all of the samples were characterized with TEM. Figure C3A shows SWCNTs before purification while there are a lot of impurities such as metallic nanoparticles, amorphous carbons, and graphitic carbons on the SWCNT surfaces. Figure C3B shows purified SWCNTs while the most of the impurities were removed. However, there were still a few impurities such as metallic nanoparticles and graphitic carbons among the SWCNT bundles. After treatment of SWCNTs with syngas/PICVD, the coating (a clear semi-polymeric film) is deposited around the SWCNT bundles (Figure C3C) rather than individual SWCNTs (Figure C3D).

The results of the mitochondrial enzymatic activity of cells (C3H10T1/2 cells) incubated with SWCNTs in suspension (samples S1-S6) plotted in Figures S17 and S18 revealed no cytotoxic effect on cells (after 48 and 72h). The cells were able to proliferate between 48 and 72h with or without SWCNTs as shown by the increase observed using MTS assays (Figure C4). However this experiment was only performed one time in duplicate and such results must be confirmed.
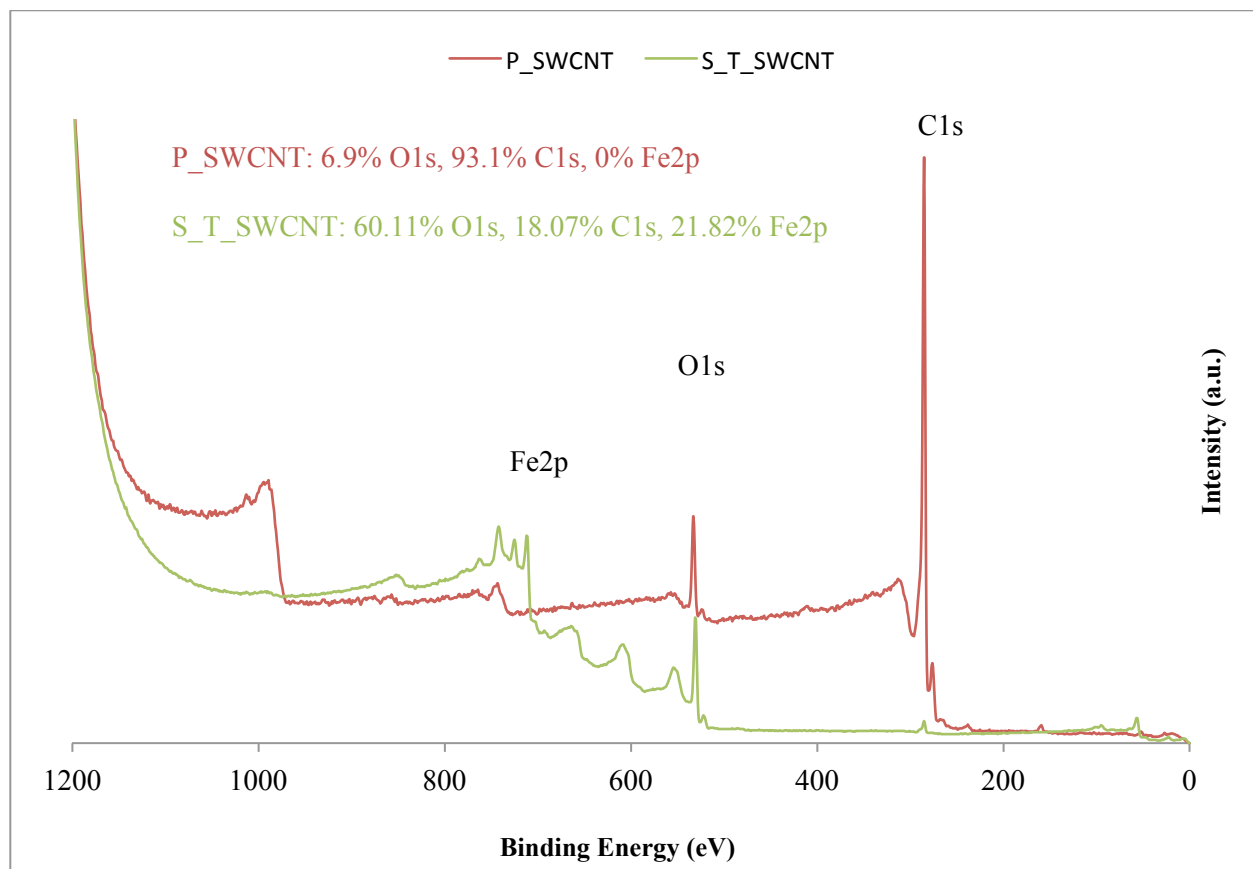

Figure C 1. XPS survey spectra of treated (Green color) and untreated SWCNTs (Red color).

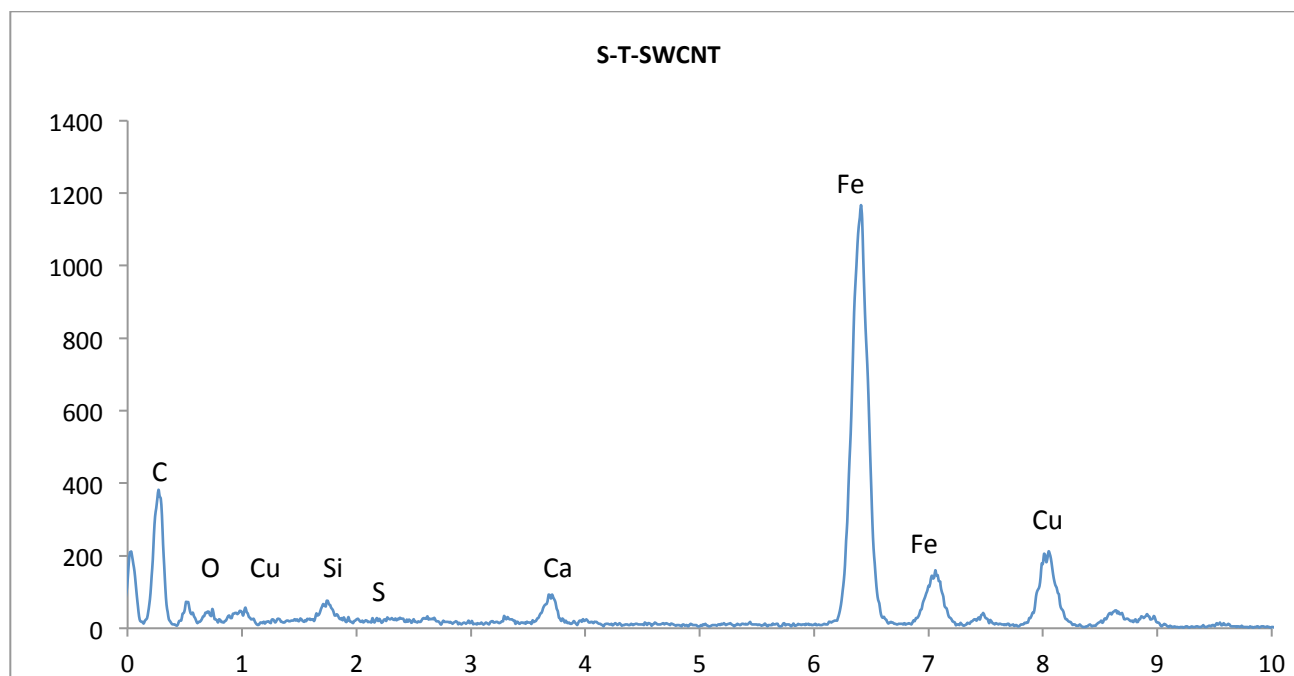Figure C 2. EDS Characterization of S-T-SWCNT treated by PICVD/syngas under vacuum for 2h. Carbon and oxygen presented as the main elemenets while S and Cu came from the membrane and Si and Ca came from impurities.
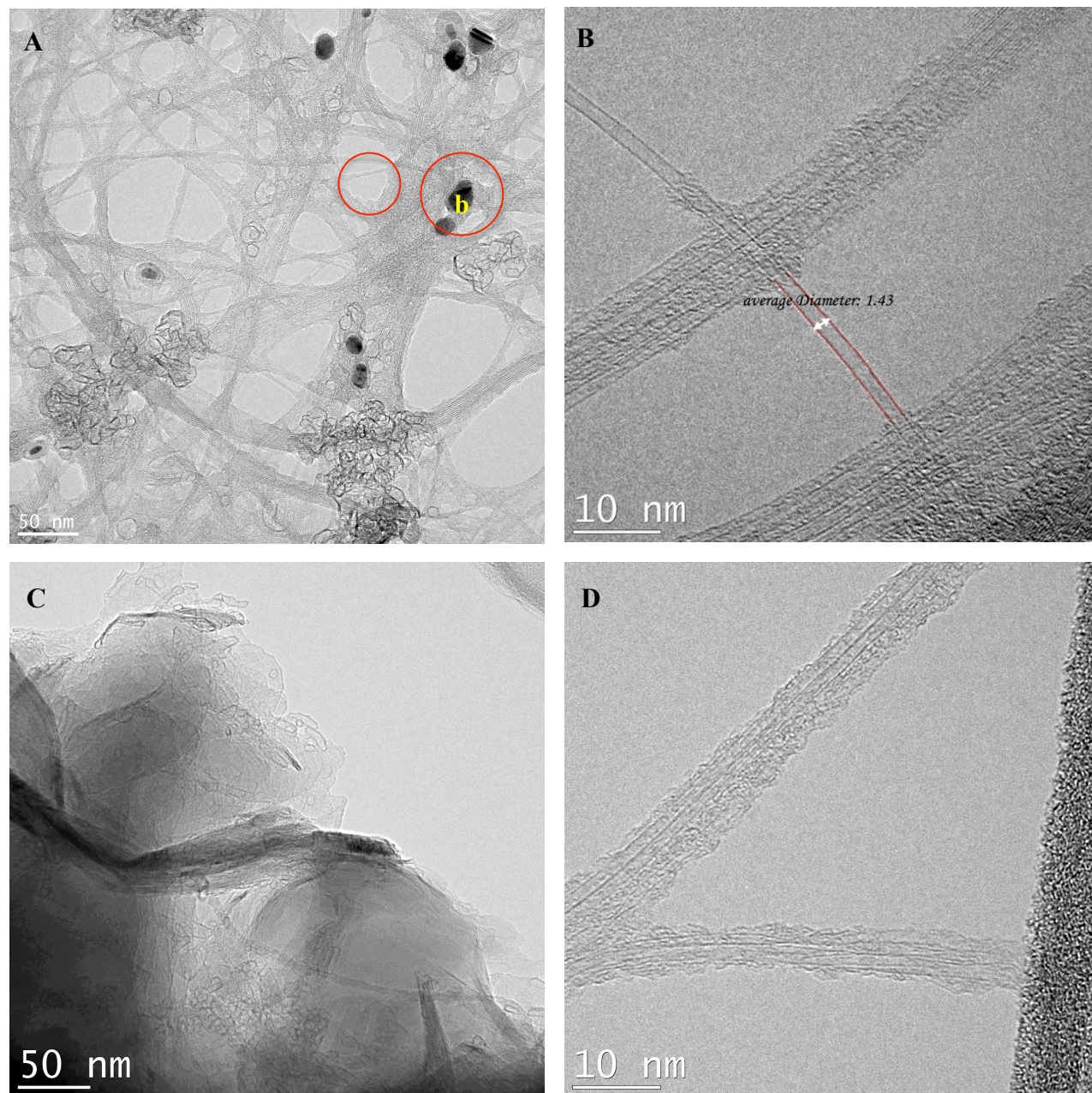
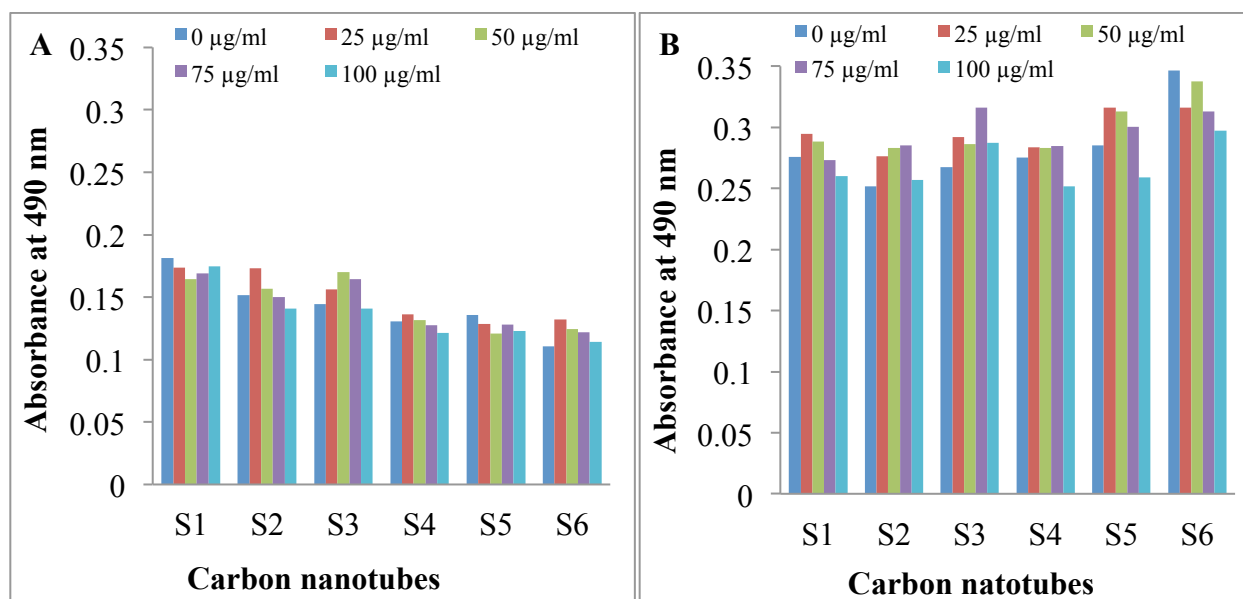Figure C 3. TEM images of treated SWCNTs by syngas/PICVD.

Figure C 4. Mitochondrial enzymatic activities in multipotent C3H10T1/2 cells incubated with or without carbon nanotubes for A) 48h, B) 72h.

APPENDIX D – PURIFICATION OF CNTS

Purification Methods of CNTs

Purification methods of CNTs can be basically classified into two categories, namely chemical and physical methods.

Purification by Wet Chemistry Oxidation

This chemical method works based on the selective oxidation of impurities where the oxidation rate of carbonaceous impurities is faster than the oxidation rate of CNTs and/or oxidation of metallic impurities in acids, such as nitric acid (HNO_3) [2], sulfuric acid (H_2SO_4) [38], oxygen [3], hydrochloric acid (HCl) [2], and even a combination of acids (i.e., nitric acid and sulfuric acid [39]). It is believed that the above-mentioned oxidants diffuse into the carbon shell and then oxidize the metal catalysts of the corresponding metal oxide or hydroxide. These oxidants tend to attack SWCNTs from the end cap and oxidize metallic particles. Amorphous carbon impurities can be attacked from all sides leading to its preferential removal during the purification procedure. This method is common and popular because of its practicality, simplicity, versatility, and applicability to both metal catalysts and amorphous carbons. However, the chemical methods always influence the structure of CNTs by creating oxygen functional groups on the surface (–OH, C=O, and –COOH) [22]. Chemical oxidation of substances can be conducted either in the liquid- or gas- phases. In the liquid phase oxidation, oxidizing agents are nitric acid (HNO_3), hydrogen peroxide (H_2O_2), sulfuric acid (H_2SO4), or a mixture of these reagents, such as HCl/H_2O_2, H_2SO_4/HNO_3 [3, 235, 236]. In the gas phase oxidation, SWCNTs are held in a temperature range of 225-760 °C under an oxidizing atmosphere, such as air (oxygen), a mixture of $Cl_2/H_2O/HCl$, or a mixture of $Ar/O_2/$ H_2O [236]. For large-scale purification, gas phase oxidations are very attractive because of their simplicity in scaling up and affordable cost. The main reason for the low efficiency of this method is the similarity between the reactivity of CNTs and carbonaceous impurities to the oxidants used for leading nanotube burning during the purification process [3].

SWCNT Purification Based on High-Temperature Annealing

Carbonaceous and metallic materials possess different physical properties either under an inert atmosphere or a high vacuum. It is believed that graphite is stable even at 3000°C under nitrogen, while metal evaporates at lower temperatures (Iron: 2862 ºC, Gold: 2856 ºC) [23, 237, 238]. Therefore, removing metal particles is expected to be effective at high temperature. The efficiency of high-temperature annealing in removing the metal particles and carbonaceous impurities of MWCNTs has been reported as high as 99.9% [23, 239]. Annealing CNTs (at a temperature higher than 1400 °C) changes the structure of CNTs through rebuilding their structural defects, enlarging their diameter, and the transformation of SWCNTs to MWCNTs or MWCNTs to double-walled CNTs (DWCNTs) [23, 237-240]. Briefly, high-temperature annealing of CNTs is one of the most efficient methods for the removal of metal particles at the tips or in the hollow core of CNTs and also for the structural evolvement from disordered to straight, crystalline layers. High-temperature annealing not only increases the mechanical strength and thermal stability of CNTs but also affects their electronic transport property. The main disadvantage of this method is graphitized carbonaceous impurities formed during the process. Therefore, this method is best suited to remove residual metal particles and amorphous carbon impurities [19, 165].

Purification Based on Microwave Heating

Microwaves can be coupled with the residual metal catalyst and cause significant local temperature increases around the individual CNTs. This induced high temperature facilitates oxidation and the rupturing of the carbon layers surrounding the catalyst particles. In this condition, a simultaneous acidic oxidation (or even after this process) provides a highly efficient purification procedure [241, 242]. For example, Ko et al. (2005) used a microwave assisted heating method in a closed vessel containing 5 mL HNO_3 to purify MWCNTs [243]. Following microwave irradiation at 160°C for 30 min, they could remove almost all the carbonaceous impurities from the MWCNTs [243]. This method is noninvasive, simple, fast, and clean compared to traditional purification approaches. It accelerates the oxidation reactions and, consequently, improves relative yields of purification for carbonaceous impurities [243]. In addition, as compared with many of the above-mentioned selective oxidation methods, this method does not damage the CNTs' structure and the processing time is relatively short (around

30 min) as compared with traditional refluxing techniques over hours [241, 242].

Purification Based On Physical Methods

The physical methods work based on the differences in size, aspect ratio, magnetic properties of CNTs with impurities (such as metallic and carbonaceous impurities), and gravity. This method is able to remove graphitic sheets, carbon nano-spheres (CNSs), aggregates, and separate CNTs with different aspect ratios. Chromatography, filtration, centrifugation, and electrophoresis are classified in the category of physical purification methods. These methods are described briefly in the following subsections.

Purification Based on Filtration

Purification by filtration is based on some physical differences (aspect ratio, size, and solubility) between CNTs and impurities. The particles with a small size or greater solubility can pass through the filter and CNTs with a larger aspect ratio will be retained on the filter membrane. Fullerenes and poly-aromatic carbons are soluble in some organic solvents, such as CS_2 and toluene, while CNTs are not. Therefore, the impurities can be easily removed by dispersing the prepared sample in these organic solutions followed by filtering [236]. For example, Bandow et al. (1997) reported a single method to purify SWCNTs using micro-filtration in the presence of cationic liquids [244]. They first dispersed SWCNTs in CS_2, then sonicated and finally filtered the suspension through the membrane under N_2 pressure. They could successfully remove poly-aromatic carbons, fullerenes, C_{60}, and C_{70}, from SWCNTs [244]. There is no negative impact on the structures of CNTs using this method but it is time-consuming and affected by the quality of the raw samples. Using surfactants (to make a stable CNT suspension) followed by an ultra-sonication process is strongly recommended to prevent the filter membrane from becoming blocked [18, 23, 236].

Purification Based on Centrifugation

Centrifugation works on particles with different densities. Centrifugation can separate amorphous carbon and carbon nanoparticles (CNPs) based on the differences in dispersion stability between CNTs and the impurities in aqueous media [240, 245]. The different stabilities result from electrical surface charges introduced by acid treatment. Low-speed centrifugation (2000G) for a

few hours (i.e., 2h) is effective in removing amorphous carbon and leaving SWCNTs and CNPs in the sediment. The main disadvantage of this method is that CNTs need a prior acidic treatment through which some functional groups will be introduced onto their surface [23].

Purification Based On Chromatography

Chromatography is another physical method that separates the components in a mixture based on differences in partitioning behavior between a flowing mobile phase and a stationary phase. This method is normally used to separate small quantities of SWCNTs into fractions with a small length and diameter distribution. For example, Yang e al. (2005) used size exclusion chromatography (SEC) without using any agents for dispersion. They purified SWCNTs using a multistep method in which the SWCNTs were first sonicated in HCl and then passed through a membrane. Then, they made purified SWCNTs water dispersible by treating them in H_2SO_4/HNO_3 (3:1 v/v) for 8 h under sonication. SEC was used to separate SWCNTs from the impurities while Milli-Q water (flow rate of 0.1 ml/min) included well-defined particles with 4 nm pores. Both methods were chosen as the mobile phase and stationary phase, respectively.

They could remove almost all the carbonaceous impurities, such as carbon particles and graphene fragments, from the oxidized SWCNTs. They could also separate SWCNTs based on their length [246]. The materials that are smaller than the pore size can enter the pores and therefore have a longer path and transit time, while larger materials that cannot enter the pores are eluted first. This method has no effect on the structure of CNTs yet it has demonstrated success to some extent in terms of the length separation of CNTs. The length distributions, however, are still broad, and the method is very difficult to scale up [246, 247].

Purification Based On Electrophoresis

Electrophoresis utilizes the electrostatic forces generated between a charged body and an electrode using an alternating current (AC) or a direct current electric field. A charged particle is drawn along the field lines toward the electrode carrying an opposite charge to that of the particles. This technique can be used to separate the CNTs with a specific diameter, length, or conductivity by refining the experimental conditions [247, 248]. For example, Doorn et al. (2003) used capillary electrophoresis (CE) for the separation of SWCNT bundles from individual ones. A lab-built CE consisted of a fused silica capillary (75 µm in internal diameter and 75 cm in

length). Capillaries were first injected with sodium hydroxide (NaOH) for 3 min and then rinsed with deionized water. For separations, they applied a +15 KV voltage while a 50 mM trizma base was used as a run buffer. Suspensions of SWCNT/sodium dodecyl sulfate (SDS) were injected under pressure using a syringe. The results showed that CE is capable of separating CNT bundles from individual ones based on the differences in mobility of SWCNTs [249]. A common characteristic of these techniques is that they require a high dispersion of CNTs in a single solution, such as sodium dodecyl sulfate (SDS) [249]. Impurities affect the electrical properties of SWCNTs. Therefore, a pretreatment process, including purification and functionalization of SWCNTs (i.e., acidic treatment), is needed to obtain the isolated CNTs having high dispersibility in a solution [247, 248].